1

Introduction

Photons are both great and lousy as qubits for quantum computing for exactly the same reason: they don't interact strongly with each other. On the positive side this means that it is relatively easy to preserve the quantum state, or information, carried by a photon for long periods of time. This is a serious problem for solid state qubits where decoherence of the quantum state is the predominant obstacle to scalable quantum computing. Photons are also the way in which quantum information is communicated between distant locations. On the negative side it is extremely hard to perform two-qubit operations, required for quantum computing, with photons. This is where the strength of solid state qubits lie: solid state systems can often interact readily with each other. It is clear then that there are two approaches to solve this dichotomy: convert the travelling qubit from being photon-based to a solid state system to allow two-qubit operations, and then convert the qubit back to a photon for transmission; or devise some way in which to increase the interaction strength between photons so that two-qubit operations are possible directly between photons. The first part of this thesis relates to the first option and we study methods to transfer quantum information from the optical to the solid state regime as well as related coherent population transfer techniques. The remainder of this thesis focuses on the second option and we study methods to create strong photon-photon interaction via nonlinear optics.

In the first chapter we cover the stimulated Raman adiabatic passage (STIRAP) technique in a Λ-type three level system. STIRAP can be used to transfer quantum information from light to atoms. Furthermore STIRAP is closely related to electromagnetically induced transparency (EIT) which is also briefly covered in this chapter; and STIRAP also serves as a good introduction to the Stark-shift-chirped rapid adiabatic (SCRAP) technique that lies at the heart of chapter 3. Both STIRAP and SCRAP are population transfer techniques, while the EIT phenomenon is well known for "slow" light and optical pulse storage. We also present some background on the nitrogen-vacancy (NV) centre defect found in diamond. The NV centre can be configured as a

Λ system, as well as a four-level tripod system and is extensively used in later parts of the thesis where we address option two, the generation of photon-photon interaction.

In chapter 3 we explain the SCRAP technique as applied to Λ-type three level systems. We then engineer the pulses used in SCRAP using optimal control techniques in order to obtain pulses that result in high fidelity population transfer over a wide range of optical field detunings. This could prove useful since solid state systems are known to suffer from large inhomogeneous broadenings, while having many other advantages over atomic vapour systems. By using the optimally robust version of SCRAP that we find, one should be able to achieve a greater fidelity population transfer in the presence of large inhomogeneities.

In chapter 4 we give an overview of the known methods to perform quantum logic between photons. We introduce the quantum phase gate (QPG) and more particularly the controlled sign flip (C-sign) gate. We review the seminal Knill, Laflamme and Milburn (KLM) [1] scheme for implementing a probabilistic CZ gate with linear optics. We also review the improvement made to this scheme by replacing measurements with quantum nondemolition measurements, thus rendering the scheme almost deterministic. We see in this chapter that there are advantages and disadvantages to each of the different schemes. The most important part of this chapter is the section on the QPG by using a large Kerr nonlinearity. We will try to minimise the disadvantage of this scheme by showing that sufficiently large conditional phase shifts can be obtained in a physically realisable system. The explanation of how a large cross-Kerr interaction can be used to implement a QPG is the primary motivation for the next chapter.

In chapter 5 we present our proposal to realise a QPG in a high-Q cavity-QED setting making use of a single NV centre in a nanodiamond. The NV centre is used in the tripod-level configuration. We review a previous proposal of how a QPG can be realised in a four-level tripod system. We then give a very brief introduction to microresonator cavities which have high-Q whispering gallery modes. We also review the literature on coupling NV centres to microresonators. Following extensive numerics, our models suggest that it is possible to obtain high fidelity conditional phase gates with phase shifts in excess of π radians in this system – enough to realise a CZ gate. Process tomography of the simulated QPG gate compares very well with an ideal QPG that results in the same conditional phase shifts.

Lastly, in chapter 6 we show that it is also possible to use this system to create a superposition of two macroscopically distinguishable states, that is a Schrödinger cat state, by using two weak coherent fields as inputs and making a measurement on the second field. Schrödinger cat states have application in the testing of quantum theory (e.g. through violations of Bell inequalities [2–4]) through to applications in quantum information processing. We make use of a recently introduced measure of macroscopic quantum superposition to evaluate our Schrödinger cat states and find that states with a measure close to the maximum achievable for the given input states can be found.

2

EIT, STIRAP and NV centre as a Λ-type three level system

Photons are ideal carriers of quantum information since they are fast and robust. To perform quantum logic with photons though is difficult as it is difficult for two photons to interact, making gates between two qubits hard to perform reliably. Atoms (or molecules which will hence forthwith be included when referring to atoms) can, under some circumstances, store quantum states reliably for long periods of time and allow for easily manipulated interactions between individual states. To facilitate the transport, storage and subsequent manipulation of quantum states it would be highly advantageous to have a means to coherently transfer a quantum state carried by light to atoms and vice versa.

Atomic vapours have been extensively investigated for use as quantum information storage media by "slowing down", or even "stopping", a light pulse carrying quantum information. This is achieved by mapping the quantum state of the light to a long-lived spin state in the ensemble of atoms by means of electromagnetically induced transparency (EIT) [5–9]. This process can then be reversed, and the pulse coherently resynthesised from the atomic ensemble. EIT is closely related to an adiabatic passage technique known as Stimulated Raman Adiabatic Passage (STIRAP), that makes use of two classical light fields of similar strength, whereas in EIT one of the two fields (the probe or signal field) is much weaker than the other (the coupling or control field). For EIT to be used to implement quantum memory the probe field is a weak quantum field, and carries the quantum information. The reason atomic vapours are good candidates is the same reason why atomic vapours are good sources of laser light: all the atoms in the ensemble are identical to each other, with identical energy transitions and resonance frequencies. This homogeneity of the atoms means that the light pulses used in EIT experiments can be tuned to specific transitions in the atoms and that these light fields will then interact strongly with all the atoms in the ensemble. Doppler-shifts due to

3

different velocities of the atoms can largely be compensated for. Diffusion of the atoms on the other hand presents a larger problem in that the resynthesised optical pulse after storage will not be identical to the original pulse if the positions of the atoms changes significantly during the storage time. This is seen as noise in the retrieved pulse and limits the duration for which an optical pulse can be stored within the atomic ensemble.

Solid-state implementations of stored light by means of EIT may have a number of potential advantages over atomic vapour implementations. Notably they have the potential to greatly reduce (possibly eliminate) limitations on the storage lifetime, which is mainly due to unavoidable atomic diffusion and Doppler velocities in atomic vapour systems. A higher atomic density has the potential to yield a stronger interaction between the light and atomic ensemble because of an increase in the number of interacting centres. Being more compact and simpler to use/manufacture may indicate great scalability [10] on the part of solid-state implementations. EIT and slow light have been demonstrated in rare-earth doped semiconductors e.g. Pr doped Y_2SiO_5 [11, 12], whereas only EIT has thus far been shown in nitrogen-vacancy colour centres in diamond [13, 14]. Solid-state media are, however, not without their own problems: the biggest of which is inhomogeneous broadening of the energy levels, which leads to a reduction in the number of atoms/centres that will be resonant with the incident optical fields. Each atom/centre experiences a different electronic environment due to a number of factors e.g. the local strains in the crystal lattice, which results in differing energy spectra for different centres in the ensemble. The light used in the EIT experiment will then be slightly off-resonance with many of the centres, and substantially off resonant with some of the centres. To overcome this problem spectral hole-burning techniques [15], can be used to select a subset of the atoms/centres within a narrow spectral range: essentially the broadening is decreased by pumping most of the atoms/centres into a highly excited state and only leaving a subensemble possessing a much narrower linewidth which can then be used for quantum memory. Clearly this creates another problem in that typically only a small fraction of the initial atoms/centres remain in this subensemble to interact with the light. This reduction decreases the coupling strength between the light and the atoms and subsequently results in lower fidelity operations.

In chapter 3 we propose an alternative method to at least partially surmount the reduction caused by inhomogeneous broadening. This entails employing an additional (pulsed) field to induce Stark shifts in the energy levels and thus bring the required transitions on resonance at specific times. This technique when employed with classical light fields is known as Stark-shift-chirped rapid-adiabatic-passage (SCRAP), and is closely related to STIRAP and other coherent population transfer (CPT) techniques. SCRAP has been shown to be far more accommodating with regard to variances in detunings between resonant frequencies of atomic systems and the frequency of illuminating light when performing coherent population transfer [16]. We show that the SCRAP pulses can be optimised such that population transfer occurs for a wide range of detunings.

Here in this chapter we explain the STIRAP technique as an introduction to the EIT phenomenon and as a basis for understanding the SCRAP technique used in chapter 3. EIT, explained in section 2.2, is also behind the large cross-Kerr nonlinear
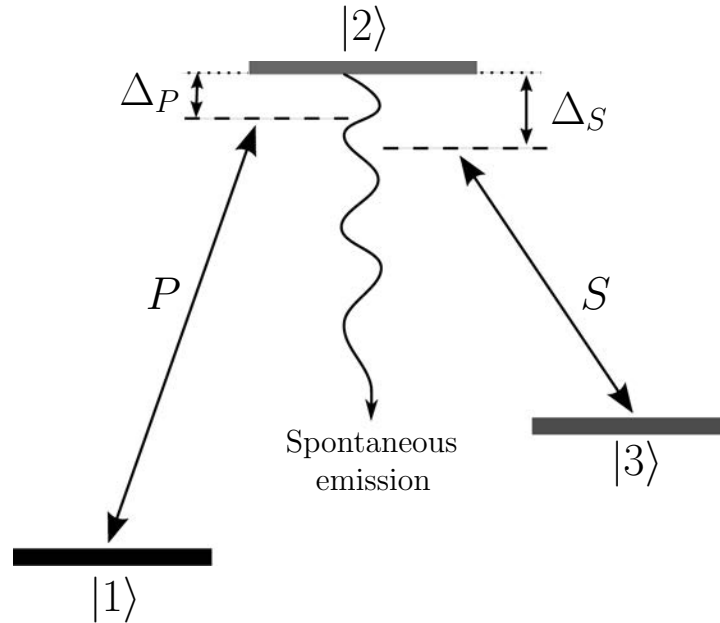
FIGURE 2.1: The Λ-type three-level energy scheme. States $|1\rangle$ and $|2\rangle$ are coupled by the pump pulse P which has a detuning Δ_P from being exactly on resonance. Similarly states $|2\rangle$ and $|3\rangle$ are coupled by the Stokes pulse S which has a detuning Δ_S. State $|2\rangle$ is short lived with spontaneous emission occurring out of the system into the continuum of states.)

interaction achievable in the tripod system that we use in chapter 5 for the NV centre based quantum phase gate. A brief introduction to the NV centre is given in section 2.3.

2.1   Stimulated Raman Adiabatic Passage (STIRAP)

In this section and the following section the links between Stimulated Raman Adiabatic Passage (STIRAP), Electromagnetically Induced Transparency (EIT) and quantum memory will be discussed. This will be achieved by briefly explaining the mechanisms behind these different concepts.

First the STIRAP technique will be explained: The STIRAP method is closely related to EIT, and also to SCRAP applied to a three-state system. Both the STIRAP and SCRAP techniques aim to transfer population from one state to another via a two photon process. STIRAP uses two coherent pulsed laser fields that couple two long lived ground states to a single excited state, in order to achieve complete population transfer between the two long lived ground states. One state is initially populated, while the other is the target state.

In explaining the mechanisms involved in STIRAP we will only consider Λ-type three-level systems (Figure 2.1), though STIRAP can also be implemented in other

level configurations of three-level systems (i.e. V- and cascade- (ladder-) type systems). State $|1\rangle$ is the initially populated ground state (or some other long-lived state), with an optical transition to the intermediate exited state $|2\rangle$. This exited state has a short lifetime and can decay via spontaneous emission to state $|1\rangle$ or $|3\rangle$ if the system is "closed"; or to a state outside the three-state system, if the system is "open". State $|3\rangle$ is the target state, with an optical transition to $|2\rangle$. For most applications, and certainly for those discussed in later sections, state $|3\rangle$ is a long-lived state, for example a ground state sublevel. States $|1\rangle$ and $|2\rangle$ are coupled by the "pump" laser pulse whilst states $|3\rangle$ and $|2\rangle$ are coupled by the "Stokes" laser pulse. The frequencies of these two lasers are typically not exactly on resonance with their respective transitions. Thus the pump field has a detuning of Δ_P from single-photon resonance for transition $|1\rangle \rightarrow |2\rangle$; and the Stokes field has a detuning, Δ_S, from single-photon resonance for transition $|3\rangle \rightarrow |2\rangle$. These two transitions are the only dipole-allowed transitions in the system. The detuning from two-photon resonance (that is, the compound detuning of the two photon transition from the lower ground state to the upper ground state) is given by $(\Delta_P - \Delta_S)$. The presence of single-photon detunings does not prevent population transfer, but for STIRAP to work it is essential that the two-photon resonance condition $\Delta_P = \Delta_S$ holds.

Naively one would expect the pump pulse to precede the Stokes pulse so that the population can be driven $|1\rangle \rightarrow |2\rangle \rightarrow |3\rangle$. This would however allow for population loss from the excited state through spontaneous emission. In STIRAP the pulse sequence has a "counterintuitive" ordering: the Stokes pulse precedes the pump pulse. Even though both states $|2\rangle$ and $|3\rangle$ initially have no population in them the Stokes pulse, which couples them, performs an essential function: it places the system in an eigenstate that is "dark" or "trapped". It is so called since subsequent application of the pump pulse will drive the population from state $|1\rangle$ to state $|3\rangle$ without allowing any population to move through state $|2\rangle$ thus avoiding any radiative decay. With this ordering of the pulses, the populating of state $|2\rangle$ is completely avoided, thus allowing complete population transfer from $|1\rangle$ to $|3\rangle$, as long as the pulses also meet certain coherence and adiabaticity conditions.

2.1.1   The Hamiltonian, eigenstates and population transfer

The simplest implementation of STIRAP, where the three states $|1\rangle$, $|2\rangle$ and $|3\rangle$ (see Figure 2.1) with respective energies E_1, E_2 and E_3 are coupled by two coherent fields (pump and Stokes fields) with respective frequencies, ω_P and ω_S, is described by the Hamiltonian

$$H(t) = H_0 + V_P(t) + V_S(t). \tag{2.1}$$

The un-perturbed Hamiltonian is given by

$$H_0 = \hbar\omega_0|2\rangle\langle2| + \hbar\left(\omega_0 - \omega_1\right)|3\rangle\langle3|, \tag{2.2}$$

with the transition frequency between states $|1\rangle$ and $|2\rangle$, $\omega_0 = (E_2 - E_1)/\hbar$, and between states $|3\rangle$ and $|2\rangle$, $\omega_1 = (E_2 - E_3)/\hbar$. The detuning of the pump field from resonance

is then $\Delta_P = \omega_0 - \omega_P$, whereas for the Stokes field the detuning is $\Delta_S = \omega_1 - \omega_S$. The interaction Hamiltonians ($V_P(t)$ and $V_S(t)$) that describe the interaction between the system and the pump and Stokes fields respectively are given by

$$V_P(t) = \mathbf{d} \cdot \mathbf{E}_P, \tag{2.3}$$

$$V_S(t) = \mathbf{d} \cdot \mathbf{E}_S. \tag{2.4}$$

$\mathbf{d}$ is the dipole moment operator for the atomic system, which for a transition between the excited state $|e\rangle$ and ground state $|g\rangle$ is

$$\mathbf{d} = \mathbf{d}_{eg}|e\rangle\langle g| + \mathbf{d}_{eg}^*|g\rangle\langle e|, \tag{2.5}$$

where $\mathbf{d}_{eg} = \langle e|\mathbf{d}|g\rangle$. The classical electric field due to the pump laser is given by

$$\mathbf{E}_P = \mathbf{E}_{0P}e^{-i\omega_P t} + \mathbf{E}_{0P}^*e^{i\omega_P t}, \tag{2.6}$$

and similarly for the Stokes field. The interaction Hamiltonian for the pump can then be written as

$$V_P(t) = (\mathbf{d}_{21}|2\rangle\langle 1| + \mathbf{d}_{21}^*|1\rangle\langle 2|) \cdot \left(\mathbf{E}_{0P}e^{-i\omega_P t} + \mathbf{E}_{0P}^*e^{i\omega_P t}\right), \tag{2.7}$$

$$= \hbar\left(\Omega_P e^{-i\omega_P t} + \tilde{\Omega}_P e^{i\omega_P t}\right)|2\rangle\langle 1| + \hbar\left(\tilde{\Omega}_P^* e^{-i\omega_P t} + \Omega_P^* e^{i\omega_P t}\right)|1\rangle\langle 2|, \tag{2.8}$$

and the Stokes interaction Hamiltonian can be derived in a similar fashion. The Rabi frequency, $\Omega_P = \hbar^{-1}\mathbf{d}_{21} \cdot \mathbf{E}_{0P}$, is proportional to the strength of the pump field. The counter-rotating Rabi frequency is $\tilde{\Omega}_P = \hbar^{-1}\mathbf{d}_{21} \cdot \mathbf{E}_{0P}^*$. The Hamiltonian of the system can be transformed into the interaction (Dirac) picture by the unitary operator, $U = e^{iH_0 t/\hbar}$. The interaction picture Hamiltonian is related to the Schrödinger picture Hamiltonian as follows:

$$\bar{H}(t) = i\hbar\dot{U}U^\dagger + UHU^\dagger \tag{2.9}$$

$$= i\hbar\left(\frac{i}{\hbar}UH_0\right)U^\dagger + U\left(H_0 + V_P + V_S\right)U^\dagger \tag{2.10}$$

$$= UV_PU^\dagger + UV_SU^\dagger. \tag{2.11}$$

The Hamiltonian in the interaction (Dirac) picture becomes

$$\bar{H}(t) = \hbar\left(\Omega_P e^{i\Delta_P t} + \tilde{\Omega}_P e^{i(\omega_P+\omega_0)t}\right)|2\rangle\langle 1| + \hbar\left(\tilde{\Omega}_P^* e^{-i(\omega_P+\omega_0)t} + \Omega_P^* e^{-i\Delta_P t}\right)|1\rangle\langle 2|$$
$$+ \hbar\left(\Omega_S e^{i\Delta_S t} + \tilde{\Omega}_S e^{i(\omega_S+\omega_1)t}\right)|2\rangle\langle 3| + \hbar\left(\tilde{\Omega}_S^* e^{-i(\omega_S+\omega_1)t} + \Omega_S^* e^{-i\Delta_S t}\right)|3\rangle\langle 2|. \tag{2.12}$$

Equation (2.12) reveals that the counterpropagating parts ($\tilde{\Omega}_P$, $\tilde{\Omega}_P^*$, $\tilde{\Omega}_S$ and $\tilde{\Omega}_S^*$) are oscillating at a much higher frequency ($\omega_0 + \omega_P \gg \Delta_P$ and $\omega_1 + \omega_S \gg \Delta_S$) than the other parts. These rapidly oscillating parts will average out to zero over any appreciable amount of time. Any realistic optical pulse will have a time dependent Rabi frequency $\Omega(t)$ that will have a small time derivative compared to the frequency

of the optical transition, and as such we can replace the up to here assumed constant Rabi frequencies with time dependent frequencies without loss of generality. In the rotating wave approximation the rapidly oscillating parts are neglected, resulting in the Schrödinger picture interaction Hamiltonian:

$$
\begin{aligned}
V(t) = {} & \hbar \left(\Omega_P e^{-i\omega_P t} \right) |2\rangle\langle 1| + \hbar \left(\Omega_P^* e^{i\omega_P t} \right) |1\rangle\langle 2| \\
& + \hbar \left(\Omega_S e^{-i\omega_S t} \right) |2\rangle\langle 3| + \hbar \left(\Omega_S^* e^{i\omega_S t} \right) |3\rangle\langle 2|,
\end{aligned} \tag{2.13}
$$

which with the un-perturbed Hamiltonian, (2.2), and after a transformation to the co-rotating frame gives the final Hamiltonian:

$$
H(t) = \frac{\hbar}{2} \begin{bmatrix} 0 & \Omega_P(t) & 0 \\ \Omega_P^*(t) & 2\Delta_P & \Omega_S(t) \\ 0 & \Omega_S^*(t) & 2\left(\Delta_P - \Delta_S\right) \end{bmatrix}. \tag{2.14}
$$

The phases of the pulses can be chosen such that the Hamiltonian is real:

$$
H(t) = \frac{\hbar}{2} \begin{bmatrix} 0 & \Omega_P(t) & 0 \\ \Omega_P(t) & 2\Delta_P & \Omega_S(t) \\ 0 & \Omega_S(t) & 2\left(\Delta_P - \Delta_S\right) \end{bmatrix}. \tag{2.15}
$$

The strength of the coupling of the states by the fields is determined by the Rabi frequencies $\Omega_P(t)$ and $\Omega_S(t)$. The detunings are defined by

$$
\begin{aligned}
\hbar\Delta_P &= (E_2 - E_1) - \hbar\omega_P, \\
\hbar\Delta_S &= (E_2 - E_3) - \hbar\omega_S,
\end{aligned} \tag{2.16}
$$

for the pump and Stokes fields respectively. For STIRAP it is mandatory that the two laser pulses are in two-photon resonance, ie. $\Delta_P - \Delta_S = 0$. Taking the two-photon resonance condition into consideration, the three instantaneous eigenstates of $H(t)$ are

$$
\begin{aligned}
|a^0(t)\rangle &= \cos\Theta(t)|1\rangle - \sin\Theta(t)|3\rangle, \\
|a^+(t)\rangle &= \sin\Theta(t)\sin\Phi(t)|1\rangle + \cos\Phi(t)|2\rangle + \cos\Theta(t)\sin\Phi(t)|3\rangle, \\
|a^-(t)\rangle &= \sin\Theta(t)\cos\Phi(t)|1\rangle - \sin\Phi(t)|2\rangle + \cos\Theta(t)\cos\Phi(t)|3\rangle.
\end{aligned} \tag{2.17}
$$

Where the time dependent mixing angle $\Theta(t)$ is defined by

$$
\tan\Theta(t) = \frac{\Omega_P(t)}{\Omega_S(t)}, \tag{2.18}
$$

and $\Phi(t)$ is given by

$$
\tan 2\Phi(t) = \frac{\sqrt{\Omega_P^2(t) + \Omega_S^2(t)}}{\Delta_P}. \tag{2.19}
$$

We will however only be interested in eigenstate $|a^0(t)\rangle$. The instantaneous eigenstates are also known as the adiabatic states of $H(t)$: if the system is initially in $|a^0(t)\rangle$ and evolves adiabatically (i.e. slow enough such that the system adapts its configuration)
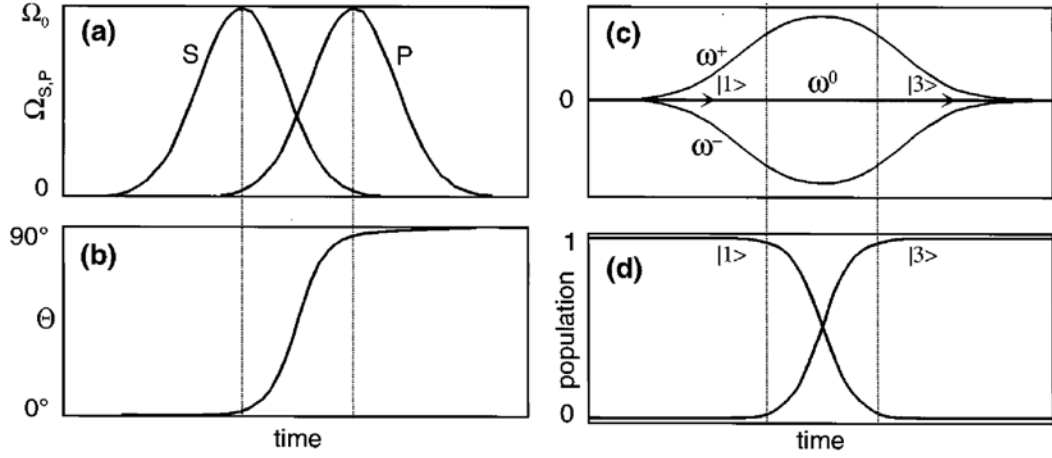
FIGURE 2.2: Graph (a) shows the Rabi frequencies of the pump and Stokes pulses; (b) the evolution of the mixing angle, Equation (2.18); (c) the eigenvalues of the adiabatic states; (d) the change in population from state $|1\rangle$ to $|3\rangle$. All pulses were taken as being exactly on resonance ($\Delta_P = 0$ and $\Delta_S = 0$). (Figure taken from Bergmann *et al.* [18])

the system will remain in state $|a^0(t)\rangle$. For adiabatic evolution the pulses need to be smooth, in addition, according to Vitanov *et al.* [17] a good rule of thumb is a very large pulse area:

$$A = \int_{-\infty}^{+\infty} \Omega(t)dt \gg 1. \tag{2.20}$$

The instantaneous eigenenergies for the eigenstates (2.17) are

$$\omega^0(t) = 0,$$
$$\omega^+(t) = \Delta_P + \sqrt{\Delta_P^2 + \Omega_P^2(t) + \Omega_S^2(t)},$$
$$\omega^-(t) = \Delta_P - \sqrt{\Delta_P^2 + \Omega_P^2(t) + \Omega_S^2(t)}. \tag{2.21}$$

STIRAP is based on the zero-eigenenergy state $|a^0(t)\rangle$ (see Equation (2.17)) which has no component of the excited state $|2\rangle$ so there will be no population loss due to radiative decay. State $|a^0(t)\rangle$ is also known as a trapped or dark-state. Making use of the counterintuitive pulse ordering, i.e. Stokes pulse before pump pulse, initially $\Omega_P(t)/\Omega_S(t) \to 0$ which then changes, when the pump Rabi frequency is smoothly increased as the Stokes Rabi frequency is smoothly decreased, to $\Omega_P(t)/\Omega_S(t) \to \infty$. Thus $|a^0(t)\rangle$ starts in state $|1\rangle$ (the initial state of the system) and then changes to state $|3\rangle$, achieving complete population transfer into the target state (see Figure 2.2). As long as the evolution is adiabatic the system will follow the dark-state: $|a^0(t)\rangle$. Only during diabatic evolution will the system evolve along a state that is a superposition of the zero-eigenenergy eigenstate $|a^0(t)\rangle$ and the other eigenstates $|a^\pm(t)\rangle$. This results
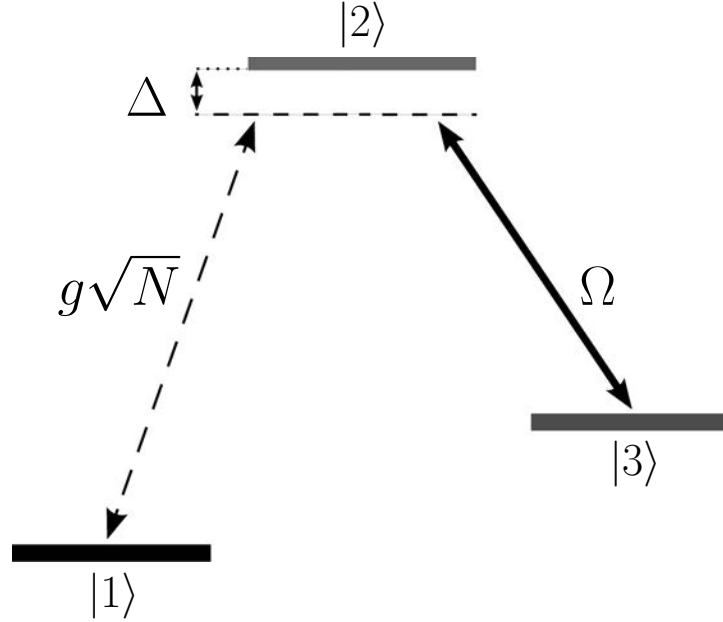
FIGURE 2.3: The Λ-type three-level energy scheme. States $|1\rangle$ and $|2\rangle$ of each atom in the ensemble of N atoms are coupled by the probe field which has a detuning Δ from being exactly on resonance. The atom-field coupling constant that describes the strength of the interaction between the probe and the atoms is g. Similarly states $|2\rangle$ and $|3\rangle$ are coupled by the control field with a Rabi frequency of Ω.

in population in the short lived state $|2\rangle$. Thus we see that with the conditions of two-photon resonance, counterintuitive pulse ordering, and adiabatic evolution, the requirements for STIRAP are met and population transfer from state $|1\rangle$ to $|3\rangle$ can be achieved with 100% fidelity where zero population is intermediately transferred to state $|2\rangle$ and thus suffers no radiative loss.

2.2   EIT and the Dark-State Polariton

Electromagnetically induced transparency (EIT) is a method whereby an optically thick (opaque) medium is rendered transparent to a weak probe laser field through the application of a second (classical) coupling field known as the control field (on account of controlling the opacity of the medium) [19]. EIT leads to a reduction in the group velocity of an optical field, resulting in a way to store and retrieve optical pulses. With the storage and high fidelity retrieval of optical pulses we have a technique for implementing quantum memory. Once again in explaining the mechanisms behind this we will only consider Λ-type three-level systems (Figure 2.3). Level $|1\rangle$ is the ground state (or some other long-lived state) with an optical transition to the exited state $|2\rangle$. State $|3\rangle$ is a long-lived state with an optical transition to $|2\rangle$. The classical pulsed

laser field that couples states $|2\rangle$ and $|3\rangle$, called the Stokes field in STIRAP, is now called the control field, whereas the pump laser field (coupling states $|1\rangle$ and $|2\rangle$) is now a weak probe laser field. Herein lies the difference between STIRAP and EIT: STIRAP refers to two fields with approximately equal strength; EIT typically refers to the situation where there is one field that is significantly stronger than the other. The discussion of the Λ-type three level system in STIRAP also holds true for EIT. The Hamiltonian is still the same and all the eigenstate and eigenenergy equations are still relevant for EIT.

2.2.1   Transparency and Slowing/Stopping a Light Pulse

As a quick explanation of the transparency phenomenon, consider the situation where the control field is on, coupling states $|2\rangle$ and $|3\rangle$ (see Figure 2.3), and the ground state $|1\rangle$ of the system is populated. As the probe laser is scanned over a frequency range it will experience increasingly strong absorption as the frequency approaches that of the transition frequency of the $|1\rangle \to |2\rangle$ excitation until the detuning of the probe and the control fields are equal (two-photon resonance). At this point the system will evolve along the dark-state $|a^0(t)\rangle$, and no $|1\rangle \to |2\rangle$ excitations will be allowed. The medium will then be completely transparent to the probe field. As the system approaches two-photon resonance, there is a rapid change in the optical response of the medium. If the control field has a constant intensity, i.e. a constant Rabi frequency Ω, the response of the atomic ensemble to the probe pulsed laser can be given in terms of the linear electric susceptibility spectrum of the ensemble [9]

$$\chi\left(\Delta\right) = g^2 N \frac{\gamma_{13} + i\Delta}{\left(\gamma_{12} + i\Delta\right)\left(\gamma_{13} + i\Delta\right) + |\Omega|^2}. \tag{2.22}$$

Here γ_{ij} is the relaxation rate of the $|i\rangle \to |j\rangle$ coherence, N is the number of atoms in the ensemble, g the atom-field coupling strength (with $g^2 N$ the square of the collective coupling strength between the atoms and the field), and Δ is the single photon detuning of the fields (two-photon resonance is assumed: $\Delta_P - \Delta_S = 0$, see Figure 2.3). The imaginary part of the susceptibility describes the absorption properties of the medium. The intensity of the probe field laser leaving the medium is determined by the transmission coefficient ($T\left(\Delta\right)$),

$$I_{transmitted} = T\left(\Delta\right) I_{initial}, \tag{2.23}$$

where

$$T\left(\Delta\right) = \exp\left(-\text{Im}\left[\chi\left(\Delta\right)\right] kL\right), \tag{2.24}$$

where L is the length of the medium and $k = 2\pi/\lambda$ is the resonant wave number. The real part of the susceptibility describes the dispersion properties of the medium and determines the refractive index of the medium:
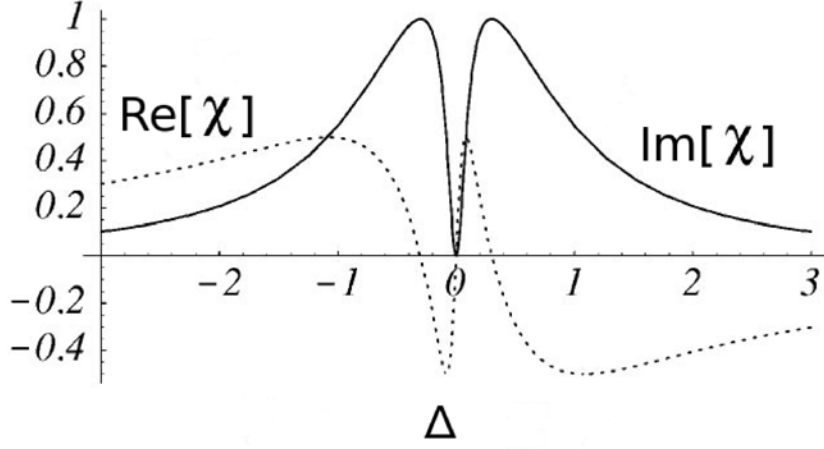
$$n = 1 + \frac{1}{2}\text{Re}\left[\chi\left(\Delta\right)\right]. \tag{2.25}$$

FIGURE 2.4: The real part of Equation (2.22), $\mathrm{Re}\left[\chi\left(\Delta\right)\right]$, describes the dispersion as a function of the frequency detuning Δ, whereas the imaginary part, $\mathrm{Im}\left[\chi\left(\Delta\right)\right]$, describes the absorption.

As first noted by Harris *et al.* 1992 [20], the rapid variation in the refractive index (see Figure 2.4) causes a reduction in the group velocity v_g of the probe pulse [8, 9, 19],

$$v_g = \frac{c}{n + \omega_P\left(dn/d\omega_P\right)}$$
$$= \frac{c}{1 + \frac{g^2 N\left(|\Omega|^2 - \gamma_{13}^2\right)}{\left(|\Omega|^2 + \gamma_{12}\gamma_{13}\right)^2}}, \tag{2.26}$$

which in the ideal case where state $|3\rangle$ is a perfect meta-stable state, i.e. the dephasing rate $\gamma_{13} = 0$, becomes:

$$v_g = \frac{c}{1 + g^2 N/|\Omega|^2}, \tag{2.27}$$

where $g^2 N/|\Omega|^2$ is referred to as the group index n_g. For the case when the ratio of the collective coupling and the control Rabi frequency (i.e. n_g) is large the group velocity can be significantly less than the speed of light in vacuum. As $\Omega \to 0$ the group velocity v_g tends to zero, thus bringing the pulse to standstill. When $\gamma_{13} \neq 0$ in Equation (2.26) there will be a lower limit on v_g. It is clear that the smaller the Rabi frequency of the control field the slower the group velocity will be. If the control field Rabi frequency is changed slowly enough it is possible to decrease the group velocity of a pulse as it moves through the medium without causing loss of information carried by the pulse. During the process energy is transferred from the electromagnetic field of the probe pulse into the atoms and control field. The result is that the state of the probe pulse is encoded into the spin states of the atoms while the photons of the probe pulse become part of the control field. Even though $v_g \ll c$, i.e. when only a small proportion of the pulse energy remains electromagnetic, the idea of a group velocity is still useful. To retrieve the information stored in the atomic states the process is reversed and energy

is transferred back into the probe electromagnetic field. This is perhaps best explained by introducing the quasiparticle, dark-state polariton.

2.2.2 Dark-State Polaritons and Quantum Memory

The dark-state polariton concept was first introduced by Mazets and Matisov (1996) [21], and was applied to pulse propagation by Fleischhauer and Lukin (2000) [22]. To introduce the dark-state polariton consider the pulse interaction from the viewpoint of the atoms in the ensemble. Before the probe pulse arrives in the medium the control field causes the dark state $|a^0\rangle$ to be identical to the ground state $|1\rangle$ in which the atoms have been initialised. The arrival of the probe pulse rotates the dark state into a superposition of states $|1\rangle$ and $|3\rangle$ (see equations (2.17) and (2.18)). As the probe pulse strength increases it loses energy that is transferred into the atoms and control field. The result is that the state of the probe pulse is encoded into the spin states of the atoms. If we assume that the probe pulse propagates in the z direction, the spin coherence will then also be a function of position. A new quantum field that incorporates the electromagnetic field of the probe pulse ($\mathcal{E}(z,t)$) and the spin coherence of the atomic states ($\sigma_{13}(z,t)$), the dark-state polariton field ($\Psi(z,t)$), is defined [8, 22] according to

$$\Psi(z,t) = \cos\theta(t)\,\mathcal{E}(z,t) - \sin\theta(t)\,\sqrt{N}\sigma_{13}(z,t). \qquad (2.28)$$

Another polariton, the bright-state polariton field ($\Phi(z,t)$), is also defined to be

$$\Phi(z,t) = \sin\theta(t)\,\mathcal{E}(z,t) + \cos\theta(t)\,\sqrt{N}\sigma_{13}(z,t) \qquad (2.29)$$

where the mixing angle $\theta(t)$ is given by

$$\tan^2\theta(t) = \frac{g^2 N}{\Omega^2(t)}. \qquad (2.30)$$

The normalised slowly varying probe electric field strength is $\mathcal{E}(z,t)$, whilst $\sigma_{13}(z,t)$ is the coherence between the two lower levels $|1\rangle$ and $|3\rangle$. The bright-state polariton is of no consequence here, as it leads to population in the excited state and thus degradation in the quantum memory due to population decay. It is often taken that states $|1\rangle$ and $|3\rangle$ are different spin sub-levels of the ground state, and hence $\sigma_{13}(z,t)$ would be the spin coherence between the states, describing a spin-wave. The dark-state polariton field obeys the equation of motion

$$\left[\frac{\partial}{\partial t} + c\cos^2\theta(t)\frac{\partial}{\partial z}\right]\Psi(z,t) = 0, \qquad (2.31)$$

which describes a shape-preserving propagation where the polariton field moves with a group velocity $v_{gr} = c\cos^2\theta(t)$. It is clear then that as the mixing angle increases from zero the dark-state polariton will change from being purely electromagnetic to being a superposition of the electromagnetic and spin-wave components. A rotation of θ from $0 \to \pi/2$ results in a complete encoding of the probe pulse onto the atomic states.
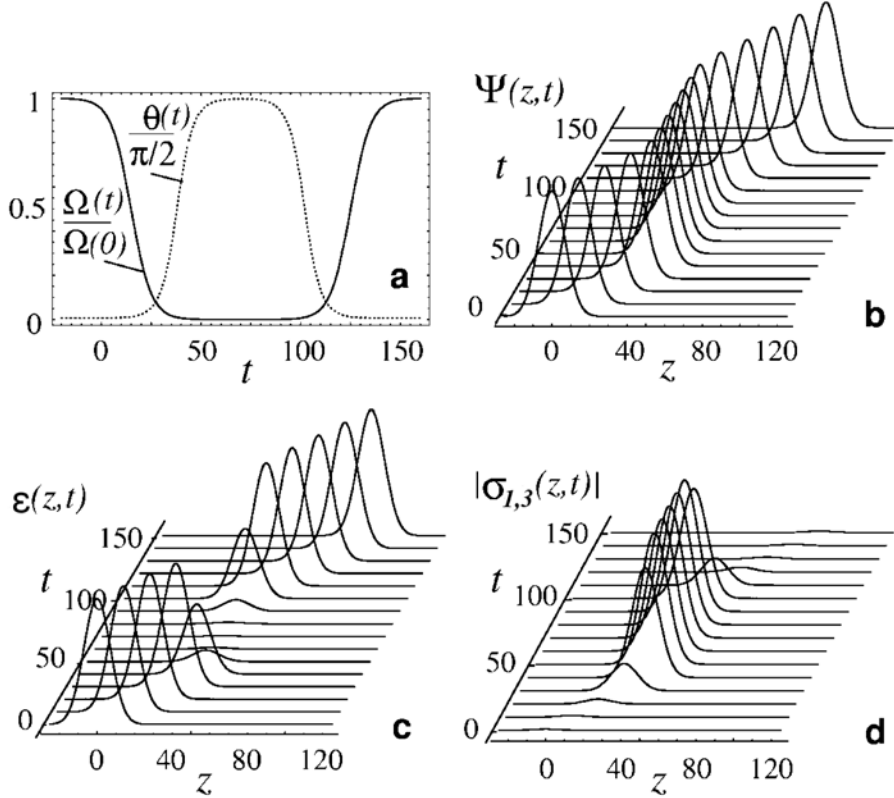
FIGURE 2.5: The change of the mixing angle $\theta(t)$ together with the change in the control field Rabi frequency $\Omega(t)$ is shown in (a). The coherent amplitude of the polariton (2.28) is plotted in (b), whilst (c) shows the electric field $\mathcal{E}(z,t)$ component and (d) the atomic component $\sigma_{13}(z,t)$ of the polariton. (Figure taken from Fleischhauer and Lukin [22])

The mixing angle can be controlled by adiabatically changing the control field $\Omega(t)$. When the control field is decreased to zero whilst the probe pulse is in the medium the pulse will be stopped by completely converting the probe pulse into a spin-wave in the medium. By subsequently increasing the control field back to its maximum the spin-wave can be changed back into an electromagnetic field and the probe pulse will be reconstructed (see Figure 2.5). This is the proposed way in which EIT and slow light will work as a quantum memory. The spin coherence of the atoms can have a very slow decay rate and as such the pulse could potentially be stored for a fairly long period of time.

Slow light due to EIT has been demonstrated in atomic vapours from as early as 1999 [6, 23], and has also been demonstrated in solid media in rare-earth ion-doped crystals [12], where pulses were stored for up to a second. It is an active field of research with a wide range of envisioned uses, from quantum memory [8] to telecommunications [24].

2.3   Solid-State: NV centre as candidate

Solid-state media are the obvious choice when trying to construct large numbers of quantum computing devices that would be easy to maintain and to use. When considering using EIT to store quantum information carried by light in the atomic states of an ensemble of atoms, solid-state implementations have some clear advantages over atomic-vapour implementations: in solids there is a far higher density of interacting atoms; the stored information does not degrade due to diffusion of the atoms during the storage time. In gas media the spin wave becomes scrambled once the atoms have moved significantly compared to the wave vector mismatch between the probe and the control beams, for this reason the two beams are usually copropagating in EIT experiments in gas media, thus minimising the mismatch. In solid-state implementations of EIT the beams do not have to be copropagating. In rare-earth-metal-doped crystals the concentration of dopant atoms can easily exceed the density of atoms in a gas by eight orders of magnitude [25]. Nitrogen-vacancy (NV) centres in diamond have also been considered as candidates for EIT media since their electron spins have large longitudinal and transverse relaxation times. They have long longitudinal relaxation times (T_1), since there is very low coupling between the electronic charge of the NV and the lattice vibration of the diamond crystal. They have very long transverse relaxation times (T_2) (or spin coherence) due to weak coupling to nearby ^{13}C nuclear spins in diamond [26]. Experiments demonstrating EIT in NV centres were first performed by Wei and Manson [13] and later by Hemmer *et al.* [14]. Santori *et al.* showed that CPT, an effect that is closely related to EIT can be performed in NV centres at zero magnetic field [27] and also in *single* NV centres [28] in for example nanodiamonds. Storage of light pulses for more than a second has been achieved in rare-earth ion-doped crystal [12], but is yet to be shown for the NV centre.

2.3.1   Description of the NV centre in diamond

We describe here the basic properties of the NV centre which we suggest as a possible system in which to implement the SCRAP protocol explained in chapter 3. We also consider the NV centre for the implementation of a cavity QED based quantum phase gate in chapter 5.

The nitrogen-vacancy centre in diamond is a stable naturally occurring defect formed when a substitutional nitrogen atom is accompanied by a vacancy at a nearest neighbour lattice site (Figure 2.6). The nitrogen-vacancy centre exists in two charge states: the neutral NV^0, and the negatively charged NV^-, we will only consider the latter in this work and for brevity's sake and conformity refer to as the NV centre. Due to the NV centre being primarily surrounded by ^{12}C, which has zero magnetic spin, very long spin coherence times are observed. Ground state spin coherence times of around 50 μs have been observed at room temperature in chemical vapour deposition (CVD) grown diamond by Kennedy *et al.* [30]. It was also noted that decreased concentration
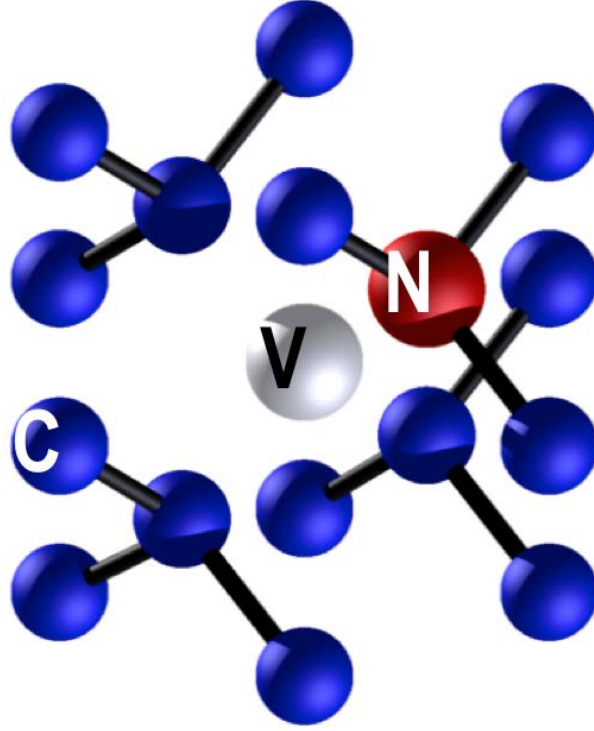
FIGURE 2.6: The nitrogen-vacancy centre structure. One substitutional nitrogen (N) atom is accompanied by a vacancy (V) at the nearest neighbour lattice site. (Figure courtesy of Carlo Bradac, Macquarie University.)

of Nitrogen in the samples resulted in longer coherence times. Moreover, recently extremely long coherence times up to 1.8 ms at 300 K were observed in isotopically rich and ultra pure CVD diamond [31], by decreasing the concentration of the ^{13}C isotope which also have a spin interaction with NV centres.

The NV centre has a C_{3v} symmetry and has a strong optical transition with a zero-phonon line at 637 nm (1.945 eV) due to a transition between the spin triplet states ^{3}A and ^{3}E. Considering the emission spectrum in Figure 2.7 one notes that the zero-phonon line becomes quite prominent at low temperatures and the sideband emission decreases. Since the NV's optical transition possesses a high fluorescence quantum yield (about 70%) and an excited state lifetime of 13 ns [32], the fluorescence of a single NV centre can be observed, an essential requirement for many quantum information applications.

It is only recently that some of the finer details concerning the energy levels has been elucidated, in particular the properties of excited states and two singlet levels believed to be between the ground and excited states have come under intense investigation. A schematic of the currently held model for the NV's energy level structure is presented in Figure 2.8. The ground state spin triplet, ^{3}A, is split by 2.88 GHz into a doublet T_{0X}, T_{0Y} ($m_s = \pm 1$) and a third spin sublevel T_{0Z} ($m_s = 0$) in the absence of a magnetic
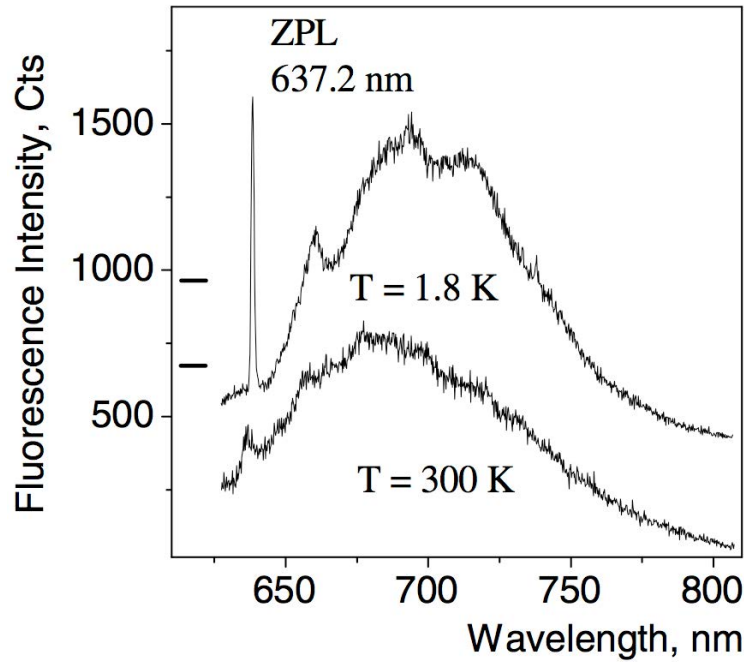
FIGURE 2.7: The NV centre emission spectra showing the ZPL at 637 nm and the phonon sideband extending from about 650-800 nm. Figure taken from Jelezko *et al.* [29]

field [34].

Recent experiments have established an infrared transition between the ^{1}E and ^{1}A singlet levels [33, 35], and it is believed that the ^{1}E level is closest to the excited ^{3}E states. The ^{1}A metastable singlet state has a temperature dependent lifetime between 219 ns at 295 K and 462 ns at 4.4 K. This level configuration is in disagreement with recent theoretical work [36, 37], which places the ^{1}A level above the ^{1}E level. These finer details, however, do not affect any of the work presented here in any way.

The excited state spin triplet is split into sublevels with $m_s = 0$ (T_{1Z}) and sublevels with $m_s = \pm 1$ ($T_{1X,1Y}$). The lifetimes of these sublevels have recently been determined and found to be 12 ns for T_{1Z} and 7.8 ns for $T_{1X,1Y}$ in bulk diamond [38] and 23 ns for T_{1Z} and 12.7 ns for $T_{1X,1Y}$ in a nanodiamond crystal [39].

There is spin selective intersystem crossing from the excited state into the ^{1}E singlet with a significantly higher probability for the $T_{1X,1Y}$ sublevels to decay nonradiatively (indicated by dashed lines in Figure 2.8) to ^{1}E than the T_{1Z} sublevel. From ^{1}E to ^{1}A there is an infrared optical transition (indicated in Figure 2.8 by a solid double arrow) as well as non-radiative decay and then finally from ^{1}A there is non-radiative decay into T_{0Z}. At least this is the interpretation of Acosta *et al.* [33] for their observations, and as mentioned above numerical theory studies suggests that the ^{1}E and ^{1}A levels are interchanged. Irrespective of this discrepancy after a few optical excitation and emission cycles the ground state becomes strongly spin-polarised, with the majority of population in the T_{0Z} ($m_s = 0$) state and almost nothing in the $T_{0X,Y}$ ($m_s = \pm 1$)
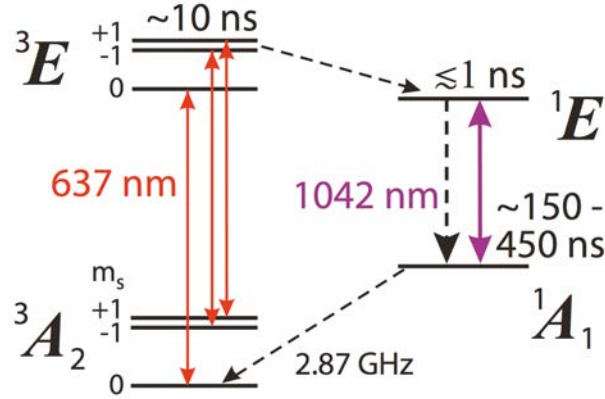
FIGURE 2.8: Energy level diagram of a NV centre. The allowed optical transitions between the ground (^{3}A) and excited (^{3}E) state sublevels are shown. The rate of the spin-selective intersystem crossing transitions (to and from the meta-stable (^{1}A) state) are indicated by the thickness of the arrows. (Figure taken from Acosta *et al.* [33])

state [26]. The exact mechanism is not important, but that this leads to a convenient way in which to initialise NV centres into the T_{0Z} state is extremely convenient. By subsequently applying an appropriate microwave pulse and magnetic field it is possible to prepare the NV centre in any superposition of the ground states.

Another essential result of the spin selective decay path is that it is possible to optically probe the spin state of the system since only the $T_{0Z} \rightarrow T_{1Z}$ transition is visible through fluorescence: If the NV centre is in the T_{0z} state a 637 nm laser will excite the system to T_{1Z} and fluorescent decay will be observed; on the other hand if the NV centre is in one of the $T_{0X,Y}$ states (or a super position of them) excitation will lead to the nonradiative decay from the excited $T_{1X,1Y}$ sublevels, suppressing the fluorescence output. This effect was observed by Jelezko *et al.* [40] in single NV centres and allows for convenient read-out of the electron spin quantum states. Furthermore the fidelity of spin read-out is very high, reported by Wrachtrup *et al.* [26] as 95%.

NV centres have shown great promise as efficient single photon sources [41, 42], this together with the long decoherence times of the ground states and the spin readout possible in the NV have placed the NV centre as a prime candidate for several quantum information applications. Notably the NV centre has been used to implement free space quantum key distribution [43]. Furthermore the NV is being investigated as a spin based qubit [29, 44]. NV centres in diamond nanocrystals are also being investigated as fluorescence bio-labels [45].

NV centres have been observed in nanodiamonds down to single digit nanometers in size [46, 47]. The linewidth of the zero-phonon line of a single NV centre in a high purity bulk diamond can reach the life-time limited linewidth of 13 MHz [48] but this is broader in NV's observed in nanodiamonds ∼16 MHz [49].

2.3.2 Inhomogeneous broadening in solid media

Inhomogeneous broadening of the spectral lines of a solid medium occurs because of the spread in resonance frequencies due to local perturbations in the crystal. Spatially varying local potentials are caused by strains which form due to various defects in the crystalline structure. In Johnsson and Mølmer [25] a thorough discussion on the limitations that inhomogeneous broadening places on EIT in solids is presented, just the main conclusions of which are given here. W_{13} and W_{12} are the inhomogeneous widths of the $|1\rangle \to |3\rangle$ and $|1\rangle \to |2\rangle$ transitions respectively. In solids the inhomogeneous broadening of the excited state (W_{12}) is several orders of magnitude greater than that of the ground state (W_{13}).

For the system to evolve along the dark state polariton (2.28) it is required that

$$\Omega^2(t) \gtrsim 3W_{12}W_{13}, \tag{2.32}$$

i.e. the control field strength must always dominate the inhomogeneous broadening. According to Equation (2.26) and the aforementioned requirement the minimum velocity of the dark state polariton occurs when $\Omega^2(t) \approx W_{12}W_{13}$ and is given by

$$v_g = \frac{cW_{12}W_{13}}{W_{12}W_{13} + g^2N}. \tag{2.33}$$

A near zero velocity can thus only be attained if $g^2N \gg W_{12}W_{13}$. In order to decrease the time required to stop the probe pulse it is advantageous to have the control field at a strength such that the probe pulse is in the slow group velocity regime as soon as it enters the medium, i.e. $W_{12}W_{13} \ll \Omega^2(0) \ll g^2N$. Good approximations of the optical and spin inhomogeneous broadenings observed in rare-earth doped materials gives a typical value of $W_{12}W_{13} \sim 10^{15}$ Hz^2. For NV centres values of $W_{12} = 375$ GHz and $W_{13} = 2.5$ MHz have previously been used [10], resulting in $W_{12}W_{13} \sim 10^{18}$ Hz^2. The inhomogeneous broadening in NV centres thus dictates that $\Omega^2(0) \sim 10^{20}$ Hz^2, and that $g^2N \sim 10^{22}$ Hz^2. These values for $\Omega^2(0)$ and g^2N are within reason since the it is possible to have large density of NV centres in the diamond lattice. Johnsson and Mølmer [25] suggest that W_{12} can be reduced by using spectral hole-burning techniques, before the probe pulse is applied, to select a subset of the centres within a specific spectral range. This is done by pumping all the centres in a broad frequency range to passive spectator levels, thus leaving only those with their transitions in the desired frequency range prepared in state $|1\rangle$. This solution has the drawback that the number of interacting centres N will be reduced and as such the collective coupling strength g^2N will also be reduced. The storage time of the pulse is limited by W_{13} because the phases of different centres evolve at different speeds due to inhomogeneity. Thus after a time $1/W_{13}$ the stored information will no longer be coherent. Something that is not considered in [25] is that due to the inhomogeneous broadening of the ground state W_{13}, some centres will not be in two-photon resonance, thus affecting the effectiveness of the EIT process. Those centres are essentially prevented from following the dark-state during evolution.

In the following chapter a method (SCRAP) to overcome the problem of two-photon off-resonance in adiabatic population transfer is discussed. The aim is to investigate the possibility of transferring this method to EIT and hence slow light.

3

Optimised Stark-shift-chirped rapid adiabatic passage

Recently a variation of STIRAP (an adiabatic passage technique which as seen in sections 2.1 and 2.2 is closely related to EIT), namely Stark-shift-chirped rapid adiabatic passage (SCRAP), has been shown to perform coherent population transfer with a high fidelity for a range of different detunings in a Λ-type three-level system [16]. That is, SCRAP is far more robust when there is large inhomogeneous broadenings present in the ensemble. In SCRAP, a separate (pulsed) field is added to the traditional STIRAP fields to induce AC Stark shifts in the energy levels and thus bring the required, initially off-resonant, transitions on resonance at specific times. We propose that a quantum version of SCRAP could surmount some of the limitations that inhomogeneous broadening places on "slow" light in solid state systems. In this chapter we test this hypothesis and find that indeed we can engineer the pulses of the SCRAP protocol resulting in a protocol robust against large unknown static shifts in the system's energy levels. We first introduce the standard SCRAP protocol in a three-level system.

We then make use of optimum control techniques somewhat similar to Khaneja *et al.* (2005) [50], in order to optimise the standard SCRAP pulses so as to minimise the decrease in fidelity brought on by inhomogeneous broadenings of the transitions. To quantify this we simulate the SCRAP process population transfer between two long lived ground states which experience large detunings due to inhomogeneous broadening. The optimisation methods employed are described in section 3.3.

Our main result is that we can improve the average fidelity of population transfer over a wide range of detunings which effect both the ground to excited state detuning and the ground to target state detuning (two-photon detuning). The optimal control pulses are thus tailored to provide effective state transfer (and thus EIT), in the presence of large inhomogeneous broadening. The modelled results obtained for the optimised pulses are given in section 3.4.
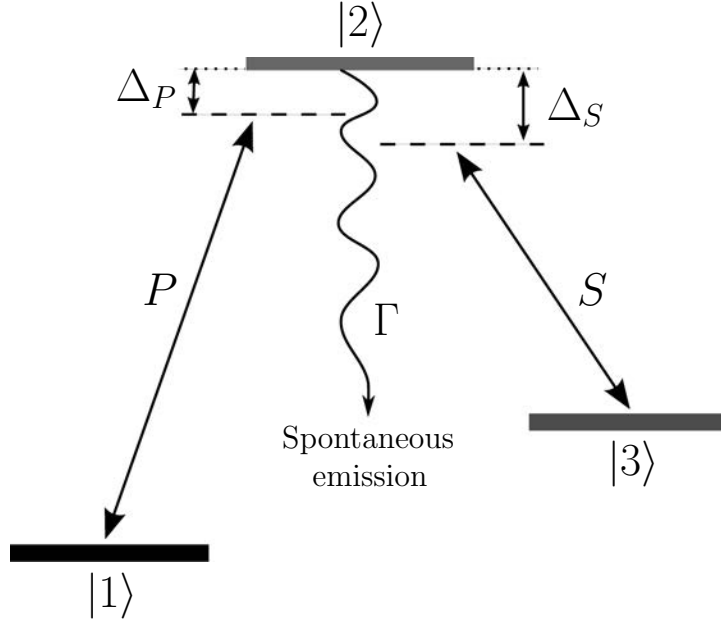
Figure 3.1: The Λ-type three-level energy scheme. States $|1\rangle$ and $|2\rangle$ are coupled by the pump pulse P which has a detuning Δ_P from being exactly on resonance. Similarly states $|2\rangle$ and $|3\rangle$ are coupled by the Stokes pulse S which has a detuning Δ_S. State $|2\rangle$ is short lived with spontaneous emission occurring out of the system

3.1 SCRAP

The Stark-chirped rapid adiabatic passage (SCRAP) technique was first proposed by Yatsenko *et al.* [51], and implemented experimentally by Rickes *et al.* [52] in two-level systems as an efficient method for complete population transfer between two states. It was later shown by Rangelov *et al.* (2005) [16], that the SCRAP technique can also be used to achieve complete population transfer through adiabatic passage in a three-level system, thus providing an alternative to STIRAP.

The Λ-type three-level system (Figure 3.1), is comprised of two long lived ground states and a single excited state ($|2\rangle$). For the purpose of complete population transfer we will assume that one of the ground states will be initially populated ($|1\rangle$), and the other will be the target state ($|3\rangle$). In general, the excited state has a short lifetime and STIRAP is effective at complete population transfer since it avoids populating the excited state by having the system evolve along a dark-state (see section 2.1). In both SCRAP and STIRAP states $|1\rangle$ and $|2\rangle$ are coupled by the "pump" laser pulse whilst states $|3\rangle$ and $|2\rangle$ are coupled by the "Stokes" laser pulse. The frequencies of these two classical laser fields are typically not exactly on resonance with their respective transitions, and have detunings Δ_P and Δ_S for the pump and Stokes lasers respectively. Herein lies the advantage that SCRAP has over STIRAP: STIRAP requires *exact* two-photon resonance ($\Delta_P - \Delta_S = 0$) in order to be effective, whereas SCRAP has a

much larger tolerance for two-photon detuning. Another advantage of SCRAP over STIRAP is that Stark shifts induced by a strong pump or Stokes field (as in multi photon transitions) has a much smaller effect on the final population in the target state for SCRAP. The pump or Stokes fields can induce Stark shifts in one of the ground states, and thus destroy the two-photon detuning that STIRAP relies on [16]. The defining difference between STIRAP and SCRAP is that in SCRAP a third strong far-off-resonance laser pulse, the Stark pulse, is also applied. The Stark pulse induces a Stark shift in the energy of the excited state (essentially leaving the energy of the lower levels unchanged), thus bringing the initially off-resonant transitions into resonance. The Stark shift causes the diabatic energy of state $|2\rangle$ to cross those of states $|1\rangle$ and $|3\rangle$, allowing population transfer from $|1\rangle$ to $|2\rangle$ and then to $|3\rangle$, completing the population transfer. It is thus clear that the diabatic energies of state $|1\rangle$ and $|2\rangle$ must cross before the diabatic energies of states $|2\rangle$ and $|3\rangle$ cross. It is also clear that decay out of the excited state will play some role in SCRAP and as such should be taken into account in the model, as opposed to STIRAP where decay could be neglected without affecting the outcome of the model.

In the rotating wave approximation, the Hamiltonian of the Λ-type three-level system depicted in Figure 3.1 is

$$H(t) = \frac{\hbar}{2} \begin{bmatrix} 0 & \Omega_P(t) & 0 \\ \Omega_P(t) & 2\left(\Delta_P + S_2\left(t\right)\right) - i\Gamma & \Omega_S(t) \\ 0 & \Omega_S(t) & 2\left(\Delta_P - \Delta_S\right) \end{bmatrix}, \tag{3.1}$$

where $\Omega_P(t)$ and $\Omega_S(t)$ are respectively the pump and Stokes laser field Rabi frequencies and $S_2\left(t\right)$ is the Stark shift in the energy of the excited energy level $|2\rangle$ due to a third far-off-resonance laser pulse (Stark pulse). For the examples used here it is assumed that the Stark shift is negative, $S_2\left(t\right) < 0$. The detunings of the pump and Stokes fields are Δ_P and Δ_S respectively. The imaginary term $i\Gamma$ describes the losses from $|2\rangle$ due to spontaneous radiative decay out of the three-level system. Dephasing of state $|3\rangle$, is not included in this model since it is assumed that the pulse durations are much shorter than the decoherence times. This assumption is validated by noting that the decoherence time for NV centres, for example, can be of the order of hundreds of microseconds at room temperature [31]. The Stark shifts of the energy levels for states $|1\rangle$ and $|3\rangle$ are not included here because Stark shifts in ground and meta-stable states tend to be much smaller than those of excited states.

The adiabatic eigenstates of Hamiltonian (3.1) are (for $k = 1, 2, 3$)

$$\beta_k\left(t\right) = \frac{1}{N_k\left(t\right)} \begin{bmatrix} \left[e_k\left(t\right) - \Delta_P - \Delta_S\right]\Omega_P\left(t\right) \\ 2e_k\left(t\right)\left[e_k\left(t\right) - \Delta_P - \Delta_S\right] \\ e_k\left(t\right)\Omega_S\left(t\right) \end{bmatrix}, \tag{3.2}$$

where $e_k\left(t\right)$ are the eigenvalues (which are too cumbersome to present here) associated with each eigenstate. See [53] for full algebraic general solutions to the adiabatic transfer processes in three-level systems.

In Rangelov $et\ al.$ (2005) [16], Gaussian pulse shapes were used for all the pulses, with identical peak values Ω_0 for the Rabi frequencies of the pump and Stokes pulses,

$$\Omega_p\left(t\right) = \Omega_0 e^{-(t-\tau_p)^2/T_P^2}, \tag{3.3}$$

$$\Omega_s(t) = \Omega_0 e^{-(t-\tau_s)^2/T_S^2}, \tag{3.4}$$

$$-S_2(t) = S(t) = S_0 e^{-t^2/T_{St}^2}. \tag{3.5}$$

The peak of the Stark pulse (maximum Stark shift of S_0) is taken to be at $t = 0$, and as such the pump and Stokes pulses peak at times τ_p and τ_s respectively. The pulse durations are determined by T_P, T_S and T_{St}, where it was taken that the pump and Stokes pulses have equal duration $T_P = T_S$ and the Stark pulse has twice their duration $T_{St} = 2T_P$. The unit of time was defined as T_P and the unit of frequency as $1/T_P$. These Gaussian pulses served as exemplars for the initial pulses used in our optimising routine, see section 3.3.

The diabatic energies of the states are

$$E_{|1\rangle} = 0, \tag{3.6}$$

$$E_{|2\rangle} = 2(\Delta_P + S_2(t)), \tag{3.7}$$

$$E_{|3\rangle} = 2(\Delta_P - \Delta_S), \tag{3.8}$$

which with the condition that the Stark shift is negative ($S_2(t) < 0$), dictates that the diabatic energy of state $|2\rangle$, $E_{|2\rangle}$, will only cross those of states $|1\rangle$ and $|3\rangle$ when

$$S_0 > \Delta_P > 0, \tag{3.9}$$

and

$$S_0 > \Delta_S > 0. \tag{3.10}$$

With the condition that the Stark shift is negative two distinct situations can arise: the two-photon detuning can be negative

$$\Delta_P > 0 > (\Delta_P - \Delta_S) > \Delta_P - S_0, \tag{3.11}$$

or positive

$$\Delta_P > (\Delta_P - \Delta_S) > 0 > \Delta_P - S_0. \tag{3.12}$$

In the examples used here to explain the SCRAP technique, and for the pulse optimisation, only the first case (3.11), where the two-photon detuning is negative will be presented (ie. $\Delta_P < \Delta_S$). In the case that the two-photon detuning is positive (3.12), the order of the pulses in standard SCRAP must be run in reverse to what will be shown here [16].

Under the conditions of Equations (3.9), (3.10), and that of Equation (3.11), in order to perform three-state SCRAP, as is shown in [16], both the pump and the Stokes pulses should precede the Stark pulse (Figure 3.2). As can be seen in Figure 3.2 the Stark pulse first causes a crossing of the diabatic energies (3.6)-(3.8) of states
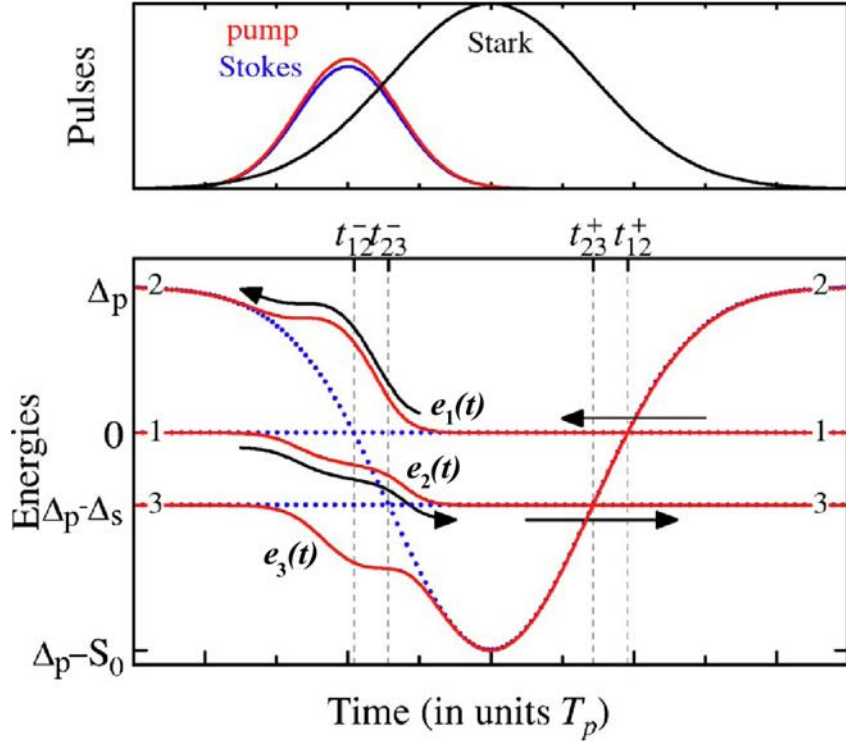
FIGURE 3.2: The top frame shows the ordering of the pulses: pump and Stokes before the Stark pulse. In the lower frame the time evolution of the diabatic (dotted) and adiabatic (solid) energies of the Hamiltonian (in units of $\hbar$) are shown. The arrows from the left shows evolution when the pump and Stokes precedes the Stark pulse, whilst arrows from the right shows evolution when the Stark pulse occurs first. (Figure taken from Rangelov *et al.* [16])

$|1\rangle$ and $|2\rangle$ at time t_{12}^-, and then thereafter a crossing of the diabatic energies of states $|2\rangle$ and $|3\rangle$ at time t_{23}^-. With the pump and Stokes pulses being timed to coincide with the correct crossings, the adiabatic energies follow a path such that the population starting in state $|1\rangle$ ends in state $|3\rangle$, with only a small transient population in state $|2\rangle$ during the transfer. If the pump and Stokes pulses were to occur after the Stark pulse, states $|2\rangle$ and $|3\rangle$ would be connected first and then states $|2\rangle$ and $|1\rangle$, which would not allow population to transfer from state $|1\rangle$ to $|3\rangle$. Figure 3.3 shows how the transient population can be minimised by slightly changing the timing of the pump and Stokes pulses relative to the Stark pulse. Analytic results and detailed reasoning is given in [16]. The pump pulse causes a repulsion between the adiabatic energies $e_1(t)$ and $e_2(t)$, which decreases the energy gap between $e_2(t)$ and $e_3(t)$. This causes an increased probability of non-adiabatic transitions of the population from state $\beta_2(t)$ (which is the adiabatic transfer state) to state $\beta_3(t)$. These non-adiabatic transitions will cause an increase in the population in the fast decaying state $|2\rangle$ (shown in the bottom frame of Figure 3.3). It is clear then that the best option is to have the Stokes pulse precede the pump pulse. The order of the pulses are thus similar to that for STIRAP, but for different reasons.
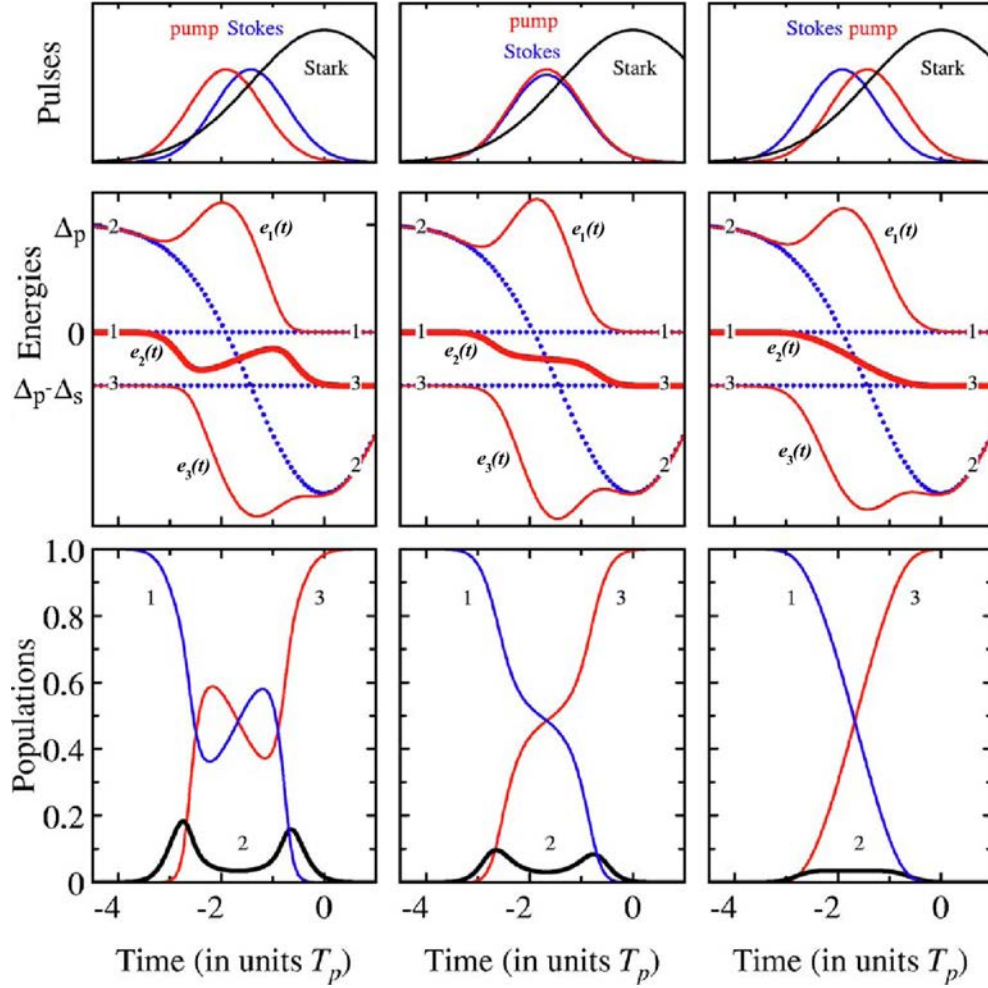
FIGURE 3.3: The top frames show the orderings of the pulses. In the middle frames the time evolution of the diabatic (dotted) and adiabatic (solid) energies of the Hamiltonian are shown (in units of $\hbar$). The heavy line is the actual path the population follows (adiabatic eigenstate $\beta_2(t)$). The bottom frames show the evolution of the population in the diabatic states. The right most setup with the Stokes pulse preceding the pump pulse minimises the population in the short-lived excited state $|2\rangle$. (Figure taken from Rangelov *et al.* [16])

Figure 3.4 shows contour plots of the population in the target state $|3\rangle$ as a function of the single-photon (Δ_P) and two-photon ($\Delta_P - \Delta_S$) detunings. For Figure 3.4 the pulses have the ordering such that the pump pulse is preceded by the Stokes pulse as the Stark pulse rises. This minimises the population in state $|2\rangle$ for the chosen pulse parameters. Even with population loss from state $|2\rangle$ there is a large area with a high fidelity of population transfer. When the two-photon detuning is zero ($\Delta_P - \Delta_S = 0$) there is a band of very high fidelity transfer for a very large range of single-photon detunings Δ_P. This feature is identified with the STIRAP process (see inset in Figure 3.4). Even with high probability of loss from state $|2\rangle$ this band will be unaffected as long as the transfer is adiabatic.

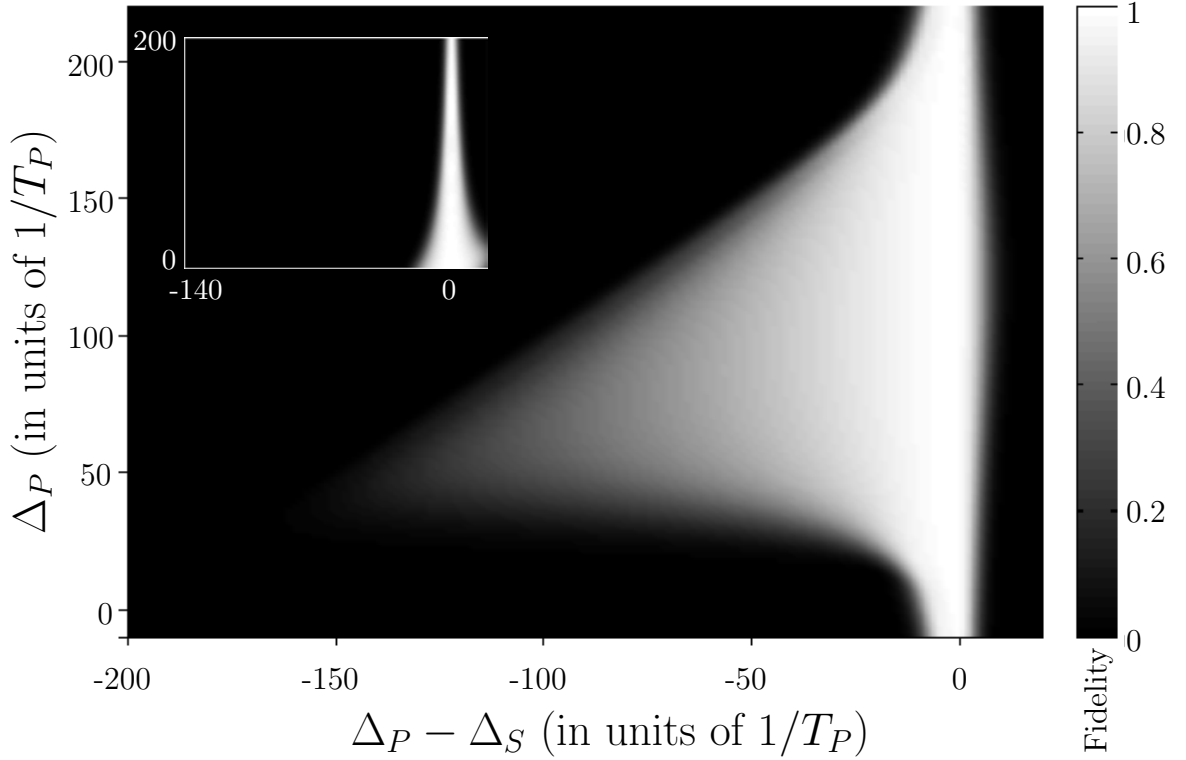Our goal is to achieve efficient state transfer for as wide a variety of detunings as

FIGURE 3.4: The fidelity for a range of detunings, using the original Gaussian pulses for SCRAP (shown as the solid lines in Figure 3.7), with $S_0 = 200/T_P$, $\Omega_0 = 50/T_P$, $T_S = T_P$, $T_{St} = 2T_P$, $\tau_p = -T_P$, $\tau_s = -2T_P$. The decay out of state $|2\rangle$ was $\Gamma = 1/T_p$. The pulses are ordered as to minimise the population in state $|2\rangle$. The inset shows the fidelity when the Stark pulse is switched off, that is the standard STIRAP technique is being performed. It is clear that STIRAP requires two-photon resonance ($\Delta_P - \Delta_S = 0$).

possible, for which SCRAP is the ideal technique. The population transfer for the ideal situation with no decay, and using pulse parameters out of [16] is shown in Figure 3.5. For a more detailed explanation of three state SCRAP please refer to section III in Rangelov *et al.* (2005) [16].

3.2   SCRAP vs STIRAP

When comparing the usefulness of STIRAP and SCRAP the first obvious difference that has already been mentioned is the absolute reliance of STIRAP on two-photon resonance ($\Delta_P - \Delta_S = 0$) between the pump and Stokes fields, where as SCRAP has no such reliance, see Figure 3.4. Furthermore Stark shifts induced by the pump or/and Stokes lasers can prevent two-photon resonance from being possible. We have assumed that these Stark shifts are negligible, which is true only of single-photon transitions. When the pump and Stokes transitions are multiphoton transitions the induced Stark
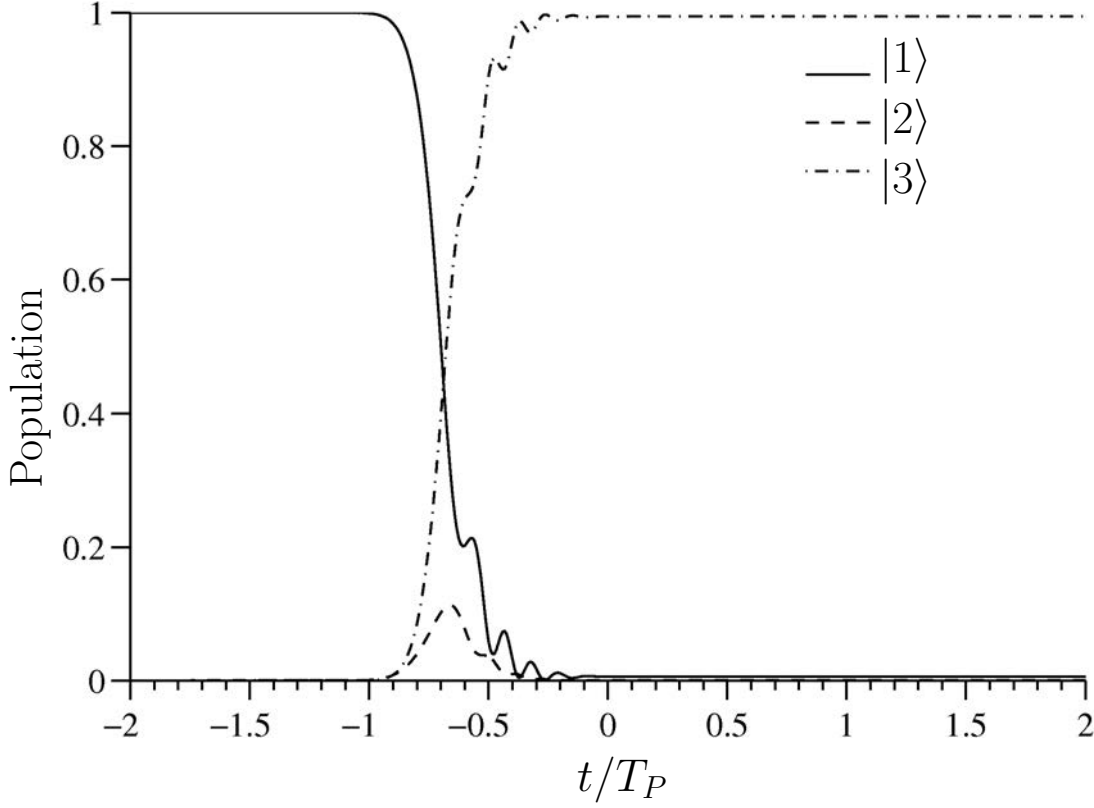
FIGURE 3.5: The evolution of the population in the 3-state-system (state $|1\rangle$ solid line, $|2\rangle$ dashed line and $|3\rangle$ dash-dotted line) where the pulses used were the original Gaussian with the following parameters: $\Delta_P = 30/T_P$, $\Delta_S = 45/T_P$, $S_0 = 200/T_P$, $\Omega_0 = 50/T_P$, $T_S = T_P$, $T_{St} = 2T_P$, $\tau_p = -T_P$, $\tau_s = -2T_P$. There was no decay out of state $|2\rangle$, ($\Gamma = 0$).

shifts can, in general, no longer be neglected. For example when the transition between the ground state $|1\rangle$ and the excited state $|2\rangle$ is a multiphoton transition the pump field induces a Stark shifts $S_{21}(t)$ and $S_{31}(t)$. The effects of such a pump field induced Stark shift on the final population of the target state $|3\rangle$ is presented in Rangelov *et al.* [16]. If we include pump-induced Stark shifts the Hamiltonian 3.1 becomes:

$$H(t) = \frac{\hbar}{2} \begin{bmatrix} 0 & \Omega_P(t) & 0 \\ \Omega_P(t) & 2\left(\Delta_P + S_2(t) + S_{21}^P(t)\right) - i\Gamma & \Omega_S(t) \\ 0 & \Omega_S(t) & 2\left(\Delta_P - \Delta_S + S_{31}^P(t)\right) \end{bmatrix}, \quad (3.13)$$

The Stark shift S_{21}^P is less significant and is taken as zero. The pump-induced Stark shift is directly proportional to the laser intensity and hence also to the pump Rabi frequency $\Omega_p(t)$, thus $S_{31}^P(t) = \sigma\Omega_P(t)$. In Figure 3.6 a plots of the target state ($|3\rangle$) population as a function of the peak pump Rabi frequency Ω_0 is given for several values of σ for both STIRAP and SCRAP. With $\sigma = 0$ there is no induced Stark shift and STIRAP is clearly superior, requiring a smaller peak Rabi frequency in order to obtain complete population transfer. With $\sigma \neq 0$ STIRAP does not deliver complete population transfer
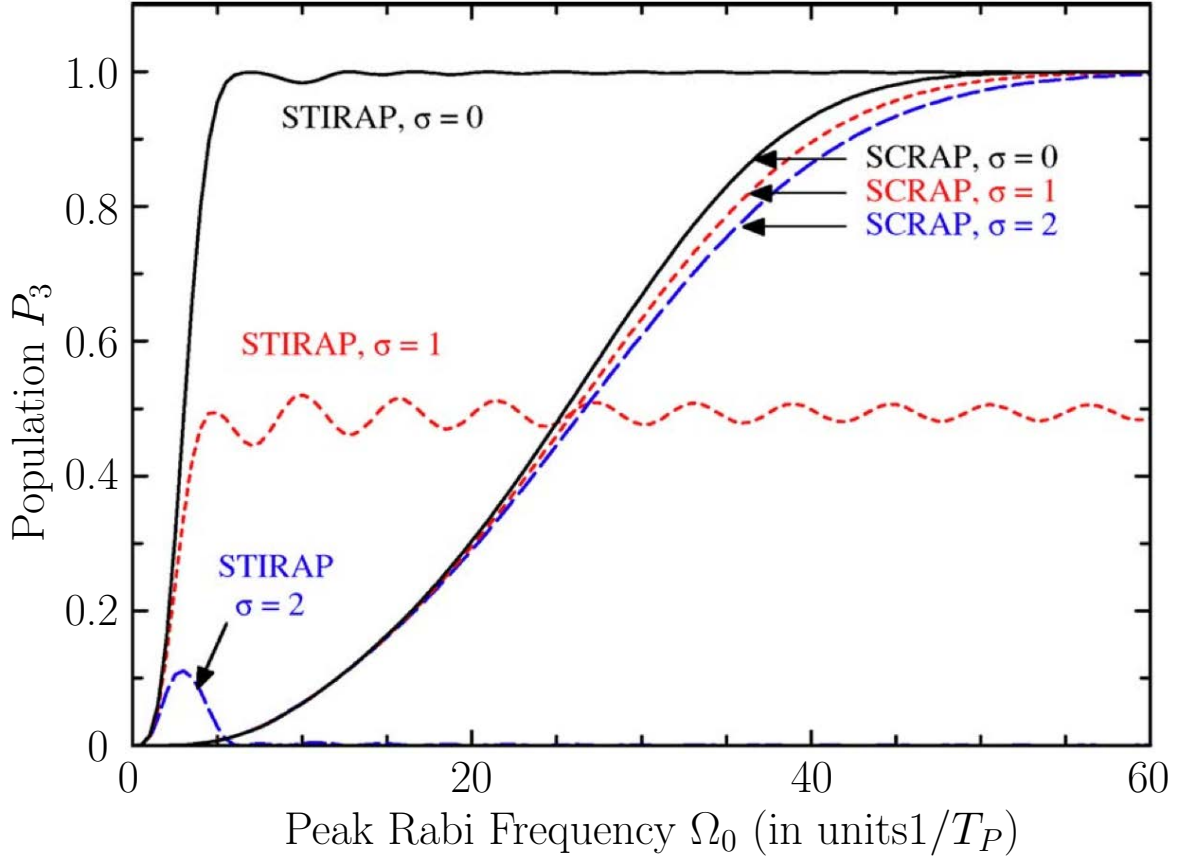
FIGURE 3.6: Final target-state population P_3 vs the peak Rabi frequency Ω_0 for STIRAP ($S_0 = 0$, $\Delta_P = \Delta_S = 0$) and SCRAP ($S_0 = 200/T_P$, $\Delta_P = 50/T_P$, $\Delta_S = -25/T_P$). Three cases of different pump-induced Stark shift $S_{31}^P(t) = \sigma\Omega_P(t)$ of state $|3\rangle$ with respect to state $|1\rangle$ are shown with $\sigma = 0, 1, and 2$. For all cases the other interaction parameters are $\tau_P = -T_P$, $\tau_S = -2T_P$, $T_{St} = 2T_P$, $T_S = T_P$, $\Gamma = 0$.

for *any* peak Rabi frequency, whereas SCRAP still has the desired result with $P_3 = 1$ for large enough Ω_0. SCRAP clearly has a huge advantage over STIRAP when multiphoton transitions are involved during adiabatic population transfer.

Furthermore Chang *et al.* [54] investigated SCRAP as a method to achieve fine state selectivity within multilevel structures and adiabatic passage of quantum superposition states. The system under consideration was a six level λ system where each of the levels in the standard λ level configuration is replaced by a doublet. In such a system each of the two ground state doublets can function as a qubit, creating a two-qubit space. It is found that by using SCRAP, population can be driven from any of the states into any other state, achieving this with STIRAP would require fine frequency control of the pulses. SCRAP allows the adiabatic passage of arbitrary superposition states from the one doublet to the other.

3.3   Optimisation through optimal control

The above mentioned SCRAP process has the advantage that it can tolerate large two-photon detunings, but unlike STIRAP it suffers from decay out of state $|2\rangle$. In this section we will use an optimisation technique, based on the Gradient Ascend Pulse Engineering (GRAPE) algorithm by Khaneja *et al.* (2005) [50], to optimise the transfer fidelity for a set of detunings. The state of the three level system is characterised by the density operator $\rho(t)$ with the Liouville-von Neumann equation of motion

$$\dot{\rho}(t) = -i\left[\left(H_0 + \sum_{k=1}^{m} u_k(t) H_k\right), \rho(t)\right]. \tag{3.14}$$

H_0 is the free evolution Hamiltonian (containing all the terms not dependant on the control fields, e.g. the decay $-i\Gamma$) and the H_k are the Hamiltonians corresponding to the m control fields (in the case of SCRAP these are the Stokes, pump and Stark fields). $u(t) = (u_1(t), u_2(t), \ldots, u_m(t))$ is a vector of control amplitudes, one for each control Hamiltonian. We discretise the transfer time T into N steps of length $\Delta t = T/N$, and assume that the amplitude for each control field is constant during each time step. Instead of optimising these amplitudes directly for each time interval, as described in [50], we define each control field amplitude in terms of q Gaussians,

$$u_k(j) = \sum_{n=1}^{q} h_{n,k} \exp\left[-(j\Delta t - \tau_{n,k})^2/\sigma_{n,k}^2\right], \quad k \in \{1, \ldots, m\} \tag{3.15}$$

that sum to create the pulse for the specific control field, and optimise the parameters of these Gaussians. The aim is to find values for the parameters $(h_{n,k}, \tau_{n,k}, \sigma_{n,k})$ that will, given the initial density operator $\rho(0) = \rho_0$, maximise the overlap of the density operator after a time T, $\rho(T)$, with a target density operator C. The overlap is measured by the standard inner product, thus the performance index Φ_0 is given by

$$\Phi_0 = \langle C|\rho(t)\rangle. \tag{3.16}$$

During each time step j the evolution of the system is given by the propagator

$$U_j = \exp\left[-i\Delta t \left(H_0 + \sum_{k=1}^{m} u_k(j) H_k\right)\right]. \tag{3.17}$$

The performance index can then be written as

$$\Phi_0 = \langle \underbrace{U_{j+1}^\dagger \ldots U_N^\dagger C U_N \ldots U_{j+1}}_{\lambda_j} | \underbrace{U_j \ldots U_1 \rho_0 U_1^\dagger \ldots U_j^\dagger}_{\rho_j} \rangle. \tag{3.18}$$

From Equation (12) in [50] we have that the gradient of the performance index with respect to the control field amplitude is

$$\frac{\delta\Phi_0}{\delta u_k(j)} = -\langle \lambda_j|i\Delta t\,[H_k, \rho_j]\rangle, \tag{3.19}$$

but we are interested in the gradient with regard to $h_{n,k}$, $\tau_{n,k}$ and $\sigma_{n,k}$:

$$
\begin{aligned}
\frac{\delta \Phi_0}{\delta h_{n,k}} &= \sum_{j=1}^{N} \left[\frac{\delta \Phi_0}{\delta u_k(j)} \times \frac{\delta u_k(j)}{\delta h_{n,k}} \right] \\
&= \sum_{j=1}^{N} -\langle \lambda_j | i \Delta t \left[H_k, \rho_j \right] \rangle \times \\
&\qquad\qquad \exp \left[-\left(j \Delta t - \tau_{n,k} \right)^2 / \sigma_{n,k}^2 \right],
\end{aligned}
\tag{3.20}
$$

and similarly

$$
\begin{aligned}
\frac{\delta \Phi_0}{\delta \tau_{n,k}} &= \sum_{j=1}^{N} -\langle \lambda_j | i \Delta t \left[H_k, \rho_j \right] \rangle \times \frac{2 \left(j \Delta t - \tau_{n,k} \right)}{\sigma_{n,k}^2} \times \\
&\qquad h_{n,k} \exp \left[-\left(j \Delta t - \tau_{n,k} \right)^2 / \sigma_{n,k}^2 \right],
\end{aligned}
\tag{3.21}
$$

and

$$
\begin{aligned}
\frac{\delta \Phi_0}{\delta \sigma_{n,k}} &= \sum_{j=1}^{N} -\langle \lambda_j | i \Delta t \left[H_k, \rho_j \right] \rangle \times \frac{2 \left(j \Delta t - \tau_{n,k} \right)^2}{\sigma_{n,k}^3} \times \\
&\qquad h_{n,k} \exp \left[-\left(j \Delta t - \tau_{n,k} \right)^2 / \sigma_{n,k}^2 \right].
\end{aligned}
\tag{3.22}
$$

The performance Φ_0 increases if we choose

$$
h_{n,k} \to h_{n,k} + \epsilon \frac{\delta \Phi_0}{\delta h_{n,k}},
\tag{3.23}
$$

with ϵ a small step size, and similarly for $\tau_{n,k}$ and $\sigma_{n,k}$.

We made use of a Matlab routine "minFuncBC", written by Mark Schmidt (http://www.cs.ubc.ca/~schmidtm/Software/minFunc.html), to perform the final optimisation step (3.23). The "minFuncBC" routine makes use of a quasi-Newton method, the Broyden-Fletcher-Goldfarb-Shanno (BFGS) method, and accepted as input Φ_0 and the vector of derivatives with respect to the optimising parameters, $\left[\frac{\delta \Phi_0}{\delta h_{n,k}}, \frac{\delta \Phi_0}{\delta \tau_{n,k}}, \frac{\delta \Phi_0}{\delta \sigma_{n,k}} \right]$.

3.4 Results

In order to optimise the pulses for as large a detuning space as possible a number of points in the detuning space was used. An initial single point in the detuning space was chosen by searching for the detuning point with optimised pulses that performed the best over the whole chosen detuning space. This entailed calculating the fidelity, using Equation (3.16), for a grid of points in the 2D detuning space $(\Delta_P - \Delta_S, \Delta_P)$, and then taking the average. Once this starting point ($d = 1$) was found a second point ($d = 2$) would be chosen by searching for the second point that, together with the first, would result in the best optimised pulses. Additional points are added to this set until

n	1	2	3	4	5
$\tau_{n,k}$	τ_k	$\tau_k - 0.15T_k$	$\tau_k + 0.15T_k$	$\tau_k - 0.4T_k$	$\tau_k + 0.4T_k$
$\sigma_{n,k}$	$\sqrt{0.2}T_k$	$\sqrt{0.2}T_k$	$\sqrt{0.2}T_k$	$\sqrt{0.25}T_k$	$\sqrt{0.25}T_k$
n		6	7	8	9
$\tau_{n,k}$		$\tau_k - 0.55T_k$	$\tau_k + 0.55T_k$	$\tau_k - T_k$	$\tau_k + T_k$
$\sigma_{n,k}$		$\sqrt{0.2}T_k$	$\sqrt{0.2}T_k$	$\sqrt{0.32}T_k$	$\sqrt{0.32}T_k$

TABLE 3.1: The parameters for each of the 9 Gaussians that constitute each of the pulses. The amplitudes of the Gaussians for a given pulse were all equal: $h_{n,P} = h_{n,S} = 0.23\Omega_0$ and $h_{n,St} = 0.23S_0$.

the enlarging of this set did not result in better pulses (this resulted in d detuning points used for optimisation). The total performance function used for evaluating the efficiency (average fidelity) of the pulses during the optimisation was taken to be the average of the performance functions (3.16) evaluated at each of the d detuning points,

$$\Phi = \frac{1}{d} \sum_{x=1}^{d} \Phi_0 \left(\Delta_P^x, \Delta_S^x \right). \tag{3.24}$$

The gradients required for the optimisation were taken to be the average of the gradients over the set of d detuning points,

$$\frac{\delta\Phi}{\delta h_{n,k}} = \frac{1}{d} \sum_{x=1}^{d} \frac{\delta\Phi_0 \left(\Delta_P^x, \Delta_S^x \right)}{\delta h_{n,k}}, \tag{3.25}$$

and similarly for $\tau_{n,k}$ and $\sigma_{n,k}$.

For the initial pulses used in our optimal control routine we used 9 Gaussians of equal amplitude to approximate each of the original pulse shapes (3.3), (3.4) and (3.5). That is, in Equation (3.15), $q = 9$ and $k \in \{P, S, St\}$ (the probe, Stokes and Stark fields). The parameters of these initial Gaussians are given in Table 3.1. The original pulses (solid lines in Figure 3.7) had the following parameters: $S_0 = 200/T_P$, $\Omega_0 = 50/T_P$, $T_S = T_P$, $T_{St} = 2T_P$, $\tau_P = -T_P$, $\tau_S = -2T_P$, $\tau_{St} = 0$.

It is always possible to increase the success of STIRAP and SCRAP by increasing the maximum Rabi frequency Ω_0. However in SCRAP diabatic evolution is required after the Stark pulse peak, thus placing an upper limit on the maximum Rabi frequency (see Equation(26) in [16]). Furthermore in every experiment there will be physical limits to the maximum Rabi frequency achievable. Once this limit is reached we can then go further to control the specific pulse shapes for both STIRAP and SCRAP to maximise the transfer. To thus provide a fair basis for comparison between STIRAP, SCRAP and the optimised SCRAP we fix identical maximum Rabi frequencies and adjust the pulse shapes. The maximum of the optimised pulses were constrained to
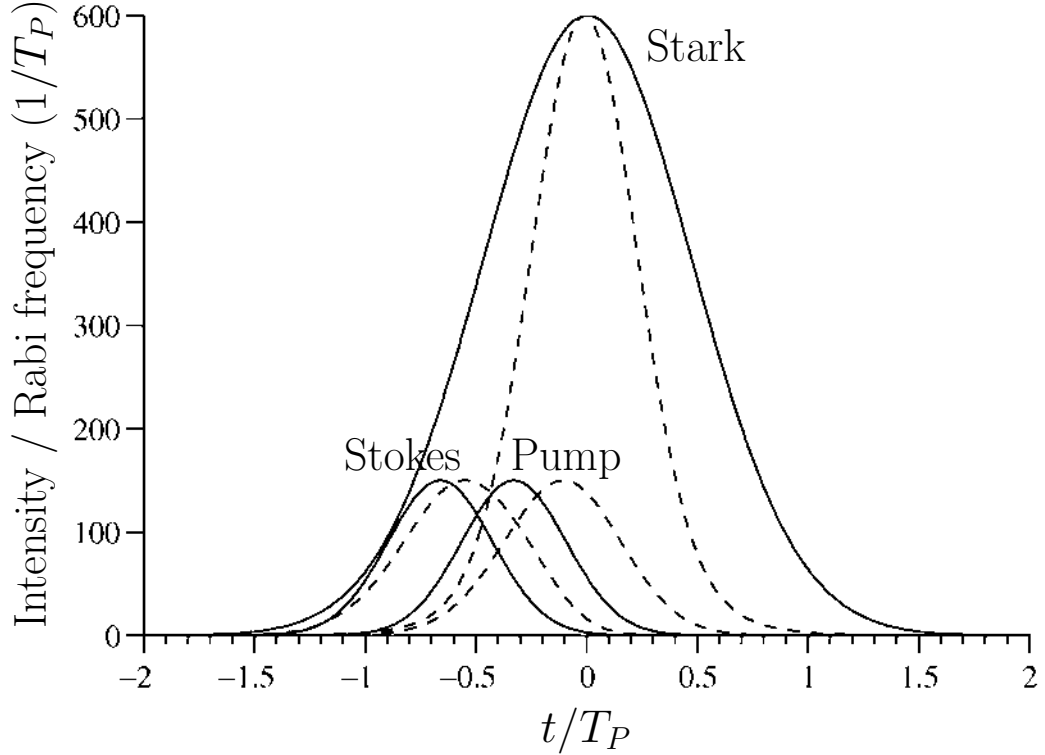
FIGURE 3.7: The original Gaussian pulses (solid lines) with $S_0 = 200/T_P$, $\Omega_0 = 50/T_P$, $T_S = T_P$, $T_{St} = 2T_P$, $\tau_p = -T_P$, $\tau_s = -2T_P$. The dashed lines are the pulses optimised for the detunings indicated in Figure 3.8 by the white dots.

that of the original pulses ($S_0 = 200/T_P$, $\Omega_0 = 50/T_P$). Furthermore the optimisation was constrained to prevent the optimised pulses from becoming too narrow by setting the lower bound on the width of the pulses to 50% of the original pulse width. The optimised pulses obtained numerically are shown as the dashed lines in Figure 3.7. It is interesting to note that the biggest change was in the duration of the Stark pulse. This has the effect that the transfer is more rapid, with the result that there is less decay out of the excited state. The pump and Stokes pulses on the other hand have slightly larger areas.

The optimised pulses were then used to evaluate the fidelity of the population transfer from state $|1\rangle$ to state $|3\rangle$ for a range of detunings, keeping in mind that the chosen pulse ordering restricts the choice of detunings (3.11). As can be seen from Figures 3.4 and 3.8 the total "area" of detunings where population transfer is at all possible (the parts that are not black) is greatly increased when using the optimised pulses. The efficiency of the pulses can be gauged in a number of ways:

1. Measuring the normalised "area" in detuning space (the area of the whole figure is unity) where the pulses result in a population transfer fidelity greater than 0.8.
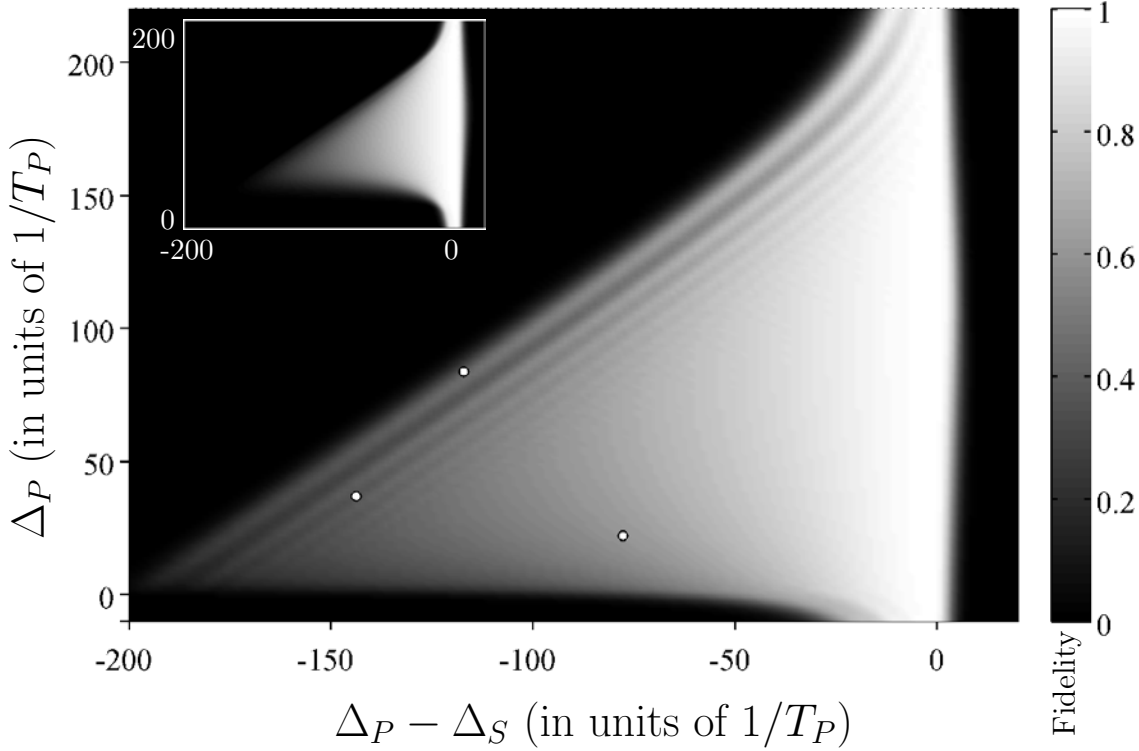
FIGURE 3.8: The fidelity for a range of detunings, using SCRAP pulses optimised for the detunings indicated (white circles) ($d = 3$). The pulses used to generate this figure are the optimised pulses shown as the dashed lines in Figure 3.7. The decay out of state $|2\rangle$ was $\Gamma = 1/T_p$. The inset is a reproduction of Figure 3.4, where the standard SCRAP pulses were used and is included here for easy comparison between the population transfer results of optimised and un-optimised SCRAP.

For the original SCRAP pulses $A_{>0.8}^{ori} = 0.131$, whilst for the optimised pulses $A_{>0.8}^{opt} = 0.178$ was obtained, an increase of 35.5%.

2. Measuring the average fidelity over the whole detuning space, i.e. the sum of the fidelities for each point in the grid that makes up Figure 3.4 and Figure 3.8, divided by the number of grid points. For the original SCRAP pulses $F_{av}^{ori} = 0.219$, whilst for the optimised pulses $F_{av}^{opt} = 0.321$, an increase of 46.6%.

3. In Figure 3.9 a plot of the percentage increase for a grid of points in the detuning space is presented. The $\log_{10}$ of the percentage increase is used since some points had an initial fidelity of virtually zero and ended with a huge percentage increase of $\approx 10^{23}\%$. The area depicted by the red line is the fidelities with a significant value obtained with the optimised SCRAP pulses.

When performing state transfer with SCRAP in an inhomogeneously broadened ensemble it would be important to take into account the profile of the inhomogeneous broadening in order to tailor the optimisation to the problem. This would be done
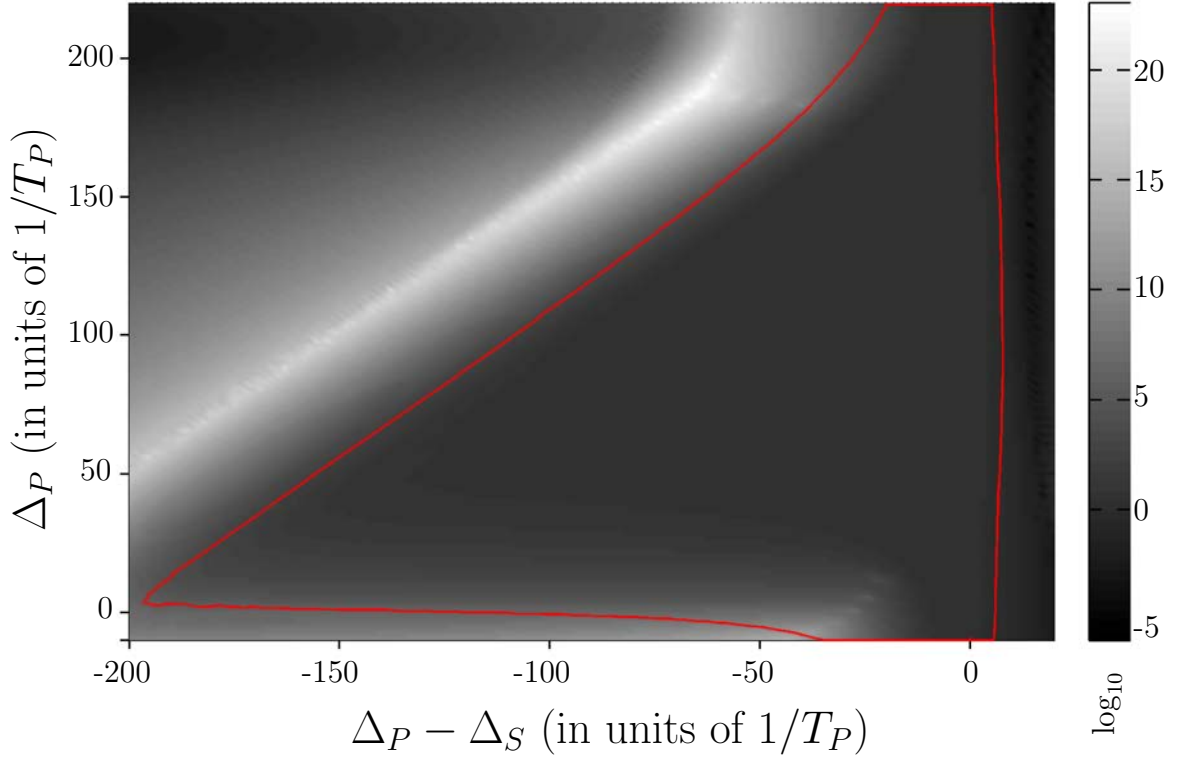
FIGURE 3.9: The $\log_{10}$ of the percentage increase in fidelity between standard SCRAP (Figure 3.4) and optimised SCRAP (Figure 3.8) for each point in the detuning space. The fidelities for optimised SCRAP that are appreciably different from 0 are traced by the red line.

by picking detuning points (Δ_P^x, Δ_S^x) to optimise for from within the zone where the highest fidelity is required.

3.5   Conclusions

It is clear that Stark-shift Chirped Rapid Adiabatic Passage (SCRAP) is a useful process to employ when trying to overcome inhomogeneous broadening of energy levels in a system undergoing state transfer. SCRAP, unlike STIRAP, does not require exact two-photon resonance and it is because of this property that SCRAP is relatively insensitive to inhomogeneous broadening and AC-Stark shifts induced by the pump or Stokes lasers.

STIRAP is an adiabatic passage technique that is closely related to EIT, one of the principal ways of slowing and stopping light pulses within a medium. It should in principle be possible to implement a version of EIT with an additional Stark-shift inducing pulse that operate in a way similar to SCRAP, with the same advantages of SCRAP for inhomogeneously broadened media. Translating and implementing SCRAP in the quantum domain would require that the pump pulse be replaced by a quantum

probe field carrying quantum information that is to be stored in the spin coherence of the atomic system. In solid state systems inhomogeneous broadening is far more severe than in atomic molecular systems. As mentioned in section 2.3.2 pulse storage time is limited by the different dephasing rates for each centre implied by the ground state inhomogeneous width.

In summary we have shown that by using an optimum control technique reminiscent of that used by Khaneja *et al.* [50] standard SCRAP pulses can be optimised so that a larger inhomogeneous broadening can be compensated for, thus increasing the overall fidelity of state transfer in an inhomogeneously broadened medium.

4

Quantum phase gate schemes

Photons are obvious candidates for the implementation of quantum information processing systems. They are robust against decoherence and single-qubit operations are easy to implement. Lloyd [55] showed that nearly any two-qubit gate, together with single qubit gates, complete the universal set of gates required for quantum computing [56]. In optical quantum computing the two-qubit gates considered are usually the controlled-phase gate (CZ and also referred to as C-sign or CPHASE) or the controlled-NOT (CNOT) gate. These two-qubit gates are much more of a challenge to implement than the single qubit gates due to the extremely weak interaction between photons. There are two approaches to implement an optical quantum phase gate (QPG): the first (described in section 4.1) was introduced by Knill, Laflamme and Milburn (the KLM scheme) [1], and is a probabilistic measurement based scheme. That is, successful execution of the gate is heralded by a measurement that has a probabilistic outcome. The second scheme (described in section 4.2) employs extremely large cross-Kerr nonlinearities to achieve strong photon-photon interactions and hence can realise a conditional phase shift of the fields required for the thus implementation of a phase gate. Such large cross-Kerr optical nonlinearities are typically very difficult to achieve in physically realistic systems. In section 4.3 we describe a third scheme which is very similar to the KLM scheme except that the probabilistic measurements in the KLM scheme are replaced by quantum nondemolition measurements which are performed with the aid of weak cross-Kerr interaction. This scheme is nearly deterministic and relies on extremely good single photon detectors.
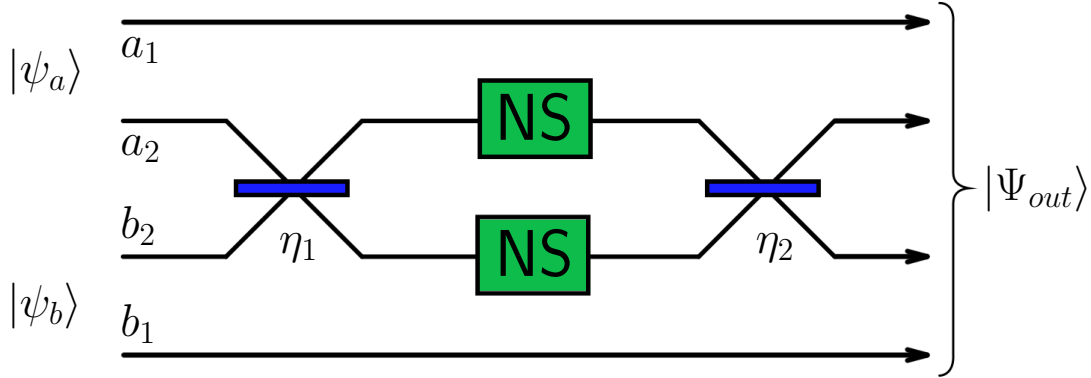
FIGURE 4.1: Circuit diagram for the KLM scheme CZ gate. The gate is comprised of two 50:50 beam splitters η_1 and η_2 (that is they have transmission coefficients equal to $1/\sqrt{2}$) and two nonlinear sign flip gates (NS). The output state $|\Psi_f\rangle$ is not necessarily a separable state (i.e. it is an entangled state).

4.1 KLM gate using linear optics

The Knill, Laflamme, Milburn (KLM) [1] scheme is based on linear optics only, and makes use of the inherent nonlinearity of measurement and single photon generation in order to realise the necessary two-qubit operations. In order to efficiently integrate a KLM gate into a quantum circuit fast feedforward is required. The specific two-qubit gate implemented by the KLM scheme is the conditional sign flip gate (C-sign) which is also known as a CZ gate. The CZ gate is defined by the transformation

$$|a\rangle |b\rangle \rightarrow (-1)^{ab} |a\rangle |b\rangle , \tag{4.1}$$

where $a, b = \{0, 1\}$ are the Fock states of individual photonic modes, and the CZ gate is a maximally-entangling gate. That is, it is possible to prepare two qubits in a maximally entangled state using a CZ gate. The KLM CZ gate is performed by a circuit comprised of two 50:50 beam splitters (BS) and two nonlinear sign flip (NS) gates as depicted in Figure 4.1. The working of these two elements of the KLM CZ gate is described in the next section. The two input qubits are described by the states $|\psi_a\rangle$ and $|\psi_b\rangle$. Considering the transformation (4.1) performed by the CZ gate it is clear that if and only if *both* qubits are in state $|1\rangle$ will the sign of the output state be different from the input state. The encoding in the figure is such that if there is a photon present in mode a_1 (i.e. $|1\rangle_{a_1} \otimes |0\rangle_{a_2}$) then the logical state of the first qubit is $|\psi_a\rangle = |0\rangle_a$ and if there is a photon in mode a_2 (i.e. $|0\rangle_{a_1} \otimes |1\rangle_{a_2}$) then the logical state is $|\psi_a\rangle = |1\rangle_a$. This is also known as a dual-rail encoding. Similarly a single photon in either the b_1 or b_2 modes equate to logical states $|0\rangle_b$ or $|1\rangle_b$ of the second qubit. Of course in general $|\psi_a\rangle$ and $|\psi_b\rangle$ are superpositions of states.

The detailed explanation of the functioning of the KLM CZ gate is presented in section 4.1.2. A CZ gate is easily transformed into a CNOT gate by placing Hadamard gates (which are single-qubit gates) on the target qubit before and after the CZ gate.
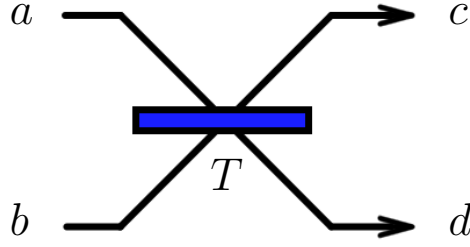
FIGURE 4.2: Diagram of a beam splitter with input modes a and b and output modes c and d. The beam splitter is characterised by its transmission coefficient T.

Single-qubit gates are easy to execute on optical qubits (performed with beam splitters and phase shifter (wave plates) optical elements) and as such if one can perform a CZ gate a CNOT gate is available. To see how the CZ gate works we will look at its constituent elements one at a time.

4.1.1   KLM gate components

First we consider the beam splitter optical element, depicted in Figure 4.2. The reflection and transmission coefficients (R and T respectively) of a symmetric beam splitter satisfy the following conditions:

$$|R|^2 + |T|^2 = 1 \quad \text{and} \quad RT^* + TR^* = 0. \tag{4.2}$$

The input modes a and b are then related to the output modes c and d by

$$\hat{a} = R\hat{c} + iT\hat{d} \tag{4.3}$$

$$\hat{b} = iT\hat{c} + R\hat{d}. \tag{4.4}$$

The 50:50 beam splitter divides the field from an input mode evenly between the two output modes thus resulting in reflection and transmission coefficients $T = R = 1/\sqrt{2}$. Considering only a single input mode a carrying a single photon the 50:50 beam splitter has the following effect:

$$\begin{aligned}
|1\rangle_a &= \hat{a}^\dagger |0\rangle_a \\
&\to 1/\sqrt{2} \left(\hat{c}^\dagger + \hat{d}^\dagger \right) |0,0\rangle_{cd} \\
&= 1/\sqrt{2} \left(|1,0\rangle_{cd} + |0,1\rangle_{cd} \right),
\end{aligned} \tag{4.5}$$

where $\hat{a}^\dagger$, $\hat{b}^\dagger$, $\hat{c}^\dagger$, $\hat{d}^\dagger$ are the creation operators for the respective modes. The single input photon is now in a superposition of being in the two output modes. The KLM scheme however has two modes as inputs for each of the beam splitters with the possibility of a photon in each of the input modes. With a single photon in each of the input modes
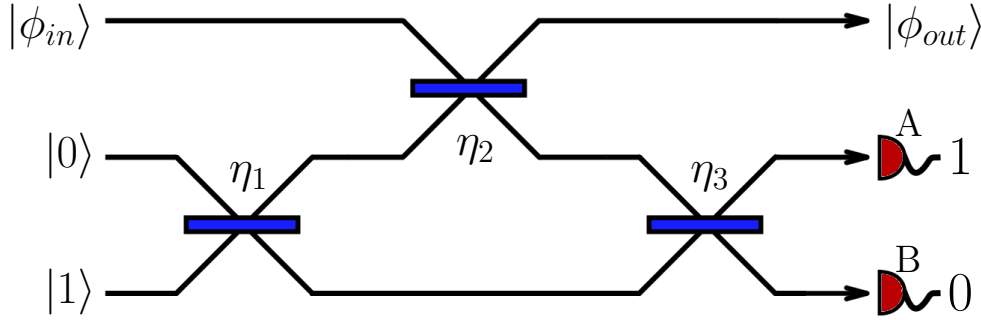
FIGURE 4.3: Circuit diagram for the KLM scheme NS gate, consisting of three beam splitters and two ancilla modes. The gate is successfully implemented when a photon is detected at detector A, and no photon at detector B.

a and b a 50:50 beam splitter results in a superposition of two-photon states in the output modes c and d:

$$|1,1\rangle_{ab} = \hat{a}^\dagger \hat{b}^\dagger |0,0\rangle_{ab} \tag{4.6}$$
$$\rightarrow 1/2 \left(\hat{c}^\dagger + \hat{d}^\dagger\right)\left(\hat{c}^\dagger - \hat{d}^\dagger\right)|0,0\rangle_{cd}$$
$$= 1/2 \left(\hat{c}^{\dagger 2} - \hat{d}^{\dagger 2}\right)|0,0\rangle_{cd}$$
$$= 1/\sqrt{2}\left(|2,0\rangle_{cd} - |0,2\rangle_{cd}\right). \tag{4.7}$$

This bunching of the photons into either one of the two output modes is called the Hong-Ou-Mandel effect [57] and is due to destructive interference between the two probability amplitudes of the $|1,1\rangle_{cd}$ output states.

The remaining element of the CZ gate is the nonlinear sign flip (NS) gate, depicted in Figure 4.3, that flips the sign of states with two photons. This gate consists of three beam splitters with transmission amplitudes $\eta_1 = \eta_3 = 1/(4-2\sqrt{2})$ and $\eta_2 = 3-2\sqrt{2}$ [1, 58]. The NS gate involves two ancillary modes and projective measurement, resulting in a success probability for the gate of 1/4. With the inclusion of feed forward this success probability can be increased, with one round of feed forward resulting in a success probability of 0.272 [59]. The first ancillary mode starts in the vacuum state $|0\rangle$ whilst the other carries a single photon $|1\rangle$ initially. Successful operation of the gate is heralded by the detection of a single photon at detector A and no photon at detector B. The action of the NS gate is to flip the sign of the two photon Fock state and leave the vacuum and single photon Fock states unchanged. As such the action of the NS gate on a general input state in a superposition of zero, single and two-photon Fock states is:

$$|\phi_{in}\rangle = \alpha|0\rangle + \beta|1\rangle + \gamma|2\rangle$$
$$\rightarrow \alpha|0\rangle + \beta|1\rangle - \gamma|2\rangle. \tag{4.8}$$

Of note is that the amplitudes of the states are left unchanged by the NS gate. The effect of the NS gate on higher Fock states is irrelevant to the discussion of the CZ gate since the output mode from the beam splitter preceding the NS gate will never carry more than two photons if the input states are perfect single photon states. Sanaka *et al.* [60] experimentally realised a NS gate with a phase shift of $(1.05 \pm 0.06)\pi$, in very good agreement with the perfect NS gate shift of π. The experimentally realised success probability for the gate execution was 10^{-5}, mostly due to the use of imperfect single photon sources. They however used 50:50 beam splitters instead of the transmission amplitudes suggested by the KLM scheme. The use of non-optimal beam splitter transmission amplitudes had the effect of decreasing the theoretical maximum success probability of the NS gate to 1/8.

4.1.2   KLM gate functioning

In order to understand the operation of the KLM CZ gate let us now consider a general logical input state for the gate where both input qubits are in superposition states. We explore how the constituent elements of the KLM CZ gate act on the input state

$$\begin{aligned}
|\psi\rangle &= |\psi_a\rangle \otimes |\psi_b\rangle \\
&= (\alpha |0\rangle_a + \beta |1\rangle_a)(\gamma |0\rangle_b + \delta |1\rangle_b),
\end{aligned} \tag{4.9}$$

where $\alpha^2 + \beta^2 = 1$ and $\gamma^2 + \delta^2 = 1$. As we have said above the logical states correspond to single photons in the input mode basis (dual rail encoding) as follows: $|0\rangle_a = |0,1\rangle_{a_1 a_2}$, $|1\rangle_a = |1,0\rangle_{a_1 a_2}$, $|0\rangle_b = |0,1\rangle_{b_1 b_2}$ and $|1\rangle_b = |1,0\rangle_{b_1 b_2}$. The input state $|\psi\rangle$ can then be written as

$$\begin{aligned}
|\psi_a\rangle \otimes |\psi_b\rangle &= \left(\alpha |0,1\rangle_{a_1,a_2} + \beta |1,0\rangle_{a_1,a_2}\right)\left(\gamma |0,1\rangle_{b_1,b_2} + \delta |1,0\rangle_{b_1,b_2}\right) \\
&= \alpha\gamma |0,1,0,1\rangle + \beta\gamma |1,0,0,1\rangle + \alpha\delta |0,1,1,0\rangle + \beta\delta |1,0,1,0\rangle, \tag{4.10}
\end{aligned}$$

where we have dropped the subscripts. Modes a_1 and b_1 now pass through the beam splitter transforming the input state according to Equation (4.6) into

$$\begin{aligned}
&\alpha\gamma |0,1,0,1\rangle + \frac{\beta\gamma}{\sqrt{2}}\left(|1,0,0,1\rangle + |0,0,1,1\rangle\right) \\
&+ \frac{\alpha\delta}{\sqrt{2}}\left(|1,1,0,0\rangle - |0,1,1,0\rangle\right) + \frac{\beta\delta}{\sqrt{2}}\left(|2,0,0,0\rangle - |0,0,2,0\rangle\right). \tag{4.11}
\end{aligned}$$

Clearly according to Equation (4.8) the NS gate (when successfully implemented) will merely flip the sign of the last term. The effect of the second beam splitter is to recreate the original states through destructive interference:

$$\begin{aligned}
&\alpha\gamma |0,1,0,1\rangle + \frac{\beta\gamma}{\sqrt{2}\sqrt{2}}\left(|1,0,0,1\rangle + |0,0,1,1\rangle\right) + \frac{\beta\gamma}{\sqrt{2}\sqrt{2}}\left(|1,0,0,1\rangle - |0,0,1,1\rangle\right) \\
&+ \frac{\alpha\delta}{\sqrt{2}\sqrt{2}}\left(|1,1,0,0\rangle + |0,1,1,0\rangle\right) - \frac{\alpha\delta}{\sqrt{2}\sqrt{2}}\left(|1,1,0,0\rangle - |0,1,1,0\rangle\right) \\
&- \frac{\beta\delta}{\sqrt{2}}\left(1/\sqrt{2}|1,0,1,0\rangle + 1/\sqrt{2}|1,0,1,0\rangle\right) \\
&= \alpha\gamma |0,1,0,1\rangle + \beta\gamma |1,0,0,1\rangle + \alpha\delta |0,1,1,0\rangle - \beta\delta |1,0,1,0\rangle. \tag{4.12}
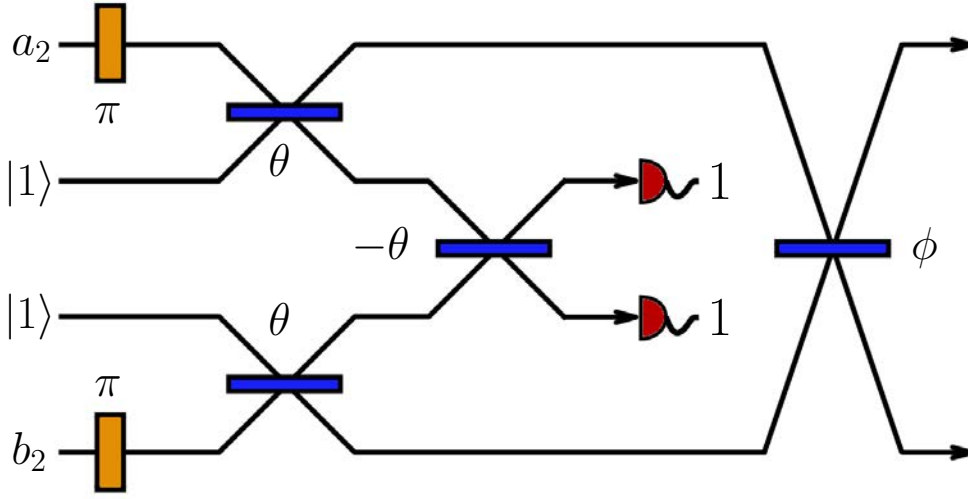\end{aligned}$$

FIGURE 4.4: Circuit diagram for the improved KLM scheme CZ gate [61]. This scheme uses two ancilla photons and two detected photons with beam splitters with beam splitter angles $\theta = 54.74°$ and $\phi = 17.63°$. Modes a_2 and b_2 are the two modes that carry the single photon components of the two input qubits $|\psi_a\rangle$ and $|\psi_b\rangle$. Modes a_1 and b_1 are not shown, they do not interact with any component just as in Figure 4.1.

Which is exactly the input state (4.10) but with the sign of the logical $|1\rangle_a |1\rangle_b$ state (which in the dual rail encoding is $|1, 0, 1, 0\rangle$) flipped. Thus these transformations perform exactly the operation that define the CZ gate [Equation (4.1)].

In a subsequent paper by Knill [61] the scheme was improved by using two ancilla photons, and two detected photons, see Figure 4.4. This scheme made use of beam splitters with beam splitter angles $\theta = 54.74°$ and $\phi = 17.63°$ which correspond to transmission coefficients $\cos \theta$ and $\cos \phi$ and reflection coefficients $\sin \theta$ and $\sin \phi$. Only the modes that correspond to the logical $|1\rangle$ state, modes a_2 and b_2, are shown in the figure. The modes for logical $|0\rangle$, modes a_1 and b_1, are omitted since they do not interact with any component of the gate. Modes a_2 and b_2 are also referred to as the control and target modes respectively. Before entering the beam splitters the control and target modes first pass through phase shifters that induce a π phase shift. The improved KLM linear optical scheme results in an improved probability of 2/27 to successfully implement a CZ gate. The success of the gate is heralded by detection of a single photon in each of the detectors.

Main difficulties with the KLM scheme are in its reliance on the availability of efficient single photon sources and good single photon detectors. Integral to the functioning of the KLM scheme is the nonlinear sign flip operation (NS) which has a success probability of 1/4. The original version of the KLM scheme as outlined in the original paper [1] used two NS gates and as such the probability of successfully executing the two-qubit gate was only 1/16. These already severe limitations exclude the further

constraints imposed by imperfect detectors and single photon sources. Knill [62] later showed that the highest possible success probability for a NS gate is 1/2.

Several improvements and alternatives to the original KLM scheme CZ gate have been proposed and demonstrated with probabilities of success up to 1/4. These implementations with high success probabilities are destructive in nature: the quantum state is destroyed by the quantum gate. For certain applications this is not detrimental, for example the Bell measurement in teleportation still results in the teleportation of the photon even if the two-photon gate was a destructive gate. The destructive CNOT gate demonstrated by Pittman *et al.* [63] makes use of an ancilla qubit and has a theoretic probability of success of 1/4. Ralph *et al.* [64] proposed a destructive gate, experimentally demonstrated by O'Brien *et al.* [65], that requires no ancilla qubits and has a probability of success of 1/9. Success is heralded by the detection of a single photon in each of the control and target outputs.

A non-destructive CNOT gate that consists of a destructive CNOT gate together with a probabilistic parity check gate was proposed by Pittman *et al.* [66]. The gate is implemented successfully with a theoretic probability of up to 1/4. Zhao *et al.* [67] experimentally demonstrated this gate; the first experimental realisation of a non-destructive CNOT gate in linear optics. The experiment made use of a pair of entangled ancilla photons, and also demonstrated that the CNOT gate can be used to entangle states.

With the advance of technology the quality and reliability of single photon sources and detectors will improve, thus improving the fidelity of linear optics two-qubit gates. The remaining drawback of these linear optical quantum computing schemes are their probabilistic nature and the massive overhead that this implies together with the overhead of error correction. Linear optics quantum computing would be well suited however for preparing cluster-states for one-way computing.

4.2 QPG using a large Kerr nonlinearity

Optical nonlinearities provide one way of getting around the very weak interaction between photons that make them such ideal information carriers yet problematic candidates for implementing two-qubit gate operations. One way to enhance the interaction between two photons is through a $\chi^{(3)}$ nonlinear medium that induces a cross-Kerr effect between the two interacting fields. This is often called cross-phase modulation (XPM). Making use of a cross-Kerr nonlinearity to obtain the required photon-photon interaction for the operation of a logical quantum gate was first suggested by Milburn [68] in a paper describing how to perform an optical Fredkin gate, a reversible gate that performs a controlled swap.

The ideal cross-Kerr effect has the interaction Hamiltonian

$$H_K = \hbar\chi\hat{a}^\dagger\hat{a}\hat{b}^\dagger\hat{b}, \tag{4.13}$$

where $\hat{a}$ and $\hat{b}$ are the annihilation operators of the two modes. Using the same dual rail encoding as for the KLM scheme CZ gate in section 4.1 (logical $|0\rangle \to |1,0\rangle_{a_1,a_2}$ and $|1\rangle \to |0,1\rangle_{a_1,a_2}$), a CZ gate can be executed by having modes a_2 and b_2 pass through
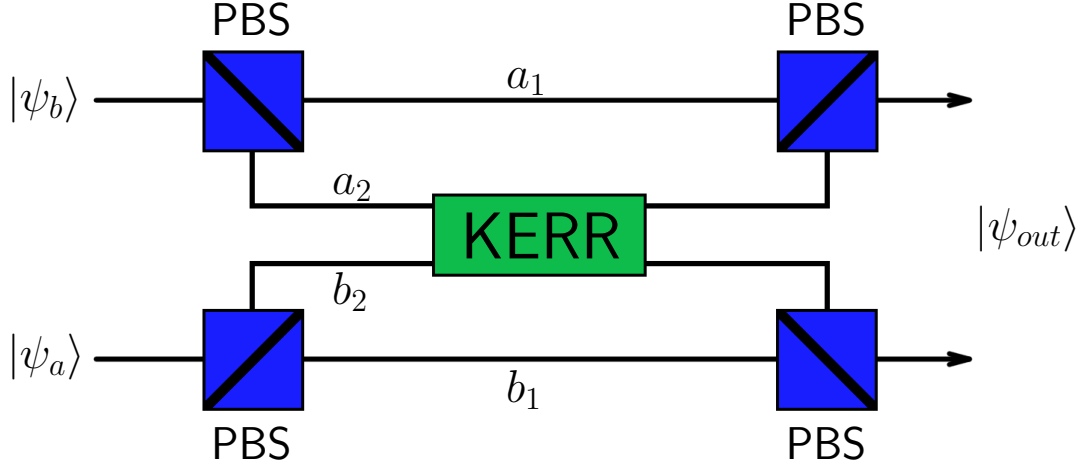
FIGURE 4.5: Circuit diagram of the nonlinear QPG employing a nonlinear Kerr medium to induce a conditional phase shift. With a phase shift of π this gate would be a CZ gate. The polarising beam splitters (PBS) split the input states into their horizontal and vertical components. The output state is entangled.

the Kerr medium. The Hamiltonian (4.13) applied to modes a_2 and b_2 results in the unitary evolution

$$\hat{U}_K = \exp\left[i\chi\hat{a}_2^\dagger\hat{a}_2\hat{b}_2^\dagger\hat{b}_2 t\right], \tag{4.14}$$

that has the general action on Fock (number) states:

$$\hat{U}_K |n_a, n_b\rangle = \exp\left[i\chi n_a n_b t\right] |n_a, n_b\rangle. \tag{4.15}$$

When this unitary evolution is applied to the same input state (4.10) that we used for the KLM scheme in order to see how an arbitrary state is transformed we obtain:

$$\begin{aligned}
|\psi\rangle \to &\hat{U}_K |\psi\rangle \\
=&e^{i\chi\hat{a}_2^\dagger\hat{a}_2\hat{b}_2^\dagger\hat{b}_2 t}\left[\alpha\gamma |0,1,0,1\rangle + \beta\gamma |1,0,0,1\rangle + \alpha\delta |0,1,1,0\rangle + \beta\delta |1,0,1,0\rangle\right] \\
=&\alpha\gamma |0,1,0,1\rangle + \beta\gamma |1,0,0,1\rangle + \alpha\delta |0,1,1,0\rangle + e^{i\chi t}\beta\delta |1,0,1,0\rangle. \tag{4.16}
\end{aligned}$$

Clearly the effect of the nonlinear medium is to induce a phase shift ($\phi = \chi t$) on the two modes if and only if both of them are occupied. This phase shift is also referred to as a conditional phase shift (CPS) since it is conditional on the presence of *both* fields. When the cross-Kerr nonlinearity in this quantum phase gate (QPG) is large enough, or the interaction time is long enough, such that the conditional phase shift is $\phi = \pi$ we obtain $e^{i\phi} \to -1$ which results exactly in a CZ or sign flip gate. An example of how this gate could be implemented in practice (depicted in Figure 4.5) is with polarisation qubits where the qubit is for example the horizontal and vertical polarisation states, i.e. the state of qubit $|\psi_a\rangle$ is in general given by $|\psi_a\rangle = \alpha |H\rangle + \beta |V\rangle$. Polarising beam

splitters acting on the two qubits a and b split them into their horizontal and vertical components resulting in a dual rail encoding of the qubit states. The modes, a_2 and b_2, that correspond to logical $|1\rangle$ for qubits $|\psi_a\rangle$ and $|\psi_b\rangle$ then pass through the Kerr medium. The use of polarising beam splitters then again combine the horizontally and vertically polarised fields of the qubits into a single mode each.

We now define the conditional phase shift in a more general sense. Here logical $|0\rangle$ and $|1\rangle$ are defined as "no photon present" and "single photon present" respectively. We then have the following truth table for the phase shifts [69]:

$$
\begin{aligned}
|0\rangle_P |0\rangle_T &\to e^{-i\left(\phi_0^P + \phi_0^T\right)} |0\rangle_P |0\rangle_T \equiv e^{-i\phi_{00}} |0\rangle_P |0\rangle_T \\
|0\rangle_P |1\rangle_T &\to e^{-i\left(\phi_0^P + \phi_0^T + \phi_{lin}^T\right)} |0\rangle_P |1\rangle_T \equiv e^{-i\phi_{01}} |0\rangle_P |1\rangle_T \\
|1\rangle_P |0\rangle_T &\to e^{-i\left(\phi_0^P + \phi_{lin}^P + \phi_0^T\right)} |1\rangle_P |0\rangle_T \equiv e^{-i\phi_{10}} |1\rangle_P |0\rangle_T \\
|1\rangle_P |1\rangle_T &\to e^{-i\left(\phi_0^P + \phi_{lin}^P + \phi_{nlin}^P + \phi_0^T + \phi_{lin}^T + \phi_{nlin}^T\right)} |1\rangle_P |1\rangle_T \equiv e^{-i\phi_{11}} |1\rangle_P |1\rangle_T .
\end{aligned}
\tag{4.17}
$$

When there is no field or the field does not interact with the non-linear medium, (e.g. it is off resonant with the relevant transitions) there is only the vacuum phase shift ϕ_0. When one field interacts with the system, but the other field does not (again not present or off resonant), there is the linear phase shift ϕ_{lin} and the vacuum shift. Only when both fields are present is the non-linear phase shift ϕ_{nlin} observed, but the linear and vacuum phase shift are still present. The conditional phase shift is defined by the non-linear phase shifts, ϕ_{nlin} [69, 70]:

$$
\begin{aligned}
\phi_{cps} &= \phi_{11} - \phi_{10} - \phi_{01} + \phi_{00} \\
&= \phi_{nlin}^P + \phi_{nlin}^T.
\end{aligned}
\tag{4.18}
$$

In order to implement a nonlinear CZ gate a CPS of ($\phi_{cps} = \pi$) is required. Such a large CPS requires an extremely large nonlinearity compared to that of typical non-linear materials, for example recently Matsuda *et al.* [71] reported a phase shift of $1 \times 10^{-7} - 1 \times 10^{-8}$ radians for weak coherent pulses with an average of one photon per pulse in optical fibres of length 4.7 m. It is this requirement that motivated the invention of the KLM scheme. A naive solution to realise an appreciable cross phase modulation of the two fields is to increase the interaction region of the Kerr medium. This solution is unfortunately defeated by the increase in losses in the system and noise induced in the phase shift [72] and the extreme length of medium (could be kilometres) that would be required. The remaining solution is then to find or engineer sufficiently large optical nonlinearities. It has been found that optical nonlinearities can be greatly enhanced in systems exhibiting electromagnetically induced transparency (EIT) [73] in an ensemble of atoms when the two-photon resonance condition is slightly disturbed, for example by the introduction of extra energy level(s) [74, 75] or if the EIT fields are simply not exactly tuned on two-photon resonance [76, 77]. Proposals for systems with EIT enhanced nonlinearies make use of a variety of energy level schemes: three-level Λ [6, 78, 79], V [80] and Ξ [81]; four-level tripod [82–84], N [74, 85] and inverted Y [86]; five-level tripod [87] and M [88–90]. The tripod and M schemes have a great advantage in that the group velocity of the two fields undergoing XPM can be matched.

Experiment	Details	n_2 (cm^2/W)	CPS
Turchette *et al.* (1995) [69]	Single Cs, V-type, CQED	NA	$(16 \pm 3)°$
Wang *et al.* (2001) [78]	^{87}Rb vapour, Λ-type	7×10^{-6}	NA
Kang *et al.* (2003) [91]	^{87}Rb cloud, N-type	NA	$7.5°$
Chang *et al.* (2004) [92]	hot ^{87}Rb vapour, Λ-type	9.6×10^{-6}	$198°$
Li *et al.* (2008) [93]	^{87}Rb cloud, 4lvl tripod	$\sim 2 \times 10^{-5}$	$\sim 5°$
Han *et al.* (2008) [94]	cold ^{87}Rb cloud, 4lvl tripod	7.2×10^{-5}	$\sim 0.6°$

TABLE 4.1: We present the nonlinear indices of refraction (n_2) and conditional phase shifts (CPS) from publications on experiments in nonlinear optics with a variety of level schemes. Most of the experiments made use of ^{87}Rb atoms in either a hot vapour or cold cloud form. Not every experiment reported both n_2 and the CPS (NA in the table).

The two fields then have a longer time during which they interact via the nonlinearity, thus greatly enhancing the phase shifts achievable in these systems for the same field strengths. The four-level tripod scheme is discussed in more detail in chapter 5 where we explore a novel system where a quantum phase gate can be implemented.

In Table 4.1 we present the results obtained for the nonlinear indices of refraction (n_2) and CPS from experiments in nonlinear optics where a variety of level schemes were investigated. It is important to realise that direct comparison of these results should be done cautiously. The nonlinear index of refraction and the strength of the cross-Kerr interaction χ, and hence the CPS, depends on the Rabi frequency of the probe and/or trigger fields, that is, the strength of the fields play a crucial role in the results. For the purposes of quantum computing with photonic qubits (obviously so for single photon fields) weak fields are preferred. For example the 1.1π radian phase shift obtained by Chang *et al.* [92] in a Λ-type level scheme made use of fields with Rabi frequencies $\Omega_p = 2\pi \times 31$MHz for the probe field and $\Omega_c = 2\pi \times 75$MHz for the coupling field whereas the $7.5°$ phase shift obtained by Kang *et al.* [91] in the N-type scheme had Rabi frequencies $\Omega_p = 0.1$MHz for the probe field, $\Omega = 3$MHz for the signal field and $\Omega_c = 2$MHz for the coupling field.

A scheme developed by Wang *et al.* in Rb atoms [95], using a five atomic level scheme, makes use of double EIT (i.e. there are two Λ subsystems similar to the tripod schemes) and results in cross-Kerr modulation with group velocity matching of the two fields, leading to enhanced interaction. Single photon implementations of this scheme, however, typically have rather low maximum phase shifts ($\sim 5°$) and has a low QPG fidelity (~ 0.65) [72].

The conditional phase shift (CPS) of one field due to the other would allow, besides a deterministic QPG, the establishment of entanglement between the two input states [1]. As briefly outlined in the next section even a modest CPS can be used with a quantum nondemolition measurement to perform a nearly deterministic QPG.
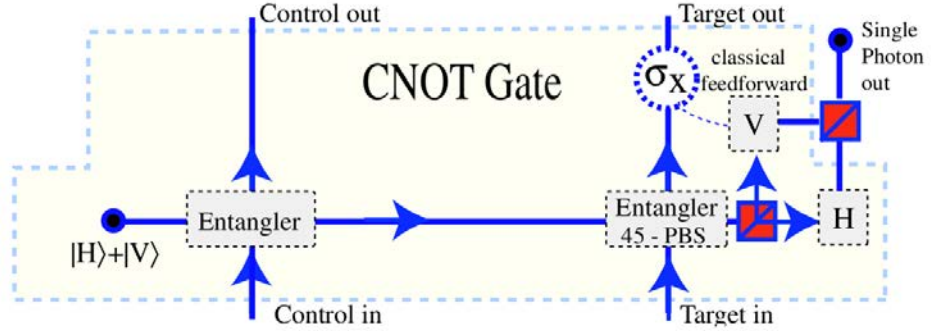
FIGURE 4.6: The nearly deterministic CNOT gate described by Nemoto and Munro [96] that utilises quantum nondemolition measurements and weak cross-Kerr interactions. QND measurements are used to implement the "Entangler" gates shown in the figure and to resolve the state of the second qubit of the target's entangler. Figure taken from Nemoto and Munro [96].

4.3 QPG using weak Kerr nonlinearity

By making use of nondestructive quantum nondemolition (QND) detection it is possible to condition the evolution of the system without destroying the information carried in the photons [97–99]. Nemoto and Munro [96] suggested making use of QND measurements in the implementation of a probabilistic optical CNOT gate, which would drastically improve the probability of success, making the gate nearly deterministic. The QND measurement is performed by making use of a weak cross-Kerr nonlinearity to induce a CPS that is much smaller than π. Specifically Nemoto and Munro adapted the CNOT gate described in Pittman *et al.* [63] by replacing the photon number resolving detectors in the scheme with single photon QND detectors. The scheme for the Nemoto and Munro CNOT gate is presented in Figure 4.6. This scheme makes use of two QND two-qubit entangling gates, one entangles the control qubit with the ancilla and the other entangles the target qubit with the second output qubit of the first entangling gate. The second qubit is then split into dual rail encoding and subjected to a QND photon number resolving measurement. A further requirement for this scheme is the ability to feedforward the results of measurements and to implement single photon operations dependent on the outcomes of the measurements. The target qubit's entangler gate makes use of PBSs in the diagonal basis where as the control qubit's PBSs are in the horizontal-vertical basis.

In order to perform a measurement on a signal system in such a way that the measured state is not demolished by the measuring procedure a measured system is introduced. It is the measured system that is eventually interacted with by the detectors and thus demolished. To gain information about the state of the signal system one first creates an interaction between the two systems, resulting in a final combined system that is a superposition of the signal and measured systems. By creating an entangled
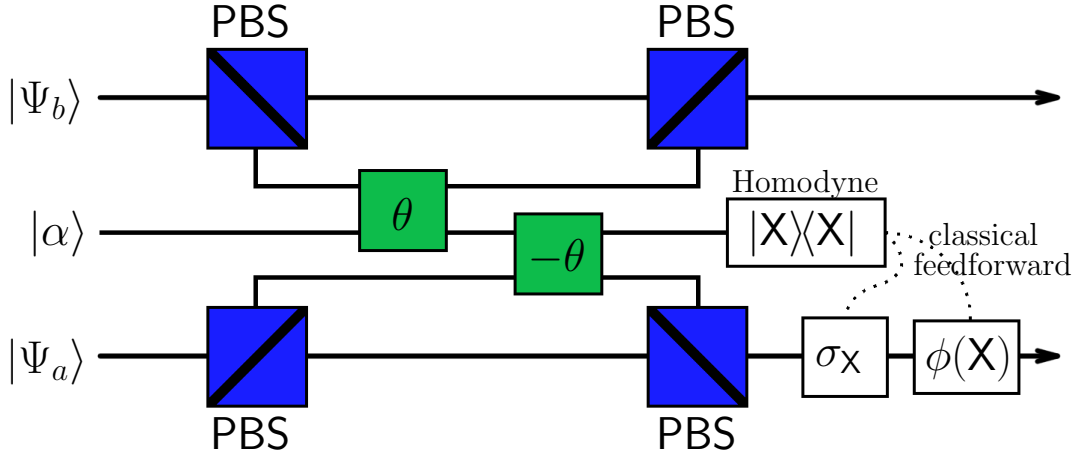
FIGURE 4.7: The QND two-qubit entangling gate described by Nemoto and Munro [96]. The PBSs again decode the polarisation qubits into the dual rail encoding. There are two Kerr media present, one induces a positive phase shift θ and the other exactly the opposite, $-\theta$, phase shift. The results of the homodyne detection $|\mathsf{X}\rangle\langle\mathsf{X}|$ on the coherent state $|\alpha\rangle$ is feedforwarded and used to implement the σ_X gate and a phase shift $\phi(\mathsf{X})$. The output is an entangled state.

state it is then possible to exploit the entanglement (see Einstein, Podolsky, Rosen [100] paradox) to learn the state of the signal system by making a measurement to determine the state of the measured system. The interaction between the two systems to create the entangled state can be achieved with a cross-Kerr interaction [with the Hamiltonian (4.13)] for photonic systems. In particular by making use of a coherent probe field $|\alpha\rangle_p$ (the measured system) interacting via a weak cross-Kerr nonlinearity with a signal field with the general state $|\Psi\rangle_s = c_0 |0\rangle_s + c_1 |1\rangle_s$ the state of the system after the interaction is

$$
\begin{aligned}
|\Psi\rangle &= e^{i\chi\hat{a}_s^\dagger\hat{a}_s\hat{a}_p^\dagger\hat{a}_p t} \left[c_0 |0\rangle_s + c_1 |1\rangle_s \right] |\alpha\rangle_p \\
&= c_0 |0\rangle_s |\alpha\rangle_p + c_1 |1\rangle_s \left|\alpha e^{i\theta}\right\rangle_p ,
\end{aligned}
\tag{4.19}
$$

where the phase shift of the coherent field is given by $\theta = \chi t$ where t is the interaction time. Measurement of the phase of the coherent probe field will then project the signal field into one of the Fock states $|0\rangle_s$ or $|1\rangle_s$. The only requirement is that $\alpha\theta \gg 1$ which even if θ is much smaller than one can be achieved with a strong enough coherent field.

By interacting the coherent measured field with two different signal modes via two cross-Kerr nonlinearities which induce opposite phase shifts Nemoto and Munro [96] introduced a way to produce entangled states. As depicted in Figure 4.7 two polarisation qubits ($|\Psi_a\rangle = c_0 |H\rangle_a + c_1 |V\rangle_a$ and $|\Psi_b\rangle = d_0 |H\rangle_b + d_1 |V\rangle_b$) have their horizontal $|H\rangle$ and vertical $|V\rangle$ components split into different spatial modes by polarising beam

splitters. The mode with the vertical component for each qubit then interacts separately with the coherent field. As a result when looking at the state of the combined system only the components with unmatched polarisations accrue a phase shift:

$$|\Psi\rangle_T = [c_0 d_0 |HH\rangle + c_1 d_1 |VV\rangle] |\alpha\rangle_p + c_0 d_1 |HV\rangle \left|\alpha e^{i\theta}\right\rangle_p + c_1 d_0 |VH\rangle \left|\alpha e^{-i\theta}\right\rangle_p .$$
(4.20)

The last two states can be distinguished due to their opposite phase shifts, but by introducing a phase offset for the local oscillator from the probe phase the states $\left|\alpha e^{\pm i\theta}\right\rangle$ become indistinguishable. It is then possible to distinguish the $|HH\rangle$ and $|VV\rangle$ states from the $|HV\rangle$ and $|VH\rangle$ states. With the application of local rotations dependent on the feedforwarded results of the $|\mathsf{X}\rangle\langle\mathsf{X}|$ homodyne detection the final state of the system can be transformed to

$$|\Psi_X\rangle_T = c_0 d_1 |HV\rangle + c_1 d_0 |VH\rangle$$
(4.21)

thus resulting in a near deterministic outcome, see [96] for complete details. It is this near deterministic entanglement creating gate that causes the dramatic improvement of the CNOT gate over the original KLM CNOT gate.

4.4   Zeno CZ gate

We very briefly discuss the Zeno gate. This two qubit CZ gate that relies on the Zeno effect was first proposed by Franson et al. [101]. This gate makes use of two single photon qubits which are initially in the polarisation basis. Similarly to Figure 4.5, using polarising beam splitters, we convert the system to the dual rail encoding and the modes corresponding to logical $|1\rangle$ enter the CZ gate, Figure 4.8(**a**). The Zeno CZ gate is implemented by a series of n weak beam splitters between the two modes a_2 and b_2. After each beam splitter there is a two-photon absorber in each mode Figure 4.8(**b**). As n tends to infinity and with infinitely short absorbers the continuous coupling limit is approached. The effect of the two-photon absorber is the suppression of the Hong-Ou-Mandel effect via the quantum Zeno effect. The probability of single-photon and two-photon transmission for a single absorber is given by γ_1 and γ_2 respectively. The relative strength between the two probabilities is given by κ: $\gamma_2 = \gamma_1^\kappa$. The Zeno CZ gate performs the following operation [102] on the input states:

$$|00\rangle \to |00\rangle , \ |01\rangle \to \gamma_1^{n/2} |01\rangle , \ |10\rangle \to \gamma_1^{n/2} |10\rangle , \ |11\rangle \to \gamma_1^n \tau |11\rangle + f(|02\rangle , |20\rangle) ,$$
(4.22)

where τ is given by:

$$\tau = \frac{2^{-(3/2)-n}}{d} \left(\left(g + \frac{d}{\sqrt{2}}\right)^n \left(\sqrt{2}d - h\right) + \left(g - \frac{d}{\sqrt{2}}\right)^n \left(\sqrt{2}d + h\right) \right),$$

$$d = \sqrt{\left(1 + \cos\frac{2\pi}{n}\right)(1 + \gamma_2) + 2\sqrt{\gamma_2}\left(\cos\left(\frac{2\pi}{n}\right) - 3\right)},$$

$$g = \left(\cos\frac{\pi}{n}\right)(\sqrt{\gamma_2} + 1), \ \ h = 2\left(\cos\frac{\pi}{n}\right)(\sqrt{\gamma_2} - 1).$$
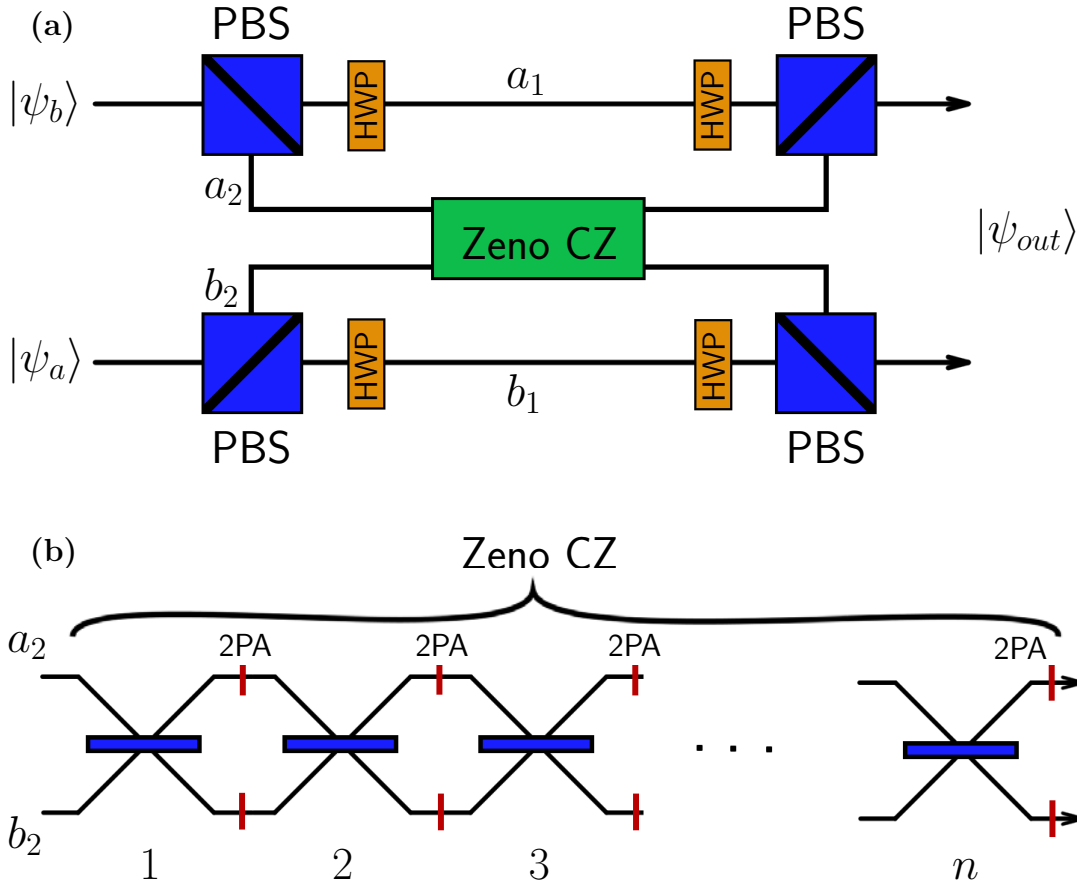(4.23)

FIGURE 4.8: **(a)** Circuit diagram of the Zeno CZ gate with the qubits being converted to the dual rail encoding by PBSs and half wave plates (HWP). **(b)** shows the n beam splitters followed by two-photon absorbers (2PA) that comprise the Zeno CZ gate.

Terms relating to loss has been discarded and as such the output states are not normalised.

It was shown by Leung *et al.* [102] that a Zeno CNOT gate can be implemented within the Gottesman-Chuang teleportation CNOT scheme [103] with a success probability of 0.8 with a two-photon to one-photon absorption ratio $\kappa = 10^4$. These results assume perfect mode-matching which is an unheralded error.

5

NV center Four-level Tripod Quantum Phase Gate

As explained in section 4.2 the conditional phase shift (CPS) can be increased by increasing the interaction time between the light and the Kerr medium, i.e. allowing the fields to pass through a longer section of Kerr medium. The photon-photon coupling can also be enhanced by exploiting the large optical nonlinearities achievable in cavity quantum electrodynamics (QED) where photons trapped in a high quality (high-Q) resonator interact strongly through their mutual coupling to intracavity media [69, 104]. Rather than considering a gas cell of ^{87}Rb atoms to achieve strong coupling we now consider a perhaps more convenient condensed matter system which would be far easier to scale up and could even operate at room temperature. In this chapter we demonstrate the feasibility of a quantum phase gate (QPG) between two weak fields in a cavity-QED system coupled to a single atomic system in a four-level tripod configuration. We demonstrate the possibility to achieve an appreciable CPS. The particular tripod system we consider in this chapter is the diamond based nitrogen-vacancy (NV) center. In order to implement this scheme three crucial elements are required:

1. An atomic system with a four-level tripod transition arrangement.

2. A high-Q cavity (i.e. small cavity field decay rates).

3. The ability to strongly couple the atomic system to the cavity fields.

The four-level tripod configuration scheme can exhibit a large cross-Kerr nonlinearity, in particular Rebić *et al.* (2004) [83] first proposed the system for implementing a conditional phase gate, using ^{87}Rb as an example. Section 5.1 gives the background to the workings of the tripod QPG.

Microresonators have recently gained much attention as high-Q cavities, for example spherical, disk and microtoroidal resonators have high-Q whispering gallery modes (WGM) that can be coupled to evanescently. Recent advances in toroidal and spherical microresonators have seen cavity QED systems with ultra-high quality factors [105, 106] with for example a stable $Q \approx 10^9$ obtained in silica microspheres. These ultra-high quality factors allow for strong coupling between light and atomic systems, thus making a single atom approach feasible. The strong coupling regime is reached when the atom field coupling rate exceeds both the atom decay rate and the cavity decay rate. Furthermore some of these microresonators are chip based which would result in good scalability of the systems. Section 5.2 gives a very brief overview of microresonators.

Which brings us to the third requirement, the ability to couple the tripod system to the high-Q modes in a resonator. Nitrogen-vacancy (NV) centres can be configured in a tripod level scheme, and single NV centres can be found in diamond nanocrystals $\sim 10\,\text{nm}$ in size. Experiments coupling nanodiamonds containing NV centres and solid state cavity QED systems have recently been performed with silica microspheres [107] and microdisks [108]. Section 5.3 expands on NV nanodiamonds and their coupling via the evanescent fields to the cavity modes in microresonator systems.

Section 5.4 brings these elements together and describe the workings of a system comprised of a *single* nitrogen-vacancy center coupled to two cavity modes. We demonstrate the remarkable possibility of obtaining a conditional phase shift in excess of π by exploiting the cross-Kerr nonlinearity in a four-level tripod system in a high-Q cavity. Such a large CPS would allow the execution of a two-qubit CZ gate and by extension a CNOT gate, which together with single qubit gates completes the universal set of gates required for optical quantum computing. Our simulations in Matlab, making use of the Quantum Optics Toolbox [109], include dephasing and decay in the NV center with values taken from recent experimental literature.

5.1   QPG in the four-level atomic system in tripod configuration

In this section we look in closer detail at the four-level tripod configuration and the conditional phase shift induced by the large cross-Kerr nonlinearity inherent in the system. This section also serves as background for the section on the QPG proposed for the NV centre in a cavity in section 5.4. The four-level tripod configuration has been used previously to achieve stimulated Raman adiabatic passage (STIRAP) between two states by Unanyan *et al.* [110], but it was first investigated as a system for implementing a quantum phase gate by Rebić *et al.* [83]. The latter work envisioned the Kerr media to be a cold atomic gas. The enhanced cross-phase modulation in the tripod system has recently been experimentally demonstrated in ^{87}Rb atomic vapour by Li *et al.* [93]. One of the essential features of this scheme is the ability to greatly reduce the group velocities of the two interacting fields by creating double EIT in two Λ subsystems: one for the probe and one for the trigger field. The two Λ subsystems facilitating the EIT share a classical driving field coupling one of the three ground states to the excited state. Furthermore, by choosing the parameters of the system carefully one can match
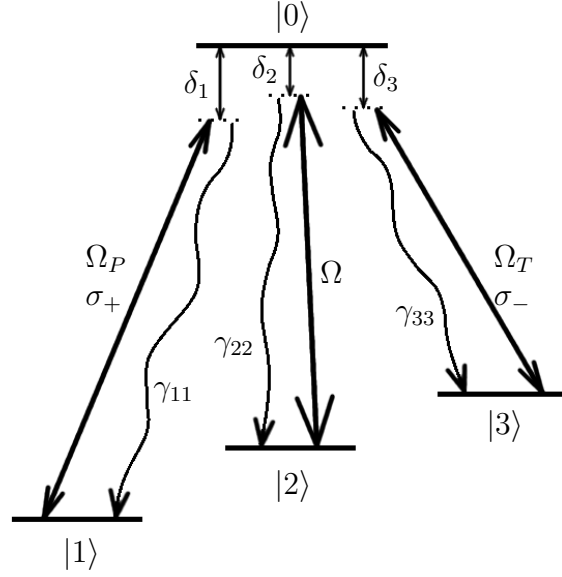
FIGURE 5.1: The four-level tripod system. The probe (Ω_P) and trigger (Ω_T) fields undergo cross-phase modulation and have different polarisations $\sigma_\pm$. Ω is a classical driving field. The fields have respective detunings δ_1, δ_3 and δ_2. The excited state has a total decay rate of $\gamma_{11} + \gamma_{22} + \gamma_{33}$.

the group velocities of the probe and trigger fields, greatly increasing the interaction between the two fields. In order to obtain the required nonlinearities it is also essential that the fields are slightly detuned from the exact two-photon resonance conditions of EIT, that is $\delta_1 \neq \delta_2$ and $\delta_2 \neq \delta_3$, but still remain within the respective transparency windows.

In the four-level tripod scheme (Figure 5.1) for a QPG as proposed by Rebić *et al.* [83], the two interacting qubits are encoded in the polarisation of the probe and trigger fields. The probe field has a Rabi frequency Ω_P and drives the transition between the first ground state $|1\rangle$ and the excited state $|0\rangle$. Similarly the trigger field has a Rabi frequency Ω_T and drives the $|3\rangle \rightarrow |0\rangle$ transition. The second ground state $|2\rangle$ is driven by the classical control field with Rabi frequency Ω. The probe, control and trigger field detunings are δ_1, δ_2, δ_3 respectively with $\delta_1 \neq \delta_2$ and $\delta_2 \neq \delta_3$. The rates of excited state spontaneous emission into the ground states are denoted by γ_{11}, γ_{22} and γ_{33}. The Hamiltonian for the system in the interaction picture and after the traditional rotating wave approximation is:

$$
\begin{aligned}
H =& \hbar\delta_1\hat{\sigma}_{00} + \hbar\left(\delta_1 - \delta_2\right)\hat{\sigma}_{22} + \hbar\left(\delta_1 - \delta_3\right)\hat{\sigma}_{33} \\
& + \hbar\Omega_P\left(\hat{a}^\dagger\hat{\sigma}_{10} + \hat{a}\hat{\sigma}_{01}\right) + \hbar\Omega\left(\hat{\sigma}_{20} + \hat{\sigma}_{02}\right) \\
& + \hbar\Omega_T\left(\hat{b}^\dagger\hat{\sigma}_{30} + \hat{b}\hat{\sigma}_{03}\right),
\end{aligned}
\tag{5.1}
$$

where the Rabi frequencies have been assumed to be real and $\hat{\sigma}_{ij} = |i\rangle\langle j|$ are the atomic operators.

The Bloch equations for the density matrix elements ($\rho_{ij} = \mathrm{Tr}\{\hat{\sigma}_{ij}\rho\} = \langle i|\rho|j\rangle$) for

the populations are

$$i\dot{\rho}_{00} = -i\left(\gamma_{11} + \gamma_{22} + \gamma_{33}\right)\rho_{00} + \Omega_P^*\rho_{10} - \Omega_P\rho_{01}$$
$$+ \Omega^*\rho_{20} - \Omega\rho_{02} + \Omega_T^*\rho_{30} - \Omega_T\rho_{03}, \tag{5.2}$$

$$i\dot{\rho}_{11} = i\left(\gamma_{11}\rho_{00} + \gamma_{12}\rho_{22} + \gamma_{13}\rho_{33}\right) + \Omega_P\rho_{01} - \Omega_P^*\rho_{10}, \tag{5.3}$$

$$i\dot{\rho}_{22} = i\left(\gamma_{22}\rho_{00} - \gamma_{12}\rho_{22} + \gamma_{23}\rho_{33}\right) + \Omega\rho_{02} - \Omega^*\rho_{20}, \tag{5.4}$$

$$i\dot{\rho}_{33} = i\gamma_{33}\rho_{00} - i\left(\gamma_{13} + \gamma_{23}\right)\rho_{33} + \Omega_T\rho_{03} - \Omega_T^*\rho_{30}, \tag{5.5}$$

and for the coherences are

$$i\dot{\rho}_{10} = -\Delta_{10}\rho_{10} + \Omega_P\left(\rho_{00} - \rho_{11}\right) - \Omega\rho_{12} - \Omega_T\rho_{13}, \tag{5.6}$$

$$i\dot{\rho}_{20} = -\Delta_{20}\rho_{20} + \Omega\left(\rho_{00} - \rho_{22}\right) - \Omega_P\rho_{21} - \Omega_T\rho_{23}, \tag{5.7}$$

$$i\dot{\rho}_{30} = -\Delta_{30}\rho_{30} + \Omega_T\rho00 - \Omega_P\left(\rho_{33} + \rho_{31}\right) - \Omega\rho_{32}, \tag{5.8}$$

$$i\dot{\rho}_{12} = -\Delta_{12}\rho_{12} + \Omega_P\rho_{02} - \Omega^*\rho_{10}, \tag{5.9}$$

$$i\dot{\rho}_{13} = -\Delta_{13}\rho_{13} + \Omega_p\rho_{03} - \Omega_T^*\rho_{10}, \tag{5.10}$$

$$i\dot{\rho}_{23} = -\Delta_{23}\rho_{23} + \Omega\rho_{03} - \Omega_T^*\rho_{20}, \tag{5.11}$$

where collisional dephasing is described by γ_{jk} $(j \neq k)$ in particular γ_{j0} denotes the decay of atomic coherences. Furthermore the complex effective detunings are defined in terms of these dephasing rates as

$$\Delta_{j0} = \delta_j + i\gamma_{j0} \tag{5.12}$$

$$\Delta_{jk} = \delta_j - \delta_k + i\gamma_{jk} \quad (j, k = 1, 2, 3). \tag{5.13}$$

In order to maintain the symmetry between the interaction of the probe field and the trigger field with the system it is required that the steady-state populations between state $|1\rangle$ and $|3\rangle$ are symmetric. That is, $\rho_{11} \approx 1/2$ and $\rho_{33} \approx 1/2$, which is achieved when $\Omega_P \approx \Omega_T$ and $|\Omega|^2 \gg |\Omega_{P,T}|^2$. With these assumptions the Bloch equations for the populations can be decoupled from those for the coherences and the steady-state solution for the coherences can be obtained, see Equations (6a) and (6b) in reference [83]. The coherences can then be used to find the probe and trigger field susceptibilities

$$\chi_P = -\lim_{t\to\infty} \frac{\mathcal{N}|\boldsymbol{\mu}_P|^2}{\hbar\epsilon_0}\frac{\rho_{10}(t)}{\Omega_P}, \tag{5.14}$$

$$\chi_T = -\lim_{t\to\infty} \frac{\mathcal{N}|\boldsymbol{\mu}_T|^2}{\hbar\epsilon_0}\frac{\rho_{30}(t)}{\Omega_T}, \tag{5.15}$$

where $\boldsymbol{\mu}_{P,T}$ are the electric dipole matrix elements and $\mathcal{N}$ is the atomic density. Retaining only the two lowest order terms for the susceptibilities we are left with a linear component and a third order nonlinear component:

$$\chi_P = \chi_P^{(1)} + \chi_P^{(3)}|E_T|^2, \tag{5.16}$$

$$\chi_T = \chi_T^{(1)} + \chi_T^{(3)}|E_P|^2. \tag{5.17}$$

The linear susceptibilities are

$$\chi_P^{(1)} = \frac{\mathcal{N}|\boldsymbol{\mu}_P|^2}{\hbar\epsilon_0} \frac{1}{2} \frac{\Delta_{12}}{\Delta_{10}\Delta_{12} - |\Omega|^2}, \tag{5.18}$$

$$\chi_T^{(1)} = \frac{\mathcal{N}|\boldsymbol{\mu}_T|^2}{\hbar\epsilon_0} \frac{1}{2} \frac{\Delta_{23}^*}{\Delta_{30}\Delta_{23}^* - |\Omega|^2}, \tag{5.19}$$

the factor $1/2$ is due to the steady-state populations of the ground states. It is the $\chi^{(3)}$ cross-Kerr nonlinear terms that are of greatest interest here, inducing the cross-phase modulation that is required to observe a conditional phase shift. The $\chi^{(3)}$ susceptibility for the probe field is given by

$$\chi_P^{(3)} = \mathcal{N} \frac{|\boldsymbol{\mu}_P|^2 |\boldsymbol{\mu}_T|^2}{\hbar^3 \epsilon_0} \times \frac{1}{2} \frac{\Delta_{12}/\Delta_{13}}{\Delta_{10}\Delta_{12} - |\Omega|^2}$$
$$\times \left(\frac{\Delta_{12}}{\Delta_{10}\Delta_{12} - |\Omega|^2} + \frac{\Delta_{23}}{\Delta_{30}^*\Delta_{23} - |\Omega|^2} \right) \tag{5.20}$$

while the cross-Kerr susceptibility for the trigger field is

$$\chi_T^{(3)} = \mathcal{N} \frac{|\boldsymbol{\mu}_T|^2 |\boldsymbol{\mu}_P|^2}{\hbar^3 \epsilon_0} \times \frac{1}{2} \frac{\Delta_{23}^*/\Delta_{13}^*}{\Delta_{30}\Delta_{23}^* - |\Omega|^2}$$
$$\times \left(\frac{\Delta_{12}^*}{\Delta_{10}^*\Delta_{12}^* - |\Omega|^2} + \frac{\Delta_{23}^*}{\Delta_{30}\Delta_{23}^* - |\Omega|^2} \right) \tag{5.21}$$

The system can be envisioned as two Λ systems: the first comprised of states $|1\rangle \rightarrow |0\rangle \rightarrow |2\rangle$ and the probe field; the second comprised of states $|3\rangle \rightarrow |0\rangle \rightarrow |2\rangle$ and the trigger field, the systems share the control field. These two Λ systems result in EIT for the probe and the trigger field, and as such a reduction in group velocity for both of the two fields. Perfect EIT occurs when the two fields in the Λ system is in perfect two-photon resonance (see section 2.2). This implies that perfect EIT for both the probe and trigger fields will occur when the detunings are all equal, i.e. $\delta_1 = \delta_2 = \delta_3$. This condition would however result in the real part of the cross-Kerr susceptibilities [equations (5.20) and (5.21)] becoming zero and hence the system would no longer be nonlinear and there would be no cross-phase modulation. It is thus necessary to disturb the exact EIT condition by having slightly different detunings for the fields but still keep the fields within the EIT transparency windows. The group velocity of the fields are determined by $v_g = c/(1 + n_g)$, where the group index is given by

$$(n_g)_{P,T} = \frac{1}{2}\text{Re}[\chi] + \frac{\omega_{P,T}}{2} \left(\frac{\delta\text{Re}[\chi]}{\delta\omega} \right)_{\omega_{P,T}}, \tag{5.22}$$

and c is the speed of light in a vacuum. $\omega_{P,T}$ is the laser frequency of the probe or trigger fields. To very close approximation the group index is only determined by the linear part of the susceptibility [Equation (5.18)], and as such neglecting the nonlinear

contributions and assuming equal detunings we can deduce an approximation for the group velocity of the probe field

$$(v_g)_P \approx \frac{4\hbar c \epsilon_0}{\omega_P \mathcal{N} |\boldsymbol{\mu}_P|^2} \left(|\Omega|^2 + |\Omega_T|^2\right), \qquad (5.23)$$

and the trigger field

$$(v_g)_T \approx \frac{4\hbar c \epsilon_0}{\omega_T \mathcal{N} |\boldsymbol{\mu}_T|^2} \left(|\Omega|^2 + |\Omega_P|^2\right) \qquad (5.24)$$

when they are both tuned exactly in the middle of their respective transparency windows (ie. exact two-photon resonance).

Rebić *et al.* (2004) specifically discuss the possible implementation of this scheme in ^{87}Rb atoms. The ground states of the tripod system, states $|1\rangle$, $|2\rangle$ and $|3\rangle$ would correspond respectively to the ground state Zeeman sublevels $\left|5S_{1/2}, F = 1, m = -1\right\rangle$, $\left|5S_{1/2}, F = 1, m = 0\right\rangle$ and $\left|5S_{1/2}, F = 1, m = 1\right\rangle$, while the excited state $|0\rangle$ corresponds to $\left|5P_{3/2}, F = 0\right\rangle$ of the ^{87}Rb system. This system will appear transparent to a probe field ($|1\rangle \rightarrow |0\rangle$) with σ^- polarisation and to a trigger field ($|3\rangle \rightarrow |0\rangle$) with σ^+ polarisation. There will thus only be a cross-phase modulation between the two fields when the probe field has σ^+ polarisation and the trigger field has σ^- polarisation. A qubit can then be encoded in the polarisation of the fields: for the probe field σ^- corresponds to logical $|0\rangle$ and σ^+ corresponds to logical $|1\rangle$; for the trigger field σ^+ corresponds to logical $|0\rangle$ and σ^- corresponds to logical $|1\rangle$. This provides everything necessary for a QPG which would have the following truth table:

$$\begin{aligned}
\left|\sigma^-\right\rangle_P \left|\sigma^-\right\rangle_T &\rightarrow e^{-i(\phi_0^P + \phi_{lin}^T)} \left|\sigma^-\right\rangle_P \left|\sigma^-\right\rangle_T, \\
\left|\sigma^-\right\rangle_P \left|\sigma^+\right\rangle_T &\rightarrow e^{-i(\phi_0^P + \phi_0^T)} \left|\sigma^-\right\rangle_P \left|\sigma^+\right\rangle_T, \\
\left|\sigma^+\right\rangle_P \left|\sigma^+\right\rangle_T &\rightarrow e^{-i(\phi_{lin}^P + \phi_0^T)} \left|\sigma^+\right\rangle_P \left|\sigma^+\right\rangle_T, \\
\left|\sigma^+\right\rangle_P \left|\sigma^-\right\rangle_T &\rightarrow e^{-i(\phi_{XPM}^P + \phi_{XPM}^T)} \left|\sigma^+\right\rangle_P \left|\sigma^-\right\rangle_T,
\end{aligned} \qquad (5.25)$$

Where ϕ_0 is the vacuum phase shift acquired by the fields when there is no interaction with the atomic system and the linear phase shift is given by ϕ_{lin}. The phase shift that the fields acquire during cross-phase modulation is the sum of the phase shift due to linear interactions and the phase shift due to the nonlinear cross-Kerr interactions: $\phi_{XPM} = \phi_{lin} + \phi_{nlin}$. The conditional phase shift consists of only the nonlinear contributions to the phase shift of the logical $|1\rangle$ states, and is calculated from the above phase shifts by

$$\phi = \phi_{XPM}^P + \phi_{XPM}^T - \phi_{lin}^P - \phi_{lin}^T, \qquad (5.26)$$

in a similar fashion as done in Equation (4.18). Simulations of the system reveal that a π conditional phase shift could be obtained in an atomic sample with an interaction length of 1.6 mm and a density $\mathcal{N} = 3 \times 10^{13}$ cm^{-3} [83].

The enhanced cross-Kerr nonlinearity based on double EIT in a four-level tripod level configuration was recently experimentally demonstrated in ^{87}Rb [93, 94]. The experiment did not make use of the atomic levels suggested above, but did reach a CPS $\sim 5°$.

5.2   Microresonators

In this section we present a very brief overview of microresonators (microcavities) which are solid state optical cavities. Included in the category of microresonators we find microdisks, which are either supported by a central column, or rests flat on a substrate, microtoroids that are also supported by a central column, and micro spheres that are manufactured from the tips of optical fibres and remain attached to it. See theses by Spillane [111] (microtoroids), Kippenberg [112] (micro-toroids, -spheres, -disks) and Mazzei [113] (microspheres) for far more detail on microresonators and their manufacturing processes. In particular we are interested in microresonators with extremely low optical losses and very small mode volumes.

Microresonators work on the principle of total internal reflection of the relevant modes. This results in whispering gallery modes (WGMs) in the resonator that can couple evanescently to atoms near the surface of the microresonator. Various factors contribute to the radiative losses from the WGMs, for example material absorption and scattering from impurities and imperfections. The losses from the cavity are described by the quality factor which is defined by

$$Q \equiv \omega \frac{E_{stored}}{P_{diss}} = \omega\tau, \tag{5.27}$$

where ω is the resonance frequency $\omega = 2\pi c/\lambda$ with the resonance wavelength λ, E_{stored} is the energy stored in the resonant system, and P_{diss} is the dissipation power. The photon lifetime in the cavity is given by τ.

The losses from the WGM are determined by several factors that describe the radiative losses from the microresonator, the intrinsic loss over which one has little control past the manufacturing stage is:

$$Q_{int}^{-1} = Q_{rad}^{-1} + Q_{scat}^{-1} + Q_{cont}^{-1} + Q_{mat}^{-1}, \tag{5.28}$$

where Q_{rad}^{-1} is the radiative losses due to the curvature; Q_{scat}^{-1} is the scattering losses from inhomogeneities in the surface; Q_{cont}^{-1} is the losses due to contaminants both on the surface and within the microresonator material and Q_{mat}^{-1} is the material losses due to absorption. The intrinsic loss together with the loss due to coupling of the WGM to external devices (Q_{coup}^{-1}), for example an input/output fibre, gives the total Q factor:

$$Q_{total}^{-1} = Q_{int}^{-1} + Q_{coup}^{-1}. \tag{5.29}$$

Clearly in order to execute high fidelity quantum operations one will need microresonator cavities with extremely low intrinsic losses and as such high Q values for each of the intrinsic loss mechanisms.

Not surprisingly the quality factor of a mode in an optical cavity relates directly to the decay rate of that mode. The cavity mode decay rate is given by

$$\kappa \equiv \frac{\pi c}{\lambda Q} \equiv \frac{\omega}{2Q}. \tag{5.30}$$

Another important parameter of microresonators is the mode volume. It is the volume occupied by the mode, and includes both the part of the field confined within the cavity and the evanescent part of the field just outside the cavity wall. There are several different definitions of mode volume depending on the specific aspect of the microresonator that is being investigated. The mode volumes for transverse electrical (TE) and transverse magnetic (TM) polarised modes are different. The mode volume also depends on the geometry of the microresonator and as such, for example a microtoroid and microsphere cavity will yield different mode volumes for the same resonance frequency. Here we are interested in the enhanced coupling to atomic systems that a large electric field per photon implies [104]. As such we are interested in small mode volumes. On the other hand the better the field is confined in the resonator the weaker the evanescent field outside the resonator that the atomic system will couple to. It is thus critical to have the atomic system we wish to couple to the WGM as close as possible to the surface of the resonator at a location where the evanescent field is at its maximum.

High quality factor (high-Q) microresonators have been demonstrated in a variety of guises in solid state systems. Examples of high-Q microresonators are: microspheres made of silica (SiO_2) with up to $Q \sim 10^9$ [106, 113]; microdisks made from SiN_x and GaAs $Q \sim 10^6$ [114, 115]; microtoroids monolithically grown from SiO_2 on silicon chips $Q \sim 10^8$ [105, 116]. The ultra high-Q factors demonstrated in microspheres and microtoroids are especially interesting.

5.3 NV centres coupled to microresonators

What remains now is the ability to strongly couple a system in tripod level configuration to a high-Q microcavity. As we saw in section 2.3 the nitrogen vacancy centre in diamond possesses a spin triplet ground state ^3A that is split by 2.88 GHz into a doublet ($m_s = \pm 1$) and singlet spin sublevel ($m_s = 0$). With the application of a magnetic field the doublet will be split into two singlets, thus providing the three ground states required for a four-level tripod system.

NV centres have been coupled to a wide variety of microresonators and we describe a few of the most noteworthy and relevant experiments to date. NV centres in bulk diamond have recently been coupled to a GaP microdisk resonator by Barclay *et al.* [117]. GaP microdisks were manufactured and deposited on bulk diamond samples containing NV centres. This experiment coupled many NV centres to the microresonator which had a total Q factor $Q > 2.5 \times 10^4$. Due to inhomogeneities between different NV centres (due to different strain environments and dipole orientation) it would be ideal to have only a *single* NV centre couple to the cavity. Single NV centres have previously been observed in nanodiamonds sized from a few tens of nanometre [118] down to $\sim 5\,\mathrm{nm}$ [119]. Let us consider the deposition of a nanodiamond onto the surface of a microresonator. For very small nanocrystals, the single NV centre contained within the nanocrystal will be in close proximity to the microresonator surface, and thus be exposed to a stronger evanescent field than if it were situated further from the surface.

This strategy was followed by Barclay *et al.* [108] when they coupled nanocrystals

with a median diameter of 200 nm to a high-Q SiO_2 microdisk cavity ($Q \approx 10^5$). The
nanocrystal was positioned on the surface with 100 nm accuracy, but better accuracy
manipulation of nanodiamonds have been demonstrated down to a few nanometres
[120]. The nanodiamonds in [120], however, did not contain single NV centres but
on average contained 5 NV centres. From the modelling done by Barclay *et al.* [108]
of the coupling between a particular WGM (with maximum evanescent field at the
nanocrystal location) and the NV centre (with optimal dipole orientation of the NV)
it was estimated that the coupling rate *at the surface* of the microresonator would be
$g_{total}/2\pi \approx 640\,\text{MHz}$ and the coupling rate to the zero phonon line would be $g_{zpl}/2\pi \approx$
$130\,\text{MHz}$. These are the maximum coupling rates achievable. The coupling rate realised
in the experiment to the zero phonon line, however, was only $g_{zpl}/2\pi \approx 28\,\text{MHz}$. Factors
contributing to the decreased coupling rate are: imperfect dipole orientation within the
nanocrystal; imperfect mode-matching; local field effects in the diamond; and distance
of the NV centres from the optimum position.

Park *et al.* [107] deposited many nanodiamonds with an average size of 75 nm on
the surface of silica microspheres and demonstrated coupling between NV centres and
WGMs of the microsphere. The WGMs had Q factors in the range $Q \approx 10^8$ and the
experiment yielded a coupling rate for the zero phonon line of $g_{zpl}/2\pi \approx 55\,\text{MHz}$ for
the cavity QED system. Another approach taken by Larsson *et al.* [121] is to couple
NV centres in diamond nanopillars to the high-Q WGMs in silica microspheres. The
nanopillars, etched from bulk diamond, contained many NV centres and had a diameter
of 200 nm. The Q factor for the composite cavity-pillar system was $Q \approx 2 \times 10^6$. The
first to couple single NV centres to high-Q WGMs in microspheres was Schietinger
et al. [122, 123]. They made use of polystyrene microspheres that were preselected
to match the NV frequency. A nanodiamond with only a *single* NV centre contained
within it was identified and selected from a collection with an average nanodiamond
diameter of 25 nm, and then attached to the microsphere. Subsequently coupling of
the NV to a WGM with $Q \approx 5500$ was observed.

We make use of observations from some of these experiments to provide numerical
values for some of the parameters used in section 5.4 for the modelling of the QPG.

5.4 Nonlinear interaction with a strongly coupled single tripod system and cavity modes

The results presented here make no assumption on the specific type of cavity used. A
cavity with a sufficiently high quality factor such that there is strong coupling between
the cavity fields and the NV center is however assumed and this restricts the type of
suitable cavity. Being able to implement this scheme in a condensed matter system
would be greatly beneficial for the scalability and integration of the CPHASE gate
with other optical elements, as such the semiconductor grown micro-resonators with
their high quality factors are ideal systems to implement this scheme in. In particular
whispering gallery modes in spherical and toroidal micro-resonators have been shown
to have ultra-high Q factors up to 10^9 [105, 106]. Ultra-high Q factors allow for
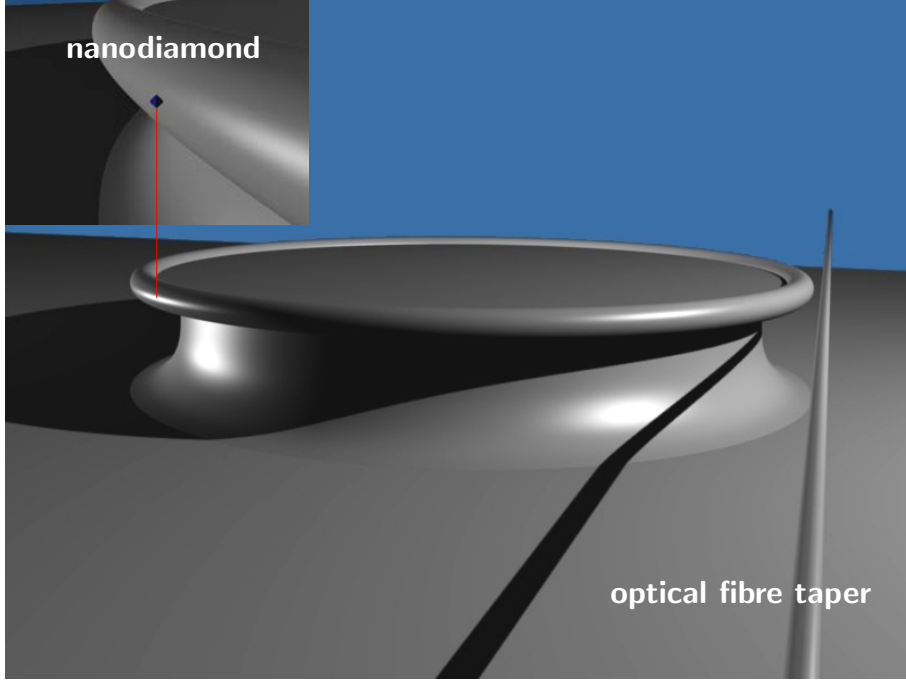strong coupling between light and atomic systems, thus making a single atom approach

FIGURE 5.2: Nanodiamond on the surface of a microtoroidal resonator with an optical fibre taper for input and output coupling.

feasible.

In particular we consider a nitrogen vacancy center in diamond as our four-level tripod system, and use characteristic values for the NV center from the literature. A schematic of how this system might appear in practice is depicted in Figure 5.2. The nitrogen vacancy center is explained in section 2.3, but for completeness the required essentials are given here too. A substitutional nitrogen atom accompanied by a vacancy forms the NV center in diamond. The NV center has a strong optical transition between the spin triplet states ^{3}A and ^{3}E with a zero-phonon line at 637 nm. The four-level tripod system is depicted in Figure 5.3, the three ground states are: $|1\rangle$ the $m_s = +1$ spin sublevel, $|2\rangle$ the $m_s = 0$ spin sublevel, and $|3\rangle$ the $m_s = -1$ spin sublevel, the excited state is denoted as $|0\rangle$. States $|1\rangle$ and $|0\rangle$ are connected by a weak probe field (a) with a coupling strength g_P, whilst the weak trigger field (b) with a coupling strength g_T connects states $|3\rangle$ and $|0\rangle$. The $|2\rangle \rightarrow |0\rangle$ transition is driven by a classical field with a Rabi frequency Ω. The transitions have detunings δ_1, δ_2 and δ_3. In our calculations we have included decay (γ_{ii}) from the excited state to ground state $|i\rangle$, we also included ground state dephasing (γ_{ph}) which is assumed to be equal for all the ground states. The decay rates sum to the total decay rate of the excited state, $\gamma = \gamma_{11} + \gamma_{22} + \gamma_{33}$. The values for the various parameters used in the simulation were
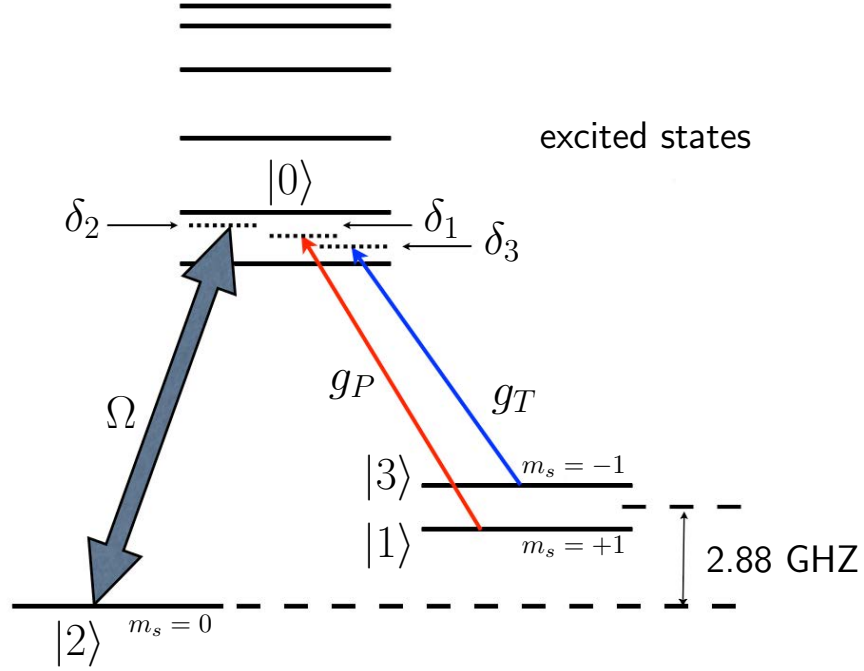
FIGURE 5.3: The NV tripod system. The probe and trigger fields have coupling strengths g_P and g_T respectively. Ω is a classical driving field. The fields have respective detunings δ_1, δ_3 and δ_2. This figure is similar to Figure 5.1 except that the probe and trigger couplings are much weaker and are thus given as coupling strengths instead of as Rabi frequencies.

taken from literature and is presented in table 5.1.

The Hamiltonian in the interaction picture and after the rotating wave approximation of the four-level system is similar to Equation (5.1) except that the Rabi frequencies Ω_P and Ω_T are replaced with the coupling strengths g_P and g_T for the probe and trigger fields respectively and the electro-magnetic fields are quantised. The Hamiltonian is given by:

$$
\begin{aligned}
H_{sys} =& \hbar\delta_1\hat{\sigma}_{00} + \hbar\left(\delta_1 - \delta_2\right)\hat{\sigma}_{22} + \hbar\left(\delta_1 - \delta_3\right)\hat{\sigma}_{33} \\
& + \hbar g_P\left(\hat{a}^\dagger\hat{\sigma}_{10} + \hat{a}\hat{\sigma}_{01}\right) + \hbar\Omega\left(\hat{\sigma}_{20} + \hat{\sigma}_{02}\right) \\
& + \hbar g_T\left(\hat{b}^\dagger\hat{\sigma}_{30} + \hat{b}\hat{\sigma}_{03}\right).
\end{aligned}
\tag{5.31}
$$

Where $\hat{\sigma}_{ij} = |i\rangle\langle j|$ $(i, j = 0, 1, 2, 3)$ are the atomic coherences, and $\hat{a}$ and $\hat{b}$ are the probe and trigger field annihilation operators respectively.

We introduce the time evolution of the system through the master equation in the Lindblad form:

$$
\dot{\rho} = -\frac{i}{\hbar}\left[H_{sys}, \rho\right] + \left(\mathcal{L}_{cav} + \mathcal{L}_{spon} + \mathcal{L}_{ph}\right)\rho,
\tag{5.32}
$$

Parameter	Value	Source
γ (excited state decay rate)	$13.4(2\pi) \times 10^6\,\mathrm{Hz}$	Santori *et al.* [28]
γ_{22} (decay to state) $|2\rangle$	$0.8 \times 13.4(2\pi) \times 10^6\,\mathrm{Hz}$	Santori *et al.* [28]
γ_{11} (decay to state) $|1\rangle$	$0.1 \times 13.4(2\pi) \times 10^6\,\mathrm{Hz}$	Santori *et al.* [28]
γ_{33} (decay to state) $|3\rangle$	$0.1 \times 13.4(2\pi) \times 10^6\,\mathrm{Hz}$	Santori *et al.* [28]
γ_{ph} (ground state dephasing)	$1.2(2\pi) \times 10^6\,\mathrm{Hz}$	Santori *et al.* [28]
g_P and g_T (field coupling strength)	$640(2\pi) \times 10^6\,\mathrm{Hz}$	Barclay *et al.* [108]

TABLE 5.1: The values for parameters used in the simulation are presented in this table. Where applicable numeric values were taken from the literature.

where the decoherence terms are

$$\mathcal{L}_{cav}\rho = \kappa_P \left(2\hat{a}\rho\hat{a}^\dagger - \hat{a}^\dagger\hat{a}\rho - \rho\hat{a}^\dagger\hat{a}\right) + \kappa_T \left(2\hat{b}\rho\hat{b}^\dagger - \hat{b}^\dagger\hat{b}\rho - \rho\hat{b}^\dagger\hat{b}\right)$$

$$\mathcal{L}_{spon}\rho = \frac{\gamma_{11}}{2}\left(2\hat{\sigma}_{10}\rho\hat{\sigma}_{01} - \hat{\sigma}_{00}\rho - \rho\hat{\sigma}_{00}\right) + \frac{\gamma_{22}}{2}\left(2\hat{\sigma}_{20}\rho\hat{\sigma}_{02} - \hat{\sigma}_{00}\rho - \rho\hat{\sigma}_{00}\right)$$

$$+ \frac{\gamma_{33}}{2}\left(2\hat{\sigma}_{30}\rho\hat{\sigma}_{03} - \hat{\sigma}_{00}\rho - \rho\hat{\sigma}_{00}\right)$$

$$\mathcal{L}_{ph}\rho = \frac{\gamma_{ph}}{2}\left(2\hat{\sigma}_{11}\rho\hat{\sigma}_{11} - \rho\hat{\sigma}_{11} - \hat{\sigma}_{11}\rho\right) + \frac{\gamma_{ph}}{2}\left(2\hat{\sigma}_{22}\rho\hat{\sigma}_{22} - \rho\hat{\sigma}_{22} - \hat{\sigma}_{22}\rho\right)$$

$$+ \frac{\gamma_{ph}}{2}\left(2\hat{\sigma}_{33}\rho\hat{\sigma}_{33} - \rho\hat{\sigma}_{33} - \hat{\sigma}_{33}\rho\right). \tag{5.33}$$

For simplicity we take the cavity decay rates for the probe and trigger fields as being equal, $\kappa_P = \kappa_T = \kappa$. The cavity decay rate κ is determined by: the intrinsic cavity decay rate κ_C a function of the Q-factor of the cavity and the frequency of the light [see Equation (5.30)]; and the decay rate due to out coupling to for example an input/output fibre κ_F. The magnitude of the cavity out-coupling decay rate, κ_F can be made arbitrarily close to zero by increasing the distance the input/output fibre is from the cavity. With the NV centre ZPL at 637 nm and assuming an ultra high-Q cavity with $Q = 10^9$ we calculate the intrinsic cavity decay rate

$$\kappa_C = \frac{\pi c}{\lambda Q}$$

$$= 1.4796\,\mathrm{MHz}. \tag{5.34}$$

The probe and trigger fields are taken as weak fields and as such we are considering single photon fields. In order to calculate the conditional phase shift from the density operator of the system we need to use a superposition of zero and one photon per field:

$$|\psi(0)\rangle_{P,T} = c_{00}\,|0_P 0_T\rangle + c_{01}\,|0_P 1_T\rangle + c_{10}\,|1_P 0_T\rangle + c_{11}\,|1_P 1_T\rangle. \tag{5.35}$$

In addition, similar to previous work with the tripod system [83, 124], the initial population of the atomic system is taken to be even between state $|1\rangle$ and $|3\rangle$ and as such the initial state of the system is given by:

$$\rho(0) = \left(\frac{1}{2}\,|1\rangle\langle 1| + \frac{1}{2}\,|3\rangle\langle 3|\right) \otimes \left(|\psi(0)\rangle_{P,T}\langle\psi(0)|\right). \tag{5.36}$$

We obtain the time evolution of the density operator by solving the master equation (5.32) using specific values for the free parameters $(\Omega, \delta_1, \delta_2, \delta_3)$ and taking the coefficients c_{ij} in the initial state (5.35) all equal. The detunings are chosen such that slightly disturbed double EIT conditions in the two Λ subsystems are created. By tracing over the NV centre degrees of freedom we obtain the reduced density operator $\rho_{P,T}(t) = \text{Tr}_{NV}[\rho(t)]$ for the probe and trigger fields. The CPS ϕ is then calculated from the relevant off-diagonal elements of the reduced density operator according to

$$\phi = \phi_{11} + \phi_{00} - \phi_{01} - \phi_{10}, \tag{5.37}$$

where the ϕ_{ij} are the phase shifts accrued by each of the states in two-qubit superposition as they interact with the NV centre.

Besides a large CPS we also need to be sure that the gate implemented has a high fidelity. We calculate the fidelity in the same way as was done in References [89, 90] by constructing an ideally evolved state for the fields:

$$|\psi_{id}(t)\rangle = c_{00}e^{i\phi_{00}}|0_P 0_T\rangle + c_{01}e^{i\phi_{01}}|0_P 1_T\rangle + c_{10}e^{i\phi_{10}}|1_P 0_T\rangle + c_{11}e^{i\phi_{11}}|1_P 1_T\rangle, \tag{5.38}$$

where the amplitudes (c_{ij}) of the states have remained unchanged from the initial state, and then taking the overlap of the ideal state with the calculated state:

$$\mathcal{F}(t) = \langle\psi_{id}(t)|\,\rho_{P,T}(t)\,|\psi_{id}(t)\rangle. \tag{5.39}$$

Obviously when field decay processes are included in the calculation of the reduced density operator the fidelity after time $t = 0$ will always be less than 1.

5.4.1 Results

Results were obtained by running a minimisation algorithm optimising both the CPS and the fidelity during the numerical temporal evolution of the master equation. The values of the three detunings $(\delta_1, \delta_2, \delta_3)$ and the classical field Rabi frequency Ω were varied. For each instance of these four parameters the system was evolved to a fixed time $(g_{P,T}t = 60)$. The values for the fidelity $\mathcal{F}$ and the quantity $\phi_{opt} = |\sin(\phi/2)|$ over this time were then maximised, by varying the four parameters, to be as close to unity as possible. We give the details of two sets of parameters that resulted in high fidelity with a large CPS. Despite the large differences in the values for the parameters both sets reach a similar CPS with similar fidelity at close to the same time.

In Figures 5.4 and 5.5 we show the time evolution of the fidelity $(\mathcal{F})$ as calculated from Equation (5.39). We see that in both cases fidelity reaches a peak of $\mathcal{F} \approx 0.9$ which is indicated with the red stars. The evolution of the CPS is presented in Figures 5.6 and 5.7 where a red star indicates the CPS $(\phi \approx 1.5\pi)$ that corresponds to the peak in fidelity. The physical mechanism behind the large-CPS/high-fidelity result lies most likely with an EIT-based nonlinearity. We believe that double EIT is not the
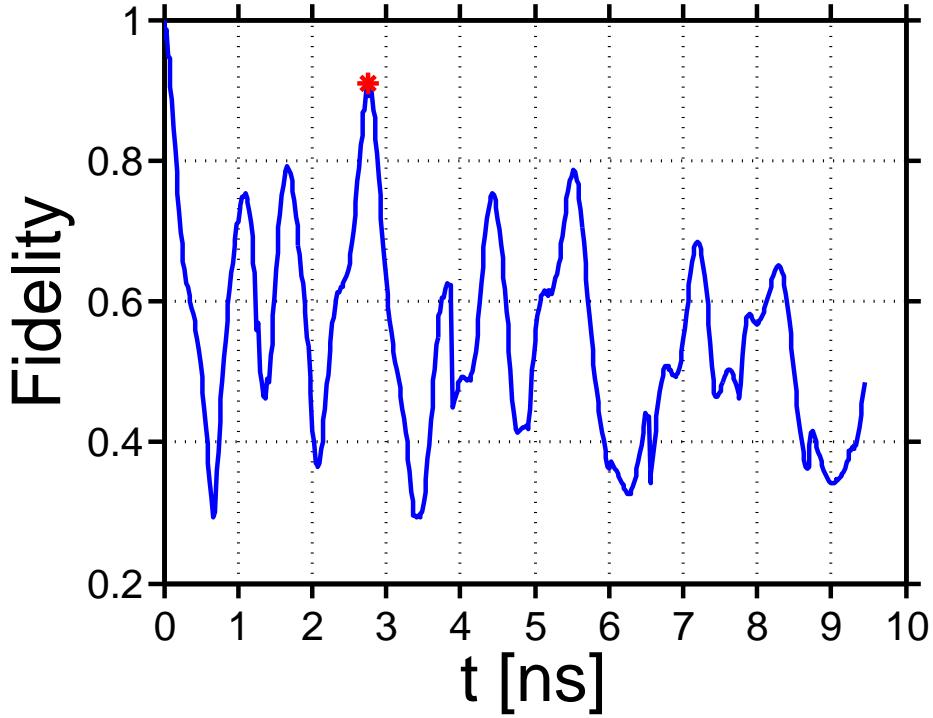
FIGURE 5.4: The time evolution of the fidelity between the ideal state ψ_{id} and the obtained state $\rho_{a,b}(t)$ [see Equation (5.39)] for $\Omega \approx 5.1\, g_{P,T}$ and $(\delta_1, \delta_2, \delta_3) \approx (-4.5, -14.9, -4.1)\, g_{P,T}$. The peak in fidelity is marked with a red star: $\mathcal{F} \approx 0.9$.

mechanism responsible for the large CPS here since the specific values for the detunings prohibit it. In the cases we have found the detuning of the classical field Ω are very different from the detunings of the probe and trigger fields. Hence EIT between the classical field and the probe field is unlikely, and similarly for EIT between the classical and trigger fields. The detunings of the probe and trigger fields, however, are close enough to allow EIT to be established between the probe and the trigger fields. Thus we are led to believe that the XPM interaction occurs between the two quantised fields forming an effective Λ system. The role of the classical field is then to keep the ground state $|2\rangle$ unpopulated and thus preserve the fidelity of the two-qubit gate operation. In the absence of the classical field the decay channel (with rate γ_{22}) would be the dominant decay channel from the excited state. In the transient regime this would result in a non-negligible population of state $|2\rangle$ which would in turn prevent achieving the satisfactory value for the fidelity.

A strange feature in the evolution of the CPS is the rapid and rather large jumps in phase of nearly π that occur regularly. We show the detail of these rapid jumps in Figures 5.6(**b, c**) and 5.7(**b, c**) where red stars denote numerically calculated points, demonstrating that these jumps are continuous in nature. They are thus not numerical artefacts even though the physical mechanism behind these jumps is not clear. Similar behaviour was however found recently in the dynamics of quantum dots [125, 126].
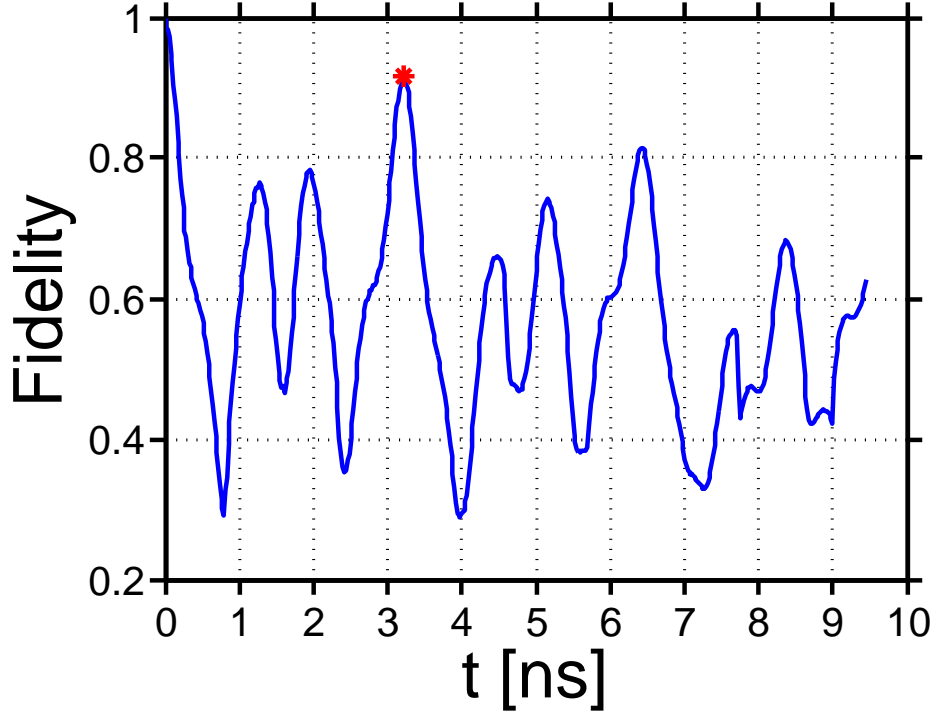
FIGURE 5.5: The time evolution of the fidelity between the ideal state ψ_{id} and the obtained
state $\rho_{a,b}(t)$ [see Equation (5.39)] for $\Omega = 3.2\, g_{P,T}$ and $(\delta_1, \delta_2, \delta_3) \approx (-7.3, -17.6, -7)\, g_{P,T}$.
The peak in fidelity is marked with a red star: $\mathcal{F} \approx 0.9$.

This matter is explored further in Appendix A.

We performed process tomography on the out put state of the simulation follow-
ing the procedure presented in Benenti *et al.* [127] where the quantum operation is
represented in the Fano basis by an affine map. The matrix elements of the process
matrix, χ_F, that characterises the quantum process are real and the number of matrix
elements is equal to the number of free parameters required to determine a generic
quantum operation. We briefly retrace the steps set out in [127] for quantum process
tomography.

An n-qubit state ρ can be written in the Fano form:

$$\rho = \frac{1}{N} \sum_{\alpha_1,\ldots,\alpha_n = x,y,z,I} c_{\alpha_1\ldots\alpha_n} \sigma_{\alpha_1} \otimes \cdots \otimes \sigma_{\alpha_n}, \qquad (5.40)$$

where $N = 2^n$, σ_x, σ_y, and σ_z are the Pauli matrices, $\sigma_I \equiv \mathbb{1}$, and

$$c_{\alpha_1\ldots\alpha_n} = \mathrm{Tr}(\sigma_{\alpha_1} \otimes \cdots \otimes \sigma_{\alpha_n}\rho). \qquad (5.41)$$

The Bloch vector is given by $\mathbf{b} = \{b_\alpha\}_{\alpha=1,\ldots,N^2-1}$ where $b_\alpha \equiv c_{\alpha_1\ldots\alpha_n}$ with $\alpha \equiv \sum_{k=1}^n i_k 4^{n-k}$, with the definition $i_k = 1, 2, 3, 4$ in correspondence to $\alpha_k = x, y, z, I$.
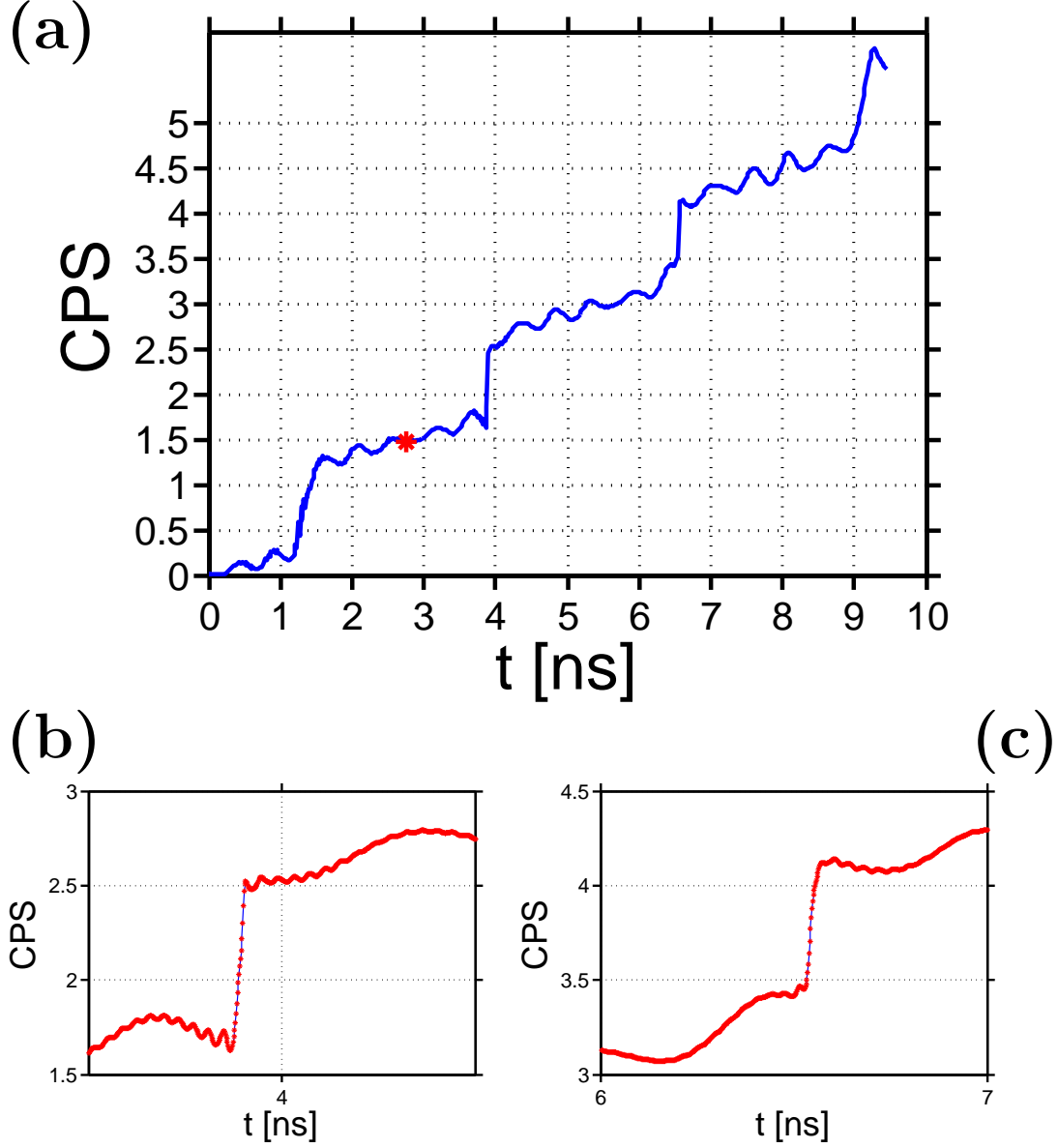
Figure 5.6: (a) The time evolution of the intracavity CPS ϕ (in units of π) for $\Omega = 5.1\, g_{P,T}$ and $(\delta_1, \delta_2, \delta_3) \approx (-4.5, -14.9, -4.1)\, g_{P,T}$. The red star denotes the CPS which corresponds to the peak in fidelity (see Figure 5.4). In (b) and (c) we show detail of the jumps in the phase from (a), here the red stars are numerically calculated points.
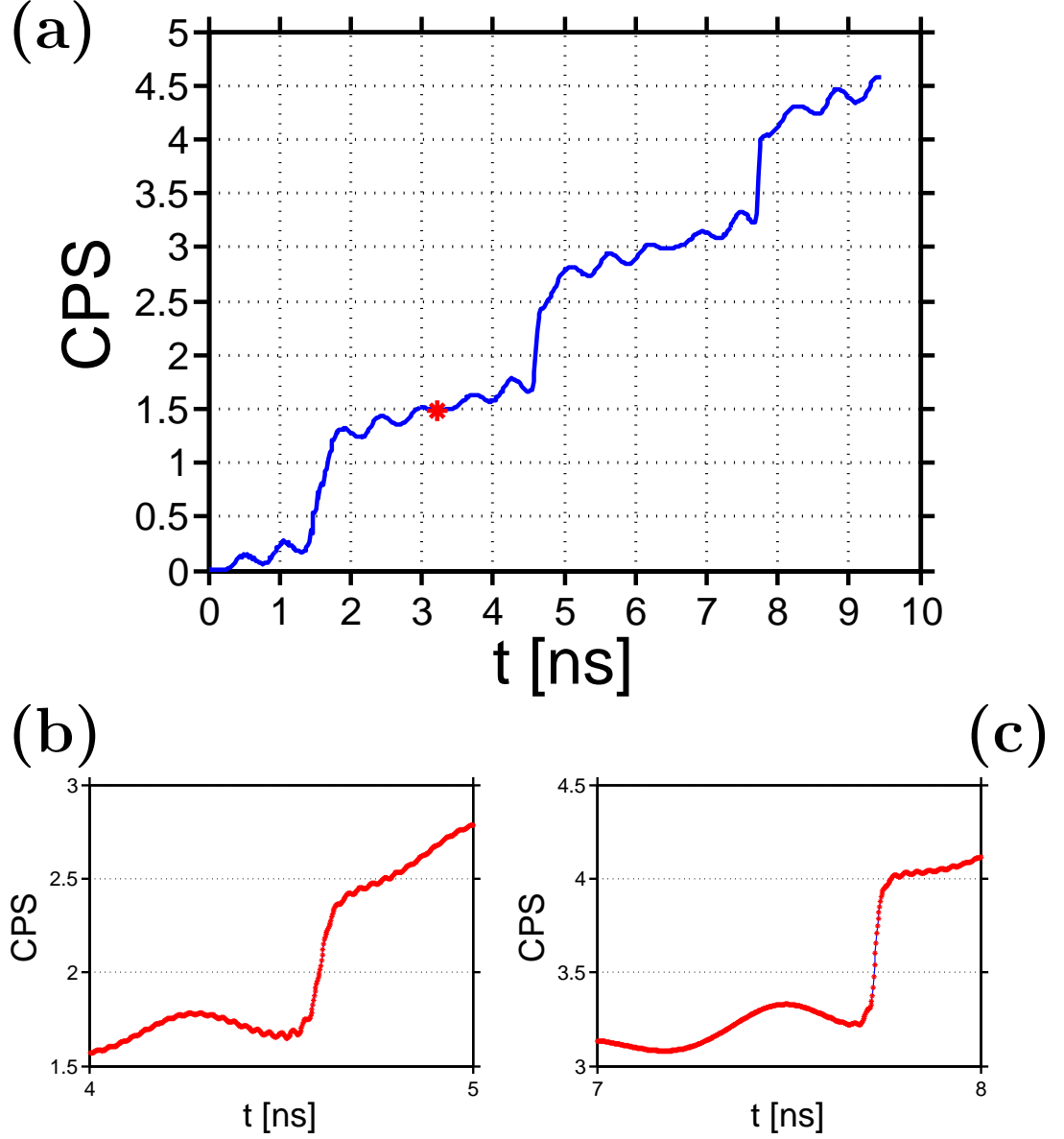
Figure 5.7: The time evolution of the intracavity CPS ϕ (in units of π) for $\Omega = 3.2\, g_{P,T}$ and $(\delta_1, \delta_2, \delta_3) \approx (-7.3, -17.6, -7)\, g_{P,T}$. The red star denotes the CPS which corresponds to the peak in fidelity (see Figure 5.5). In (b) and (c) we show detail of the jumps in the phase from (a), here the red stars are numerically calculated points.

In the case of a two qubit system the Bloch vector is given by

$$\mathbf{b}^T = (b_1, b_2, ..., b_{15}) = (c_{xx}, c_{xy}, c_{xz}, c_{xI}, c_{yx}, c_{yy}, \tag{5.42}$$

$$c_{yz}, c_{yI}, c_{zx}, c_{zy}, c_{zz}, c_{zI}, c_{Ix}, c_{Iy}, c_{Iz}). \tag{5.43}$$

The quantum operation $\rho \to \rho' = \mathcal{E}(\rho)$ is represented in the Fano basis $\{\sigma_{\alpha_1} \otimes ... \otimes \sigma_{\alpha_n}\}$ by an affine map:

$$\left[\frac{\mathbf{b}'}{1} \right] = \mathcal{M} \left[\frac{\mathbf{b}}{1} \right] = \left[\begin{array}{c|c} \mathbf{M} & \mathbf{a} \\ \hline \mathbf{0}^T & 1 \end{array} \right] \left[\frac{\mathbf{b}}{1} \right], \tag{5.44}$$

where $\mathbf{M}$ is a $(N^2 - 1) \times (N^2 - 1)$ matrix, $\mathbf{a}$ a column vector of dimension $N^2 - 1$ and $\mathbf{0}$ the null vector of the same dimension. The quantum operation $\mathcal{E}$ is characterised by the process matrix

$$\chi_F = \left[\begin{array}{c|c} \mathbf{M} & \mathbf{a} \end{array} \right], \tag{5.45}$$

that describes the evolution of the expectation values of the system's polarisation measurements. The process matrix is calculated from experimental data by preparing N^2 linearly independent initial states $\{\rho_i\}$ and allowing them to evolve according to the quantum operation $\mathcal{E}$ and then measuring the resulting states $\{\rho_i' = \mathcal{E}(\rho_i)\}$. By using the Fano representation of the states ρ_i as the columns we can form the $N^2 \times N^2$ matrix $\mathcal{R}$. The corresponding matrix formed from the output states ρ_i' is then $\mathcal{R}'$. The transformation of the ρ_i states into the ρ_i' states are then written as

$$\mathcal{R}' = \mathcal{M}\mathcal{R}, \tag{5.46}$$

and as such

$$\mathcal{M} = \mathcal{R}'\mathcal{R}^{-1}. \tag{5.47}$$

As the linearly independent initial states $\{\rho_i\}$ for our two-qubit system we choose the 16 tensor-product states of the single-qubit states:

$$|0\rangle, \quad |1\rangle, \quad \frac{1}{\sqrt{2}} (|0\rangle + |1\rangle), \quad \frac{1}{\sqrt{2}} (|0\rangle + i |1\rangle). \tag{5.48}$$

The matrix $\mathcal{R}$ is then calculated as:

$$
\mathcal{R} = \begin{bmatrix}
0 & 0 & 0 & 0 & 0 & 0 & 0 & 0 & 0 & 0 & 1 & 0 & 0 & 0 & 0 & 0 \\
0 & 0 & 0 & 0 & 0 & 0 & 0 & 0 & 0 & 0 & 0 & 1 & 0 & 0 & 0 & 0 \\
0 & 0 & 0 & 0 & 0 & 0 & 0 & 0 & 1 & -1 & 0 & 0 & 0 & 0 & 0 & 0 \\
0 & 0 & 0 & 0 & 0 & 0 & 0 & 0 & 1 & 1 & 1 & 1 & 0 & 0 & 0 & 0 \\
0 & 0 & 0 & 0 & 0 & 0 & 0 & 0 & 0 & 0 & 0 & 0 & 0 & 0 & 1 & 0 \\
0 & 0 & 0 & 0 & 0 & 0 & 0 & 0 & 0 & 0 & 0 & 0 & 0 & 0 & 0 & 1 \\
0 & 0 & 0 & 0 & 0 & 0 & 0 & 0 & 0 & 0 & 0 & 0 & 1 & -1 & 0 & 0 \\
0 & 0 & 0 & 0 & 0 & 0 & 0 & 0 & 0 & 0 & 0 & 0 & 1 & 1 & 1 & 1 \\
0 & 0 & 1 & 0 & 0 & 0 & -1 & 0 & 0 & 0 & 0 & 0 & 0 & 0 & 0 & 0 \\
0 & 0 & 0 & 1 & 0 & 0 & 0 & -1 & 0 & 0 & 0 & 0 & 0 & 0 & 0 & 0 \\
1 & -1 & 0 & 0 & -1 & 1 & 0 & 0 & 0 & 0 & 0 & 0 & 0 & 0 & 0 & 0 \\
1 & 1 & 1 & 1 & -1 & -1 & -1 & -1 & 0 & 0 & 0 & 0 & 0 & 0 & 0 & 0 \\
0 & 0 & 1 & 0 & 0 & 0 & 1 & 0 & 0 & 0 & 1 & 0 & 0 & 0 & 1 & 0 \\
0 & 0 & 0 & 1 & 0 & 0 & 0 & 1 & 0 & 0 & 0 & 1 & 0 & 0 & 0 & 1 \\
1 & -1 & 0 & 0 & 1 & -1 & 0 & 0 & 1 & -1 & 0 & 0 & 1 & -1 & 0 & 0 \\
1 & 1 & 1 & 1 & 1 & 1 & 1 & 1 & 1 & 1 & 1 & 1 & 1 & 1 & 1 & 1
\end{bmatrix}, \tag{5.49}
$$

while $\mathcal{R}'$ is calculated by using each of the 16 initial states as the initial state of the
fields in our simulation and then obtaining the Fano representation of the final state of
the system at the time when we have previously obtained a peak in fidelity, see Figures
5.4 and 5.5.

The Choi matrix [128] for the process can be obtained from the process matrix χ_F:
The Choi fidelity is given by the trace fidelity of the Choi matrices for the simulated
process and the ideal process:

$$
F_C = \mathrm{Tr}\left[\chi_{sim}\,\chi_{ideal}\right]. \tag{5.50}
$$

5.4.2 Conclusion

We have demonstrated in this chapter that a *single* NV centre nanodiamond coupled
to an ultra-high Q cavity could induce, with a high fidelity, a CPS in excess of π in
two cavity fields coupled to two transitions of the four-level tripod scheme realised in
the NV centre. Such a large CPS would allow the implementation of a CZ gate and
as such would allow a CNOT gate if single photon Hadamard gates are applied to the
target qubit before and after the CZ gate interaction. It has also been shown that all
the technologies required have been demonstrated close to or upto the level required
to realise this system experimentally:

1. Single NV centres in nanodiamonds are available

2. Nanodiamonds can be accurately positioned on microresonators

3. Ultra-high Q cavities for NV centre optical transition wavelengths are under
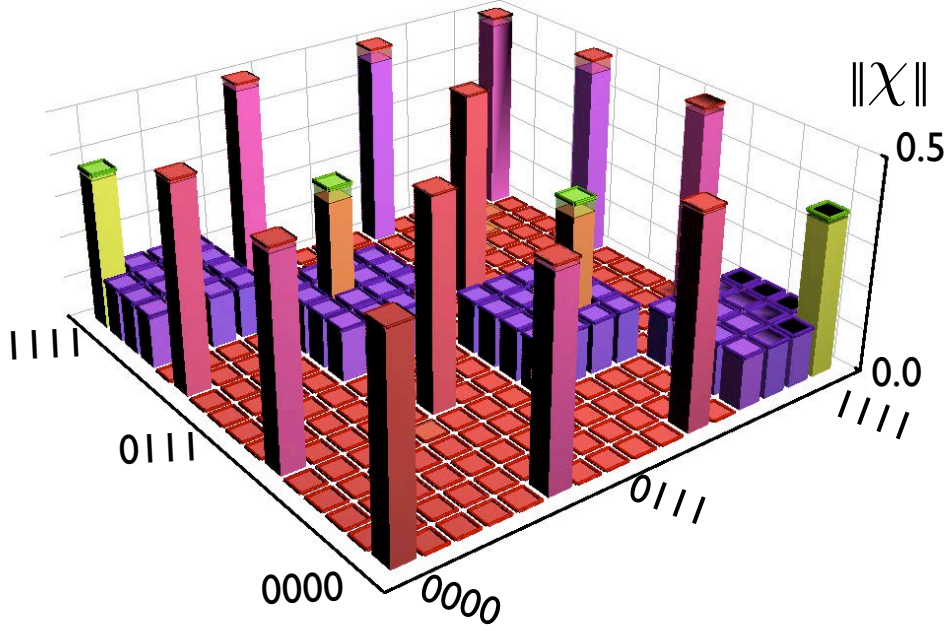   investigation

FIGURE 5.8: The Choi matrix for the simulated process (solid bars) obtained by process tomography, and the Choi matrix for the ideal process (transparent bars) with a CPS equal to that of the simulation. The trace fidelity between the two matrices is 0.98, indicating that the implemented process is very close to the ideal process.

4. Large coupling between NV centres and cavity fields have been demonstrated and would be larger for better cavities

We also found an interesting regular feature where the CPS jumps by nearly π radians.

6

Breeding Schrödinger cats with diamonds

In this chapter we explain how the system introduced in section 5.4 can be used in the preparation of optical macroscopically distinguishable states, also known as Schrödinger cat states (from the *gedankenexperiment* of Schrödinger [129]). An optical cat state consists of two quasi-classical states with opposite phases in a quantum superposition, the cat state then possesses opposite phases simultaneously. Several uses exist for cat states, from tests of quantum theory (e.g. through violations of Bell inequalities [2–4]) through to applications in quantum information processing [130–133].

Due to strong interactions with the environment quantum superpositions in macroscopic systems decohere rapidly. Yurke and Stoler [134] first showed that an optical coherent state propagating through a medium with an intensity dependent refractive index (i.e. a self-Kerr medium, $H = \hbar\chi \left(a^\dagger a\right)^2$) can evolve into a quantum superposition state. The coherent state evolves into a Schrödinger cat state at time $t = \pi/2\chi$ and in order to minimise the effects of decoherence a strong self-Kerr interaction is required, i.e.. $\chi \sim \pi$, making standard Kerr media with their weak nonlinearities ill suited for the job. Brune *et al.* [135] introduced a way of generating cats through the conditional measurement of a subsystem which is correlated with another subsystem that can then be left in a Schrödinger cat state. In [135] they considered the case when an atom is dropped through a cavity where it entangles with an optical coherent field. In that case atom and the field constitute the two subsystems. Vitali *et al.* [136] introduced the notion that the two subsystems could be optical coherent fields undergoing a cross-Kerr interaction. A measurement by homodyne detection on one coherent field will then herald the creation of a cat state in the other field. After reviewing this last work, which uses an ideal cross-Kerr evolution of two coherent states followed by measurement we will investigate the possibility of using the system of section 5.4 in this method of cat-state generation.

6.1   The ideal cross-Kerr cat breeder

On account of the relatively weak interaction of light with the environment super-positions of macroscopically distinguishable coherent optical states $|\alpha\rangle$ form an ideal physical system in which to realise cat states. The Schrödinger cat state is then defined by $|\psi\rangle = \mathcal{N}\left(|\alpha\rangle + e^{i\theta}|-\alpha\rangle\right)$ where $\mathcal{N}$ is a normalisation constant and the coherent amplitude is α. The "size" of the cat is given by the average number of photons $|\alpha|^2$ in the coherent field, while the overlap between the "live" and "dead" cat is given by $\langle\alpha|-\alpha\rangle = e^{-2|\alpha|^2}$ which is required to be small by most quantum information processing applications: the overlap will be less than 1% when $|\alpha|^2 \gtrsim 2.3$. The coherent state $|\alpha\rangle$ can be written in the Fock (number) state basis as

$$|\alpha\rangle = e^{-|\alpha|^2/2} \sum_{n=0}^{\infty} \frac{\alpha^n}{\sqrt{n!}} |n\rangle , \qquad (6.1)$$

Taking the simplest most ideal situation with no damping and no driving the Hamiltonian describing the cross-Kerr interaction between two modes a and b is given by

$$H_{int} = \hbar\chi \left(\hat{a}^\dagger \hat{a} \hat{b}^\dagger \hat{b}\right) , \qquad (6.2)$$

The strength of the cross-Kerr interaction is given by χ. With the initial state of the fields being

$$|\psi(0)\rangle = |\alpha_0\rangle |\beta_0\rangle , \qquad (6.3)$$

where $|\alpha_0\rangle$ and $|\beta_0\rangle$ are coherent states of the a and b modes respectively. We write the evolved state at time t as

$$\begin{aligned}
|\psi(t)\rangle &= e^{(-i/\hbar)H_{int}t} |\psi(0)\rangle \\
&= e^{-|\alpha|^2/2} e^{-|\beta|^2/2} \sum_{n_a,n_b=0}^{\infty} \frac{\alpha_0^{n_a}\beta_0^{n_b}}{\sqrt{n_a!n_b!}} e^{-i\chi t(n_a n_b)} |n_a\rangle |n_b\rangle .
\end{aligned} \qquad (6.4)$$

At time $t = \pi/\chi$ we have $e^{i\chi n_a n_b t} = (-1)^{n_a n_b}$ such that the sum in Equation (6.4) can be divided into two parts, one with n_a even and the other with n_a odd:

$$\begin{aligned}
|\psi(\pi/\chi)\rangle = e^{-|\alpha|^2/2} e^{-|\beta|^2/2} &\left(\sum_{n_a=even}^{\infty} \frac{\alpha_0^{n_a}}{\sqrt{n_a!}} |n_a\rangle \sum_{n_b=0}^{\infty} \frac{\beta_0^{n_b}}{\sqrt{n_b!}} |n_b\rangle \right. \\
&\left. + \sum_{n_a=odd}^{\infty} \frac{\alpha_0^{n_a}}{\sqrt{n_a!}} |n_a\rangle \sum_{n_b=0}^{\infty} \frac{(-\beta_0)^{n_b}}{\sqrt{n_b!}} |n_b\rangle \right) \\
= \frac{1}{2}\left\{|\alpha_0\rangle + |-\alpha_0\rangle\right\} |\beta_0\rangle &+ \frac{1}{2}\left\{|\alpha_0\rangle - |-\alpha_0\rangle\right\} |-\beta_0\rangle .
\end{aligned} \qquad (6.5)$$

Two kinds of cat states can be obtained, the even cat state $|\alpha_0\rangle + |-\alpha_0\rangle$, or the odd cat state $|\alpha_0\rangle - |-\alpha_0\rangle$. We can identify situations where the a mode is in a cat state by making a measurement of the b mode at time $t = \pi/\chi$ that discriminates between

states $|\beta_0\rangle$ and $|-\beta_0\rangle$. As suggested by Vitali *et al.* [136] this can be done with a homodyne measurement of the quadrature of mode b

$$X_b = \frac{1}{2}\left(\hat{b}e^{-i\phi_b^0} + \hat{b}^\dagger e^{-i\phi_b^0}\right), \tag{6.6}$$

where $\phi_b^0 = \arg(\beta_0)$. As mentioned with large enough β_0 the overlap between the two states are small and the measurement will easily discriminate between them, yielding $|\beta_0\rangle$ half of the time and $|-\beta_0\rangle$ the other half. When the measurement result is $|\beta_0\rangle$ the state of the system becomes:

$$|\psi(\pi/\chi)\rangle_{X_b} = N\left(\{|\alpha_0\rangle + |\alpha_0\rangle\}|\beta_0\rangle + \langle\beta_0| - \beta_0\rangle\{|\alpha_0\rangle - |\alpha_0\rangle\}|\beta_0\rangle\right), \tag{6.7}$$

which, with large β_0, results in the a mode subensemble being in the even cat state. The normalisation constant N is given by

$$N = 1/\sqrt{\langle\beta_0| - \beta_0\rangle\langle\alpha_0| - \alpha_0\rangle + \langle-\beta_0|\beta_0\rangle\langle-\alpha_0|\alpha_0\rangle + \langle\beta_0| - \beta_0\rangle\langle\beta_0| - \beta_0\rangle}, \tag{6.8}$$

which with large β_0 will be equal to one.

A very useful way to visualise macroscopic superposition states is with the quasi-distribution function, the Wigner function, defined as

$$W(\alpha, \alpha^*) = \frac{1}{\pi^2}\int d^2\gamma\, e^{-i\gamma\alpha^* - i\gamma^*\alpha}\,\mathrm{Tr}\left[e^{i\gamma\hat{a}^\dagger + i\gamma^*\hat{a}}\rho\right]. \tag{6.9}$$

In Figure 6.1 we show the Wigner function calculated for an ideal Schrödinger cat state, i.e. a state that is a perfect superposition of a positive and a negative coherent state $|\psi\rangle_{IDcat} = N\{|\alpha_0\rangle + |-\alpha_0\rangle\}$, where $\alpha_0 = \beta_0 = \sqrt{3}$. Of note is the two peaks, one corresponds with the "living" cat ($|\alpha_0\rangle$) the other with the "dead" cat ($|-\alpha_0\rangle$); and the rapid oscillations with negative troughs between the two peaks due to the interference between the two states. When the Wigner function of a quantum state has negative values the state can not be described by a classical phase-space density and as such it is clear that the state is indeed nonclassical and not simply a mixture of coherent states. The separation distance between the two Gaussian peaks corresponding to the coherent states increases as the average photon number in the coherent states increases. Further more the frequency of the interference oscillations increase with separation [137].

6.2 Cats in the tripod configured single NV centre and high-Q cavity system

Considering the results in chapter 5 where our simulations yielded a large CPS between two single photon fields it seemed likely that two coherent fields as the input probe and trigger fields could evolve into a state closely resembling that in Equation (6.5). A projective measurement of the b mode after sufficient time ($t = \pi/\chi$) would then leave mode a in a cat state. As such we use the same setup as in section 5.4 for the
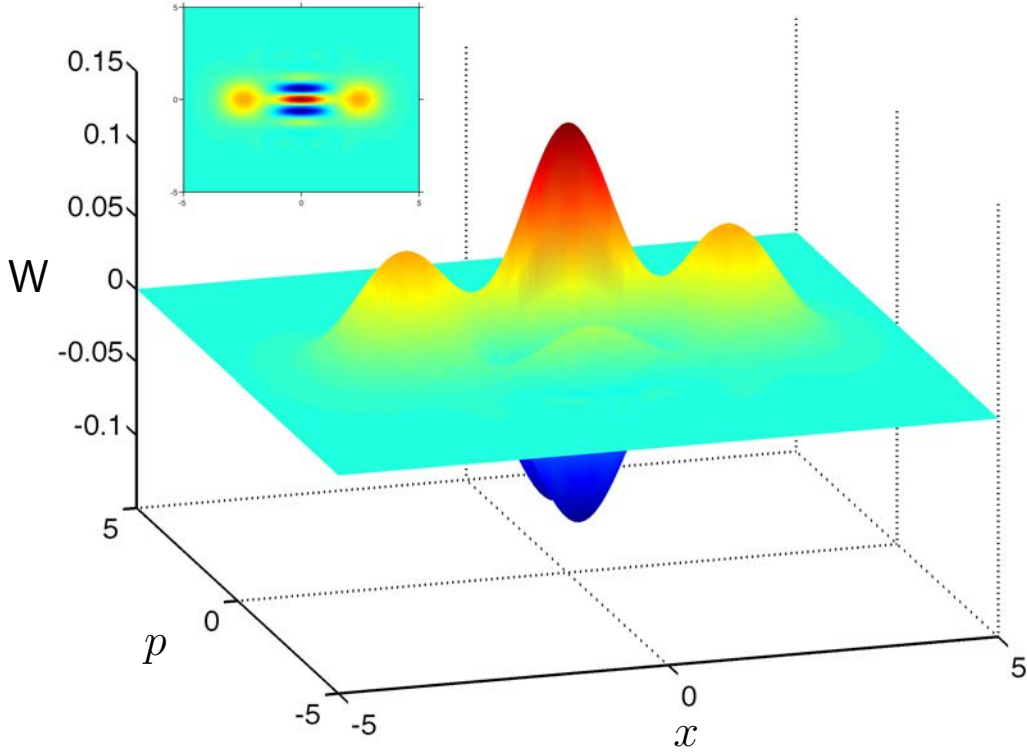
Figure 6.1: The Wigner distribution of an ideal cat state $|\psi\rangle_{IDcat} = N\{|\alpha_0\rangle + |-\alpha_0\rangle\}$ where $\alpha_0 = \beta_0 = \sqrt{3}$. The inset shows the view from the top.

simulations here, with the one change being the use of coherent states in place of single photon states as inputs. We assume a tripod-level (Figure 5.3) configured NV centre with parameters taken from literature (see Table 5.1). The Hamiltonian of the system is given by

$$
\begin{aligned}
H_{sys} =& \hbar\delta_1\hat{\sigma}_{00} + \hbar\left(\delta_1 - \delta_2\right)\hat{\sigma}_{22} + \hbar\left(\delta_1 - \delta_3\right)\hat{\sigma}_{33} \\
& + \hbar g_P\left(\hat{a}^\dagger\hat{\sigma}_{10} + \hat{a}\hat{\sigma}_{01}\right) + \hbar\Omega\left(\hat{\sigma}_{20} + \hat{\sigma}_{02}\right) \\
& + \hbar g_T\left(\hat{b}^\dagger\hat{\sigma}_{30} + \hat{b}\hat{\sigma}_{03}\right).
\end{aligned}
\tag{6.10}
$$

Where $\hat{\sigma}_{ij} = |i\rangle\langle j|$ $(i, j = 0, 1, 2, 3)$ are the atomic coherences, and $\hat{a}$ and $\hat{b}$ are the probe (mode a) and trigger (mode b) field annihilation operators respectively. The time evolution of the system is governed by the master equation in the Lindblad form:

$$
\dot{\rho} = -\frac{i}{\hbar}\left[H_{sys}, \rho\right] + \left(\mathcal{L}_{cav} + \mathcal{L}_{spon} + \mathcal{L}_{ph}\right)\rho,
\tag{6.11}
$$

where the decoherence terms are

$$\mathcal{L}_{cav}\rho = \kappa_P \left(2\hat{a}\rho\hat{a}^\dagger - \hat{a}^\dagger\hat{a}\rho - \rho\hat{a}^\dagger\hat{a}\right) + \kappa_T \left(2\hat{b}\rho\hat{b}^\dagger - \hat{b}^\dagger\hat{b}\rho - \rho\hat{b}^\dagger\hat{b}\right)$$

$$\mathcal{L}_{spon}\rho = \frac{\gamma_{11}}{2}\left(2\hat{\sigma}_{10}\rho\hat{\sigma}_{01} - \hat{\sigma}_{00}\rho - \rho\hat{\sigma}_{00}\right) + \frac{\gamma_{22}}{2}\left(2\hat{\sigma}_{20}\rho\hat{\sigma}_{02} - \hat{\sigma}_{00}\rho - \rho\hat{\sigma}_{00}\right)$$

$$+ \frac{\gamma_{33}}{2}\left(2\hat{\sigma}_{30}\rho\hat{\sigma}_{03} - \hat{\sigma}_{00}\rho - \rho\hat{\sigma}_{00}\right)$$

$$\mathcal{L}_{ph}\rho = \frac{\gamma_{ph}}{2}\left(2\hat{\sigma}_{11}\rho\hat{\sigma}_{11} - \rho\hat{\sigma}_{11} - \hat{\sigma}_{11}\rho\right) + \frac{\gamma_{ph}}{2}\left(2\hat{\sigma}_{22}\rho\hat{\sigma}_{22} - \rho\hat{\sigma}_{22} - \hat{\sigma}_{22}\rho\right)$$

$$+ \frac{\gamma_{ph}}{2}\left(2\hat{\sigma}_{33}\rho\hat{\sigma}_{33} - \rho\hat{\sigma}_{33} - \hat{\sigma}_{33}\rho\right). \tag{6.12}$$

For simplicity we take the cavity decay rates for the probe and trigger fields as being equal, $\kappa_P = \kappa_T = \kappa$. The state of the coherent input fields is

$$|\varphi(0)\rangle_{a,b} = |\alpha_0\rangle\,|\beta_0\rangle, \tag{6.13}$$

and the initial population of the atomic system is taken to be even between state $|1\rangle$ and $|3\rangle$ and as such the initial state of the system is given by:

$$\rho(0) = \left(\frac{1}{2}\,|1\rangle\,\langle 1| + \frac{1}{2}\,|3\rangle\,\langle 3|\right) \otimes \left(|\varphi(0)\rangle_{a,b}\,\langle\varphi(0)|\right). \tag{6.14}$$

From our previous study in chapter 5 we know that this Hamiltonian acts like the ideal cross-Kerr Hamiltonian (6.2) but with additional linear terms proportional to $\hat{a}^\dagger\hat{a}$ and $\hat{b}^\dagger\hat{b}$. With the real value of χ unknown we make use of a recent measure for quantifying macroscopic quantum superpositions [138] to determine how close to a Schrödinger cat state mode a is at each time step in the evolution. We maximise this measure with respect to the detunings δ_1, δ_2, δ_3 and classical field Rabi frequency Ω and the time. An effective measure for a macroscopic superposition must quantify the degree of superposition against an incoherent mixture, as well as the effective size of the state, e.g.. the average number of photons. A recent measure proposed by Lee et $al.$ [138] makes use of the phase-space representation of the state, the Wigner function. The Wigner function of a macroscopic superposition of two states has two well defined peaks with interference fringes between them. The frequency of the fringes is proportional to the "size" of the superposition, i.e. how distinguishable the two states are from each other. While the magnitude of the fringes relate to the "coherence" of the superposition, or how different the superposition is from a completely mixed version. The measure $\mathcal{I}(\rho)$ can be easily calculated

$$\mathcal{I}(\rho) = -\mathrm{Tr}\left[\rho\mathcal{L}(\rho)\right], \tag{6.15}$$

where $\mathcal{L}(\rho)$ is the superoperator in the Lindblad form

$$\frac{d\rho}{d\tau} = \mathcal{L}(\rho) = \left(\hat{a}\rho\hat{a}^\dagger - \frac{1}{2}\hat{a}^\dagger\hat{a}\rho - \frac{1}{2}\rho\hat{a}^\dagger\hat{a}\right), \tag{6.16}$$

where $\tau = (\mathrm{decayrate}) \times (\mathrm{time})$ is the dimensionless time.

$\mathcal{I}(\rho)$ gives a maximum value $\langle \hat{n} \rangle$ (the number of particles for ρ) only for pure states, and has a minimum value $\mathcal{I}(\rho) = 0$ for completely mixed states. Thus no matter how many particles are in the state if there is no potential for quantum interference $\mathcal{I}(\rho) = 0$. For an ideal cat state

$$|\psi\rangle_{IDcat} = \frac{1}{\sqrt{2}}|\alpha_0\rangle + \frac{1}{\sqrt{2}}|-\alpha_0\rangle, \tag{6.17}$$

the macroscopic quantum superposition measure is related to α_0 as

$$\mathcal{I}(\rho_{IDcat}) = \langle \hat{n} \rangle = \alpha_0^2 \tanh \alpha_0^2. \tag{6.18}$$

It is against this value that we must compare our generated cats. For the ideal Schrödinger cat with $\alpha_0 = \sqrt{3}$ (depicted in Figure 6.1), $\mathcal{I} = 2.9852$. Another important measure is the purity of the state given by

$$P = \text{Tr}(\rho^2), \tag{6.19}$$

which should ideally be equal to one.

We present here some examples of states obtained in our simulation that have very high measures of macroscopic quantum superposition. The Wigner distribution in Figure 6.2 displays the necessary features for a macroscopic superposition state: two peaks with interference fringes with negative parts between them. The parameters we used for the generation of this state were $(\delta_1, \delta_2, \delta_3) \approx (-4.78, -14.93, -3.86)\, g_{P,T}$ for the detunings and $\Omega \approx 5.10\, g_{P,T}$ for the Rabi frequency. The input coherent states had amplitudes $\alpha_0 = \beta_0 = \sqrt{3}$ and the sytem evolved for a $t \approx 8.5$ns. The state depicted in Figure 6.2 has a measure $\mathcal{I} = 2.84$ out of a maximum of $\mathcal{I}_{ID} = 2.9852$, and a purity $P = 0.78$.

For Figure 6.3 the parameters we used were $(\delta_1, \delta_2, \delta_3) \approx (-7.66, 0.00, -6.93)\, g_{P,T}$ for the detunings and $\Omega = 0\, g_{P,T}$ for the Rabi frequency. The same input coherent state amplitudes $\alpha_0 = \beta_0 = \sqrt{3}$ were used and the sytem evolved for a $t \approx 11.4$ns. Since the classical field that would connect the $|2\rangle \rightarrow |0\rangle$ transition is not present the tripod system reduces down to a λ system. The macroscopic quantum superposition measure for this state was $\mathcal{I} = 2.93$, extremely close to the maximum of $\mathcal{I}_{ID} = 2.9852$, and the purity was $P = 0.81$.

It should be noted that due to constraints on computing power we could not use a larger coherent field for the b mode. With $|\beta_0|^2 = 3$ we have $\langle \beta_0| - \beta_0 \rangle \approx 0.0024$ which results in the final state of the system after the projective measurement being a mixture of the even and odd cats.

In conclusion we have shown that there is the potential that a single NV centre coupled to WGMs of a high-Q cavity could be used for the generation of Schrödinger cat states from coherent state input modes. Cat states have many uses, and the deterministic on demand generation of cat states would hold great benefit for quantum information applications.
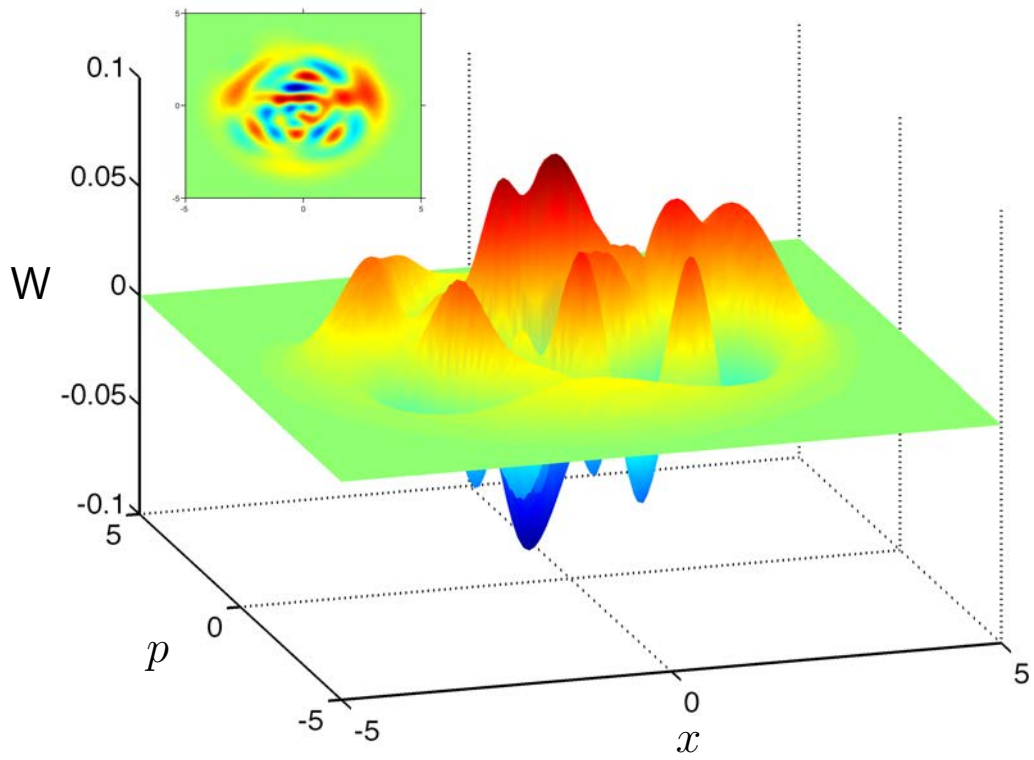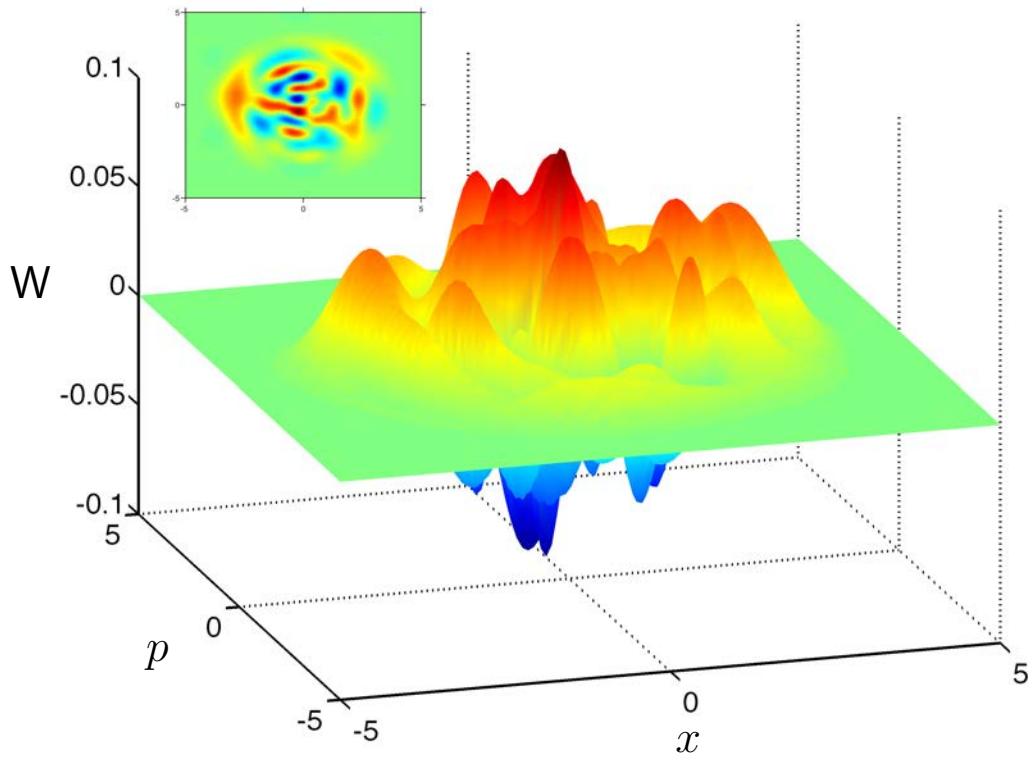
FIGURE 6.2: A cat state created by the cross-Kerr interaction in the tripod system. The detunings were $(\delta_1, \delta_2, \delta_3) \approx (-4.78, -14.93, -3.86)\, g_{P,T}$ for the detunings and $\Omega \approx 5.10\, g_{P,T}$. The system was evolved for $t \approx 8.5\, \text{ns}$. The inset shows the view from the top.

FIGURE 6.3: The cat state created by the cross-Kerr interaction in a tripod system. The detunings were $(\delta_1, \delta_2, \delta_3) \approx (-7.66, 0.00, -6.93)\, g_{P,T}$ for the detunings and $\Omega = 0\, g_{P,T}$ for the Rabi frequency. The system was evolved for $t \approx 11.4\,\mathrm{ns}$. The inset shows the view from the top.

7
Conclusion

In this thesis we investigated methods related to achieving interaction between photonic qubits. The first general approach by which to achieve this is to transfer photonic qubits to solid state systems, where the qubit interactions can then take place. We review several techniques related to the transfer of optical qubits to solid state systems, and optimise one of them for situations with large inhomogeneities in the solid state system. The other approach is to enhance the strength of the photon-photon interaction. We review some ways in which to achieve this photon-photon interaction in linear optics, and propose a system with a single NV centre in a cavity-QED setting enhancing the nonlinear interaction between photons.

We demonstrated in chapter 3 that the SCRAP pulses can be optimised further to increase the fidelity of population transfer amongst the two ground states of a Λ-type three level system for a wide range of different field detunings. This concept of coherent population transfer is closely related to EIT and the storage of the quantum state of light in the spin coherences of the system. Unlike STIRAP, SCRAP does not require two-photon resonance (i.e. detunings that are all equal) in order to achieve population transfer. This means that SCRAP is far more insensitive to inhomogeneous broadening of the energy levels in the system.

We have shown that the range of detunings where population transfer is at all possible is around 35.5% larger using the optimised SCRAP pulses compared to the original pulses. Furthermore it was shown that the fidelity of population transfer for those detunings where it was possible is greatly increased when using the optimised pulses. The optimised pulses increased the average fidelity of population transfer for the detuning space under investigation by 46.6%. It is clear that SCRAP is a useful process to employ when trying to overcome inhomogeneous broadening of energy levels in a system undergoing state transfer. Solid state systems typically suffer the greatest inhomogeneous broadenings due to the different electronic environments each atomic centre finds itself in because of crystal defects and other strain related phenomena.

In chapter 5 we conclude that a *single* NV centre strongly coupled to high-Q WGMs of a microresonator could induce a sufficiently large CPS with a high fidelity for the implementation of a QPG. In particular, the CPS calculated would allow for a CZ gate, a two-qubit gate essential for optical quantum computing. A great advantage of only using a single atomic centre is the fact that there is no inhomogeneous broadening of the energy level transitions. The establishment of EIT between the probe and trigger fields lies at the heart of the large CPS achievable. We calculate that a CPS of $\phi \approx 1.5\pi$ radians is achieved with a fidelity $\mathcal{F} \approx 0.9$. We also conclude that the elements comprising this scheme exist and are at or close to the quality required to realise a large CPS. We also found an interesting regular feature where the CPS jumps by nearly π radians. This feature, or something similar, has previously been observed in quantum dot experiments, and the further study of the physical mechanism behind this phenomenon has merit.

This proposal for the implementation of a QPG has several advantages over current well established methods. The current linear optics based methods (KLM schemes) are either probabilistic or if nearly deterministic still require a large over head of additional qubits for the computation. These methods also require an optical lab with many large optical elements. The scheme we propose should be able to accommodate many QPGs on a single chip. Admittedly this will not be easy to manufacture and assemble with current fabrication techniques. One could also envision simulations of networks of the proposed NV-cavity scheme.

In chapter 6 we give numerical evidence that Schrödinger cat states can be created using the single NV tripod scheme introduced in chapter 5, by using weak coherent fields for the probe and trigger fields. We make use of a recent measure for macroscopic quantum superposition and find that states with values $\mathcal{I} = 2.93$, close to the maximum $\mathcal{I}_{max} = 2.9852$, can be found. Cat states have several uses within quantum information processing and can be used for tests of Bell's inequalities. Due to the scalable solid state system proposed here for the generation of cats it could be possible to have access to a large number of cats for computing purposes.

Future work

Several possibilities for future investigation have been opened by our research. Firstly the question arises whether an analogy of SCRAP could be implemented with weak/quantum fields. Essentially such a protocol would be standard EIT with an added Stark shift pulse. Research into this would have to consider the field propagation equations as is done for EIT and evaluate the transparency window and slow down effect on the quantum field. The possibility of the application of this technique in a quantum memory context is uncertain since most current quantum memory systems do not suffer from large inhomogeneous broadening between the ground states.

Further investigation of an NV centre and high-Q WGM microresonator based QPG could take the form of an experiment coupling a single NV centre in a nano-diamond to a high-Q cavity and investigating the phase shifts achievable with such a system. All the required techniques and components for such an experiment already exist. The challenge would be in getting all these cutting edge experimental components to come

together in one experiment.

Certainly further investigation into the generation of Schrödinger cat states with the aid of high-Q cavities is warranted. A further prospect is simulating established methods for computation with Schrödinger cats using cats derived from our simulations instead of ideal cats, thus closer simulating the real world performance of these computations.

<div align="right">

A
Appendix

</div>

In Chapter 5 we saw that the results for the CPS showed sudden changes of almost π at a regular interval, as depicted in Figures 5.6 and 5.7. In and of itself neither the magnitude of the phase jumps nor the timescale on which they happen is that interesting: similarly sized sudden phase jumps are seen in previous results, see Figure A.1, taken from Rebić *et al.* [90]. The most obvious difference between the jumps in previous results and that of ours is that in our results the jumps occur at regular intervals, and only in one direction.

In an attemt to find the reason for these regular phase jumps we first note that, as stated in chapter 5, the detuning δ_2 is substantially greater than δ_1 and δ_3 and as such there is no possiblility for double EIT. The classical field thus only serves to prevent population from accumulating in state $|2\rangle$ and we should be able to see similar results in a simplified Λ-system. Sticking with the convention we used in Chapter 5 of $|0\rangle$ as the exited state the Hamiltonian of the Λ system is similar to that of the tripod 5.31 just with all terms relating to $|2\rangle$ removed:

$$
\begin{aligned}
H_{sys} = {} & \hbar\delta_1\hat{\sigma}_{00} + \hbar\left(\delta_1 - \delta_3\right)\hat{\sigma}_{33} + \hbar g_P\left(\hat{a}^\dagger\hat{\sigma}_{10} + \hat{a}\hat{\sigma}_{01}\right) \\
& + \hbar g_T\left(\hat{b}^\dagger\hat{\sigma}_{30} + \hat{b}\hat{\sigma}_{03}\right).
\end{aligned} \tag{A.1}
$$

We make use of the exact same methodology for calculating the CPS as in Chapter 5. For simplicity we ignore all decay and dephasing (thus ignoring the cavity). With this unitary evolution of the system we find that we can obtain similar results displaying rapid phase jumps in a Λ-system, see Figure A.2.

In a further attempt to simplify the system we adiabatically eliminate the excited state $|0\rangle$ from the Λ-system A.1 to obtain an effective two-level system. We follow the
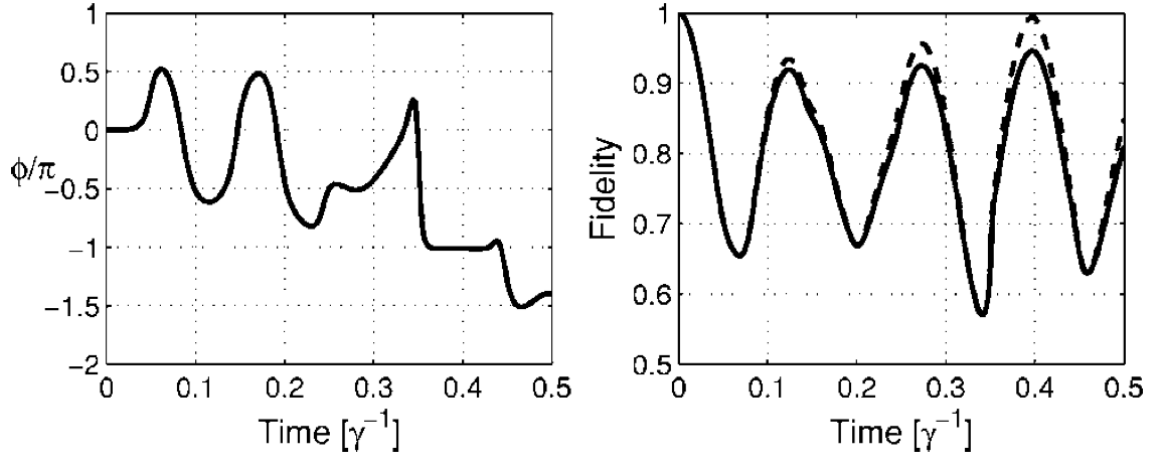
FIGURE A.1: Figure taken from Rebić *et al.* [90] showing large sudden phase jumps in the graph on the left, accompanied with the fidelity of the QPG operation on the right. $\gamma = 2\pi \times 6\text{MHZ}$.

methods used by E. Brion *et al.* [139]. We write the Hamiltonian A.1 as

$$H = H_0 + V, \tag{A.2}$$

where

$$H_0 = \hbar\delta_1\hat{\sigma}_{00} + \hbar\left(\delta_1 - \delta_3\right)\hat{\sigma}_{33},$$
$$V = \hbar g_P\hat{a}^\dagger\hat{\sigma}_{10} + \hbar g_T\hat{b}^\dagger\hat{\sigma}_{30},$$
$$+ \hbar g_P\hat{a}\hat{\sigma}_{01} + \hbar g_T\hat{b}\hat{\sigma}_{03}. \tag{A.3}$$

We also define the projectors

$$P^+ = |0\rangle\langle 0|,$$
$$P^- = |1\rangle\langle 1| + |3\rangle\langle 3|, \tag{A.4}$$

onto the excited and ground states respectively. The effective two level Hamiltonian is given by

$$H_{eff} = P^-H_0P^- + P^-RP^-, \tag{A.5}$$

where R is defined by

$$R = V + V\frac{P^+}{-P^+H_0P^+ - P^+VP^+}V, \tag{A.6}$$

The effective two-level Hamiltonian is then calculated as

$$H_{eff} = \hbar\left(\delta_1 - \delta_3\right)\hat{\sigma}_{33} - \frac{\hbar g_T^2}{\delta_1}\hat{b}^\dagger\hat{b}\hat{\sigma}_{33} - \frac{\hbar g_P^2}{\delta_1}\hat{a}^\dagger\hat{a}\hat{\sigma}_{11} - \frac{\hbar g_T g_P}{\delta_1}\left(\hat{a}^\dagger\hat{b}\hat{\sigma}_{13} + \hat{a}\hat{b}^\dagger\hat{\sigma}_{31}\right). \tag{A.7}$$

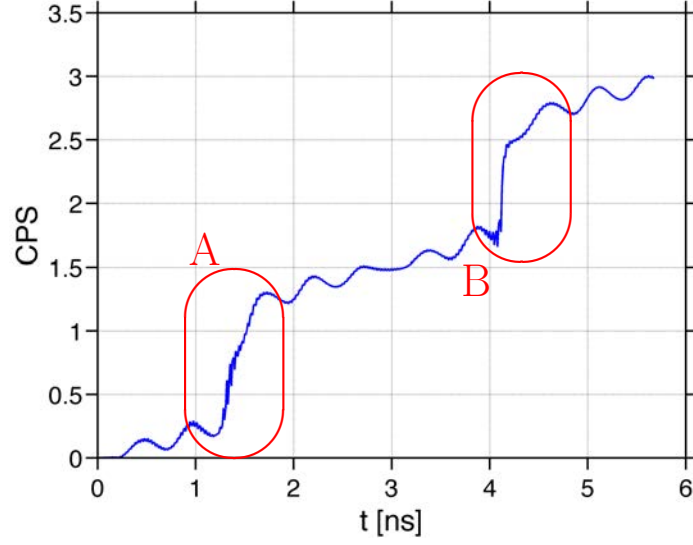FIGURE A.2: CPS calculated in a Λ system with detunings: $(\delta_1, \delta_3) \approx (-7.48, -7.14)\, g_{P,T}$ and all other parameters the same as used for the tripod system, except all decay rates are set to zero. The encircled regions labeled A and B show the sudden large phase jumps.

The CPS obtained by making use of this effective two-level Hamiltonian is given in Figure A.3, which corresponds well with the previous Λ-system results. A difference of note is the sudden jumps in phase denoted by A and B in Figures A.2 and A.3. In the effective two-level system each of these large phase jumps consist of two smaller jumps in phase much closer in scale to the regular oscillating jumps seen elsewhere in Figure A.3.

We are no closer to explaining these phase jumps, but we see that this feature is not out of the ordinary and has to a degree been seen in similar simulations evaluating CPS.
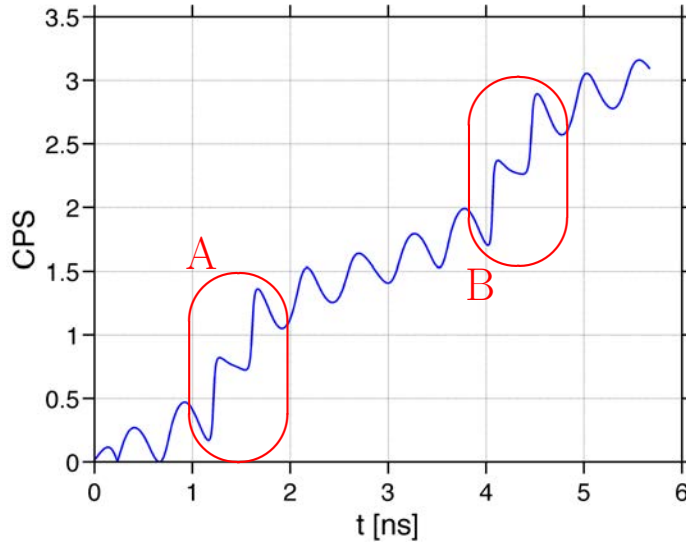
FIGURE A.3: CPS calculated in an effective two-level system derived from a Λ system by adiabatically eliminating the excited state. Only the unitary evolution of the effective hamiltonian was considered, that is all decay rates were ignored. The detunings used were: $(\delta_1, \delta_3) \approx (-7.48, -7.14)\, g_{P,T}$. The encircled regions labeled A and B show the rappid large phase jumps.

References

[1] E. Knill, R. Laflamme, and G. J. Milburn. *A scheme for efficient quantum computation with linear optics.* Nature **409**, 46 (2001). URL http://dx.doi.org/10.1038/35051009. xix, 2, 37, 38, 40, 42, 46

[2] J. Wenger, M. Hafezi, F. Grosshans, R. Tualle-Brouri, and P. Grangier. *Maximal violation of Bell inequalities using continuous-variable measurements.* Phys. Rev. A **67**(1), 012105 (2003). URL http://dx.doi.org/10.1103/PhysRevA.67.012105. 2, 71

[3] H. Nha and H. J. Carmichael. *Proposed Test of Quantum Nonlocality for Continuous Variables.* Physical Review Letters **93**(2), 020401 (2004). URL http://dx.doi.org/10.1103/PhysRevLett.93.020401.

[4] M. Stobińska, H. Jeong, and T. C. Ralph. *Violation of Bell's inequality using classical measurements and nonlinear local operations.* Phys. Rev. A **75**(5), 052105 (2007). URL http://dx.doi.org/10.1103/PhysRevA.75.052105. 2, 71

[5] S. E. Harris. *Electromagnetically induced transparency.* Physics Today **50**, 36 (1997). 3

[6] L. V. Hau, S. E. Harris, Z. Dutton, and C. H. Behroozi. *Light speed reduction to 17 metres per second in an ultracold atomic gas.* Nature **397**, 594 (1999). URL http://dx.doi.org/10.1038/17561. 14, 45

[7] D. F. Phillips, A. Fleischhauer, A. Mair, R. L. Walsworth, and M. D. Lukin. *Storage of light in atomic vapor.* Phys. Rev. Lett. **86**(5), 783 (2001). URL http://dx.doi.org/10.1103/PhysRevLett.86.783.

[8] M. Fleischhauer and M. D. Lukin. *Quantum memory for photons: Dark-state polaritons.* Phys. Rev. A **65**(2), 022314 (2002). URL http://dx.doi.org/10.1103/PhysRevA.65.022314. 12, 13, 14

[9] M. D. Lukin. *Colloquium: Trapping and manipulating photon states in atomic ensembles.* Rev. Mod. Phys. **75**(2), 457 (2003). URL http://dx.doi.org/10.1103/RevModPhys.75.457. 3, 11, 12

[10] J.-H. Wu, G. C. La Rocca, and M. Artoni. *Controlled light-pulse propagation in driven color centers in diamond.* Phys. Rev. B **77**(11), 113106 (2008). URL http://dx.doi.org/10.1103/PhysRevB.77.113106. 4, 19

[11] A. V. Turukhin, V. S. Sudarshanam, M. S. Shahriar, J. A. Musser, B. S. Ham, and P. R. Hemmer. *Observation of ultraslow and stored light pulses in a solid.* Phys. Rev. Lett. **88**(2), 023602 (2001). URL http://dx.doi.org/10.1103/PhysRevLett.88.023602. 4

[12] J. J. Longdell, E. Fraval, M. J. Sellars, and N. B. Manson. *Stopped light with storage times greater than one second using electromagnetically induced transparency in a solid.* Phys. Rev. Lett. **95**(6), 063601 (2005). URL http://dx.doi.org/10.1103/PhysRevLett.95.063601. 4, 14, 15

[13] C. Wei and N. B. Manson. *Observation of electromagnetically induced transparency within an electron spin resonance transition .* Journal of Optics B: Quantum and Semiclassical Optics **1**, 464 (1999). 4, 15

[14] P. R. Hemmer, A. V. Turukhin, M. S. Shahriar, and J. A. Musser. *Raman-excited spin coherences in nitrogen-vacancy color centers in diamond.* Opt. Lett. **26**, 361 (2001). URL http://dx.doi.org/10.1364/OL.26.000361. 4, 15

[15] R. M. Macfarlane. *High-resolution laser spectroscopy of rare-earth doped insulators: a personal perspective.* Jounal of Luminescence **100**(1-4), 1 (2002). 4

[16] A. A. Rangelov, N. V. Vitanov, L. P. Yatsenko, B. W. Shore, T. Halfmann, and K. Bergmann. *Stark-shift-chirped rapid-adiabatic-passage technique among three states.* Phys. Rev. A **72**(5), 053403 (2005). URL http://dx.doi.org/10.1103/PhysRevA.72.053403. xiv, 4, 21, 22, 23, 24, 25, 26, 27, 28, 32

[17] N. Vitanov, M. Fleischhauer, B. Shore, and K. Bergmann. *Coherent manipulation of atoms and molecules by sequential laser pulses.* vol. 46 of *Advances In Atomic, Molecular, and Optical Physics*, pp. 55 – 190 (Academic Press, 2001). URL http://dx.doi.org/10.1016/S1049-250X(01)80063-X. 9

[18] K. Bergmann, H. Theuer, and B. W. Shore. *Coherent population transfer among quantum states of atoms and molecules.* Rev. Mod. Phys. **70**(3), 1003 (1998). URL http://dx.doi.org/10.1103/RevModPhys.70.1003. xiii, 9

[19] M. Fleischhauer, A. Imamoglu, and J. P. Marangos. *Electromagnetically induced transparency: Optics in coherent media.* Reviews of Modern Physics **77**(2), 633 (2005). URL http://dx.doi.org/10.1103/RevModPhys.77.633. 10, 12

[20] S. E. Harris, J. E. Field, and A. Kasapi. *Dispersive properties of electromagnetically induced transparency.* Phys. Rev. A **46**(1), R29 (1992). URL http://dx.doi.org/10.1103/PhysRevA.46.R29. 12

[21] I. E. Mazets and B. G. Matisov. *Adiabatic Raman polariton in a Bose condensate.* Soviet Journal of Experimental and Theoretical Physics Letters **64**, 515 (1996). URL http://dx.doi.org/10.1134/1.567227. 13

[22] M. Fleischhauer and M. D. Lukin. *Dark-state polaritons in electromagnetically induced transparency.* Phys. Rev. Lett. **84**(22), 5094 (2000). URL http://dx.doi.org/10.1103/PhysRevLett.84.5094. xiii, 13, 14

[23] D. Budker, D. F. Kimball, S. M. Rochester, and V. V. Yashchuk. *Nonlinear magneto-optics and reduced group velocity of light in atomic vapor with slow ground state relaxation.* Phys. Rev. Lett. **83**(9), 1767 (1999). URL http://dx.doi.org/10.1103/PhysRevLett.83.1767. 14

[24] E. Parra and J. R. Lowell. *Toward applications of slow light technology.* Optics & Photonics News **18**(11), 40 (2007). 14

[25] M. Johnsson and K. Mølmer. *Storing quantum information in a solid using dark-state polaritons.* Phys. Rev. A **70**(3), 032320 (2004). URL http://dx.doi.org/10.1103/PhysRevA.70.032320. 15, 19

[26] J. Wrachtrup and F. Jelezko. *Processing quantum information in diamond.* Journal of Physics: Condensed Matter **18**(21), S807 (2006). 15, 18

[27] C. Santori, D. Fattal, S. M. Spillane, M. Fiorentino, R. G. Beausoleil, A. D. Greentree, P. Olivero, M. Draganski, J. R. Rabeau, P. Reichart, B. C. Gibson, S. Rubanov, D. N. Jamieson, and S. Prawer. *Coherent population trapping in diamond N-V centers at zero magnetic field.* Optics Express **14**, 7986 (2006). URL http://dx.doi.org/10.1364/OE.14.007986. 15

[28] C. Santori, P. Tamarat, P. Neumann, J. Wrachtrup, D. Fattal, R. G. Beausoleil, J. Rabeau, P. Olivero, A. D. Greentree, S. Prawer, F. Jelezko, and P. Hemmer. *Coherent Population Trapping of Single Spins in Diamond under Optical Excitation.* Physical Review Letters **97**(24), 247401 (2006). URL http://dx.doi.org/10.1103/PhysRevLett.97.247401. 15, 62

[29] F. Jelezko and J. Wrachtrup. *Single defect centres in diamond: A review.* physica status solidi (a) **203**(13), 3207 (2006). URL http://dx.doi.org/10.1002/pssa.200671403. xiii, 17, 18

[30] T. A. Kennedy, J. S. Colton, J. E. Butler, R. C. Linares, and P. J. Doering. *Long coherence times at 300 K for nitrogen-vacancy center spins in diamond grown by chemical vapor deposition.* Applied Physics Letters **83**, 4190 (2003). 15

[31] G. Balasubramanian, P. Neumann, D. Twitchen, M. Markham, R. Kolesov, N. Mizuochi, J. Isoya, J. Achard, J. Beck, J. Tissler, V. Jacques, P. R. Hemmer, F. Jelezko, and J. Wrachtrup. *Ultralong spin coherence time in isotopically engineered diamond.* Nature Materials **8**, 383 (2009). URL http://dx.doi.org/10.1038/nmat2420. 16, 23

[32] A. Lenef, S. W. Brown, D. A. Redman, S. C. Rand, J. Shigley, and E. Fritsch. *Electronic structure of the N-V center in diamond: Experiments.* Phys. Rev. B **53**, 13427 (1996). URL http://dx.doi.org/10.1103/PhysRevB.53.13427. 16

[33] V. M. Acosta, A. Jarmola, E. Bauch, and D. Budker. *Optical properties of the nitrogen-vacancy singlet levels in diamond.* Phys. Rev. B **82**(20), 201202 (2010). URL http://dx.doi.org/10.1103/PhysRevB.82.201202. xiii, 17, 18

[34] E. van Oort, N. B. Manson, and M. Glasbeek. *Optically detected spin coherence of the diamond N-V centre in its triplet ground state.* Journal of Physics C Solid State Physics **21**, 4385 (1988). URL http://dx.doi.org/10.1088/0022-3719/21/23/020. 17

[35] L. J. Rogers, S. Armstrong, M. J. Sellars, and N. B. Manson. *Infrared emission of the NV centre in diamond: Zeeman and uniaxial stress studies.* New Journal of Physics **10**(10), 103024 (2008). URL http://dx.doi.org/10.1088/1367-2630/10/10/103024. 17

[36] P. Delaney, J. C. Greer, and J. A. Larsson. *Spin-Polarization Mechanisms of the Nitrogen-Vacancy Center in Diamond.* Nano Letters **10**, 610 (2010). URL http://dx.doi.org/10.1021/nl903646p. 17

[37] M. W. Doherty, N. B. Manson, P. Delaney, and L. C. L. Hollenberg. *The negatively charged nitrogen-vacancy centre in diamond: the electronic solution.* ArXiv e-prints (2010). 1008.5224. 17

[38] A. Batalov, C. Zierl, T. Gaebel, P. Neumann, I.-Y. Chan, G. Balasubramanian, P. R. Hemmer, F. Jelezko, and J. Wrachtrup. *Temporal coherence of photons emitted by single nitrogen-vacancy defect centers in diamond using optical rabi-oscillations.* Phys. Rev. Lett. **100**(7), 077401 (2008). URL http://dx.doi.org/10.1103/PhysRevLett.100.077401. 17

[39] P. Neumann, R. Kolesov, V. Jacques, J. Beck, J. Tisler, A. Batalov, L. Rogers, N. B. Manson, G. Balasubramanian, F. Jelezko, and J. Wrachtrup. *Excited-state spectroscopy of single NV defects in diamond using optically detected magnetic resonance.* New Journal of Physics **11**(1), 013017 (2009). URL http://dx.doi.org/10.1088/1367-2630/11/1/013017. 17

[40] F. Jelezko, I. Popa, A. Gruber, C. Tietz, J. Wrachtrup, A. Nizovtsev, and S. Kilin. *Single spin states in a defect center resolved by optical spectroscopy.* Applied Physics Letters **81**, 2160 (2002). URL http://dx.doi.org/10.1063/1.1507838. 18

[41] C. Kurtsiefer, S. Mayer, P. Zarda, and H. Weinfurter. *Stable solid-state source of single photons.* Phys. Rev. Lett. **85**(2), 290 (2000). URL http://dx.doi.org/10.1103/PhysRevLett.85.290. 18

[42] R. Brouri, A. Beveratos, J. Poizat, and P. Grangier. *Photon antibunching in the fluorescence of individual color centers in diamond.* Optics Letters **25**, 1294 (2000). URL http://dx.doi.org/10.1364/OL.25.001294. 18

[43] A. Beveratos, R. Brouri, T. Gacoin, A. Villing, J.-P. Poizat, and P. Grangier. *Single photon quantum cryptography.* Phys. Rev. Lett. **89**(18), 187901 (2002). URL http://dx.doi.org/10.1103/PhysRevLett.89.187901. 18

[44] L. Childress, M. V. G. Dutt, J. M. Taylor, A. S. Zibrov, F. Jelezko, J. Wrachtrup, P. R. Hemmer, and M. D. Lukin. *Coherent Dynamics of Coupled Electron and Nuclear Spin Qubits in Diamond.* Science **314**, 281 (2006). URL http://dx.doi.org/10.1126/science.1131871. 18

[45] P.-H. Chung, E. Perevedentseva, J.-S. Tu, C. Chang, and C.-L. Cheng. *Spectroscopic study of bio-functionalized nanodiamonds.* Diamond and Related Materials **15**(4-8), 622 (2006). URL http://dx.doi.org/10.1016/j.diamond.2005.11.019. 18

[46] J. Tisler, G. Balasubramanian, B. Naydenov, R. Kolesov, B. Grotz, R. Reuter, J.-P. Boudou, P. A. Curmi, M. Sennour, A. Thorel, M. Börsch, K. Aulenbacher, R. Erdmann, P. R. Hemmer, F. Jelezko, and J. Wrachtrup. *Fluorescence and spin properties of defects in single digit nanodiamonds.* ACS Nano **3**(7), 1959 (2009). http://pubs.acs.org/doi/pdf/10.1021/nn9003617, URL http://dx.doi.org/10.1021/nn9003617. 18

[47] C. Bradac, T. Gaebel, N. Naidoo, M. J. Sellars, J. Twamley, L. J. Brown, A. S. Barnard, T. Plakhotnik, A. V. Zvyagin, and J. R. Rabeau. *Observation and control of blinking nitrogen-vacancy centres in discrete nanodiamonds.* Nature Nanotechnology **5**, 345 (2010). URL http://dx.doi.org/10.1038/nnano.2010.56. 18

[48] P. Tamarat, T. Gaebel, J. R. Rabeau, M. Khan, A. D. Greentree, H. Wilson, L. C. L. Hollenberg, S. Prawer, P. Hemmer, F. Jelezko, and J. Wrachtrup. *Stark shift control of single optical centers in diamond.* Phys. Rev. Lett. **97**(8), 083002 (2006). URL http://dx.doi.org/10.1103/PhysRevLett.97.083002. 18

[49] Y. Shen, T. M. Sweeney, and H. Wang. *Zero-phonon linewidth of single nitrogen vacancy centers in diamond nanocrystals.* Phys. Rev. B **77**(3), 033201 (2008). URL http://dx.doi.org/10.1103/PhysRevB.77.033201. 18

[50] N. Khaneja, T. Reiss, C. Kehlet, T. Schulte-Herbrüggen, and S. J. Glaser. *Optimal control of coupled spin dynamics: design of NMR pulse sequences by gradient ascent algorithms.* J. Magn. Reson. **172**, 296 (2005). URL http://dx.doi.org/10.1016/j.jmr.2004.11.004. 21, 30, 36

[51] L. P. Yatsenko, B. W. Shore, T. Halfmann, K. Bergmann, and A. Vardi. *Source of metastable h(2s) atoms using the stark chirped rapid-adiabatic-passage technique.* Phys. Rev. A **60**(6), R4237 (1999). URL http://dx.doi.org/10.1103/PhysRevA.60.R4237. 22

[52] T. Rickes, L. P. Yatsenko, S. Steuerwald, T. Halfmann, B. W. Shore, N. V. Vitanov, and K. Bergmann. *Efficient adiabatic population transfer by two-photon*

excitation assisted by a laser-induced Stark shift. J. Chem. Phys. **113**, 534 (2000). URL http://dx.doi.org/10.1063/1.481829. 22

[53] M. P. Fewell, B. W. Shore, and K. Bergmann. *Coherent population transfer among three states: Full algebraic solutions and the relevance of non adiabatic processes to transfer by delayed pulses.* Australian Journal of Physics **50**, 281 (1997). URL http://dx.doi.org/doi:10.1071/P96071. 23

[54] B. Y. Chang, H. Choi, S. Shin, and I. R. Sola. *Quantum-state-selective two-photon excitation of multilevel systems assisted by the stark shift.* Phys. Rev. A **75**(6), 063405 (2007). URL http://dx.doi.org/10.1103/PhysRevA.75.063405. 29

[55] S. Lloyd. *Almost any quantum logic gate is universal.* Phys. Rev. Lett. **75**(2), 346 (1995). URL http://dx.doi.org/10.1103/PhysRevLett.75.346. 37

[56] D. P. DiVincenzo. *Two-bit gates are universal for quantum computation.* Phys. Rev. A **51**(2), 1015 (1995). URL http://dx.doi.org/10.1103/PhysRevA.51.1015. 37

[57] C. K. Hong, Z. Y. Ou, and L. Mandel. *Measurement of subpicosecond time intervals between two photons by interference.* Phys. Rev. Lett. **59**(18), 2044 (1987). URL http://dx.doi.org/10.1103/PhysRevLett.59.2044. 40

[58] P. Kok, W. J. Munro, K. Nemoto, T. C. Ralph, J. P. Dowling, and G. J. Milburn. *Linear optical quantum computing with photonic qubits.* Rev. Mod. Phys. **79**(1), 135 (2007). URL http://dx.doi.org/10.1103/RevModPhys.79.135. 40

[59] S. Scheel, W. J. Munro, J. Eisert, K. Nemoto, and P. Kok. *Feed-forward and its role in conditional linear optical quantum dynamics.* Phys. Rev. A **73**(3), 034301 (2006). URL http://dx.doi.org/10.1103/PhysRevA.73.034301. 40

[60] K. Sanaka, T. Jennewein, J.-W. Pan, K. Resch, and A. Zeilinger. *Experimental nonlinear sign shift for linear optics quantum computation.* Phys. Rev. Lett. **92**(1), 017902 (2004). URL http://dx.doi.org/10.1103/PhysRevLett.92.017902. 41

[61] E. Knill. *Quantum gates using linear optics and postselection.* Phys. Rev. A **66**(5), 052306 (2002). URL http://dx.doi.org/10.1103/PhysRevA.66.052306. xv, 42

[62] E. Knill. *Bounds on the probability of success of postselected nonlinear sign shifts implemented with linear optics.* Phys. Rev. A **68**(6), 064303 (2003). URL http://dx.doi.org/10.1103/PhysRevA.68.064303. 43

[63] T. B. Pittman, M. J. Fitch, B. C. Jacobs, and J. D. Franson. *Experimental controlled-not logic gate for single photons in the coincidence basis.* Phys. Rev. A **68**(3), 032316 (2003). URL http://dx.doi.org/10.1103/PhysRevA.68.032316. 43, 47

[64] T. C. Ralph, N. K. Langford, T. B. Bell, and A. G. White. *Linear optical controlled-NOT gate in the coincidence basis.* Phys. Rev. A **65**(6), 062324 (2002). URL http://dx.doi.org/10.1103/PhysRevA.65.062324. 43

[65] J. L. O'Brien, G. J. Pryde, A. G. White, T. C. Ralph, and D. Branning. *Demonstration of an all-optical quantum controlled-NOT gate.* Nature **426**, 264 (2003). URL http://dx.doi.org/10.1038/nature02054. 43

[66] T. B. Pittman, B. C. Jacobs, and J. D. Franson. *Probabilistic quantum logic operations using polarizing beam splitters.* Phys. Rev. A **64**(6), 062311 (2001). URL http://dx.doi.org/10.1103/PhysRevA.64.062311. 43

[67] Z. Zhao, A.-N. Zhang, Y.-A. Chen, H. Zhang, J.-F. Du, T. Yang, and J.-W. Pan. *Experimental demonstration of a nondestructive controlled-not quantum gate for two independent photon qubits.* Phys. Rev. Lett. **94**(3), 030501 (2005). URL http://dx.doi.org/10.1103/PhysRevLett.94.030501. 43

[68] G. J. Milburn. *Quantum optical Fredkin gate.* Physical Review Letters **62**, 2124 (1989). URL http://dx.doi.org/10.1103/PhysRevLett.62.2124. 43

[69] Q. A. Turchette, C. J. Hood, W. Lange, H. Mabuchi, and H. J. Kimble. *Measurement of conditional phase shifts for quantum logic.* Physical Review Letters **75**, 4710 (1995). arXiv:quant-ph/9511008, URL http://dx.doi.org/10.1103/PhysRevLett.75.4710. 45, 46, 51

[70] M. A. Nielsen and I. L. Chaung. *Quantum Computation and Quantum Information* (Cambridge University Press, Cambridge, 2000). 45

[71] N. Matsuda, R. Shimizu, Y. Mitsumori, H. Kosaka, and K. Edamatsu. *Observation of optical-fibre Kerr nonlinearity at the single-photon level.* Nature Photonics **3**, 95 (2009). URL http://dx.doi.org/10.1038/nphoton.2008.292. 45

[72] J. H. Shapiro. *Single-photon Kerr nonlinearities do not help quantum computation.* Phys. Rev. A **73**(6), 062305 (2006). URL http://dx.doi.org/10.1103/PhysRevA.73.062305. 45, 46

[73] M. D. Lukin and A. Imamoğlu. *Controlling photons using electromagnetically induced transparency.* Nature **413**, 273 (2001). URL http://dx.doi.org/10.1038/35095000. 45

[74] H. Schmidt and A. Imamogdlu. *Giant Kerr nonlinearities obtained by electromagnetically induced transparency.* Opt. Lett. **21**(23), 1936 (1996). URL http://ol.osa.org/abstract.cfm?URI=ol-21-23-1936. 45

[75] M. S. Zubairy, A. B. Matsko, and M. O. Scully. *Resonant enhancement of high-order optical nonlinearities based on atomic coherence.* Phys. Rev. A **65**(4), 043804 (2002). URL http://dx.doi.org/10.1103/PhysRevA.65.043804. 45

[76] A. B. Matsko, I. Novikova, M. S. Zubairy, and G. R. Welch. *Nonlinear magneto-optical rotation of elliptically polarized light*. Phys. Rev. A **67**(4), 043805 (2003). URL http://dx.doi.org/10.1103/PhysRevA.67.043805. 45

[77] A. D. Greentree, D. Richards, J. A. Vaccaro, A. V. Durrant, S. R. d. Echaniz, D. M. Segal, and J. P. Marangos. *Intensity-dependent dispersion under conditions of electromagnetically induced transparency in coherently prepared multistate atoms*. Phys. Rev. A **67**(2), 023818 (2003). URL http://dx.doi.org/10.1103/PhysRevA.67.023818. 45

[78] H. Wang, D. Goorskey, and M. Xiao. *Enhanced kerr nonlinearity via atomic coherence in a three-level atomic system*. Phys. Rev. Lett. **87**(7), 073601 (2001). URL http://dx.doi.org/10.1103/PhysRevLett.87.073601. 45, 46

[79] F. G. S. L. Brandão, M. J. Hartmann, and M. B. Plenio. *Light-shift-induced photonic nonlinearities*. New Journal of Physics **10**(4), 043010 (2008). URL http://dx.doi.org/10.1088/1367-2630/10/4/043010. 45

[80] R. García-Maraver, R. Corbalán, K. Eckert, S. Rebić, M. Artoni, and J. Mompart. *Cavity qed quantum phase gates for a single longitudinal mode of the intracavity field*. Phys. Rev. A **70**(6), 062324 (2004). URL http://dx.doi.org/10.1103/PhysRevA.70.062324. 45

[81] M. S. Zubairy, M. Kim, and M. O. Scully. *Cavity-QED-based quantum phase gate*. Phys. Rev. A **68**(3), 033820 (2003). URL http://dx.doi.org/10.1103/PhysRevA.68.033820. 45

[82] D. Petrosyan and Y. P. Malakyan. *Magneto-optical rotation and cross-phase modulation via coherently driven four-level atomsin a tripod configuration*. Phys. Rev. A **70**(2), 023822 (2004). URL http://dx.doi.org/10.1103/PhysRevA.70.023822. 45

[83] S. Rebić, D. Vitali, C. Ottaviani, P. Tombesi, M. Artoni, F. Cataliotti, and R. Corbalán. *Polarization phase gate with a tripod atomic system*. Phys. Rev. A **70**(3), 032317 (2004). URL http://dx.doi.org/10.1103/PhysRevA.70.032317. 51, 52, 53, 54, 56, 62

[84] X. Yang, S. Li, C. Zhang, and H. Wang. *Enhanced cross-kerr nonlinearity via electromagnetically induced transparency in a four-level tripod atomic system*. J. Opt. Soc. Am. B **26**(7), 1423 (2009). URL http://dx.doi.org/10.1364/JOSAB.26.001423. 45

[85] K. J. Jiang, L. Deng, E. W. Hagley, and M. G. Payne. *Fast-responding nonlinear phase shifter using a signal-wave gain medium*. Phys. Rev. A **77**(4), 045804 (2008). URL http://dx.doi.org/10.1103/PhysRevA.77.045804. 45

[86] A. Joshi and M. Xiao. *Phase gate with a four-level inverted-y system*. Phys. Rev. A **72**(6), 062319 (2005). URL http://dx.doi.org/10.1103/PhysRevA.72.062319. 45

[87] P. Li, Y. Gu, L. Wang, and Q. Gong. *Fifth-order nonlinearity and 3-qubit phase gate in a five-level tripod atomic system.* Journal of the Optical Society of America B Optical Physics **25**, 504 (2008). URL http://dx.doi.org/10.1364/JOSAB.25.000504. 45

[88] C. Ottaviani, D. Vitali, M. Artoni, F. Cataliotti, and P. Tombesi. *Polarization qubit phase gate in driven atomic media.* Phys. Rev. Lett. **90**(19), 197902 (2003). URL http://dx.doi.org/10.1103/PhysRevLett.90.197902. 45

[89] C. Ottaviani, S. Rebić, D. Vitali, and P. Tombesi. *Quantum phase-gate operation based on nonlinear optics: Full quantum analysis.* Phys. Rev. A **73**(1), 010301 (2006). URL http://dx.doi.org/10.1103/PhysRevA.73.010301. 63

[90] S. Rebić, C. Ottaviani, G. di Giuseppe, D. Vitali, and P. Tombesi. *Assessment of a quantum phase-gate operation based on nonlinear optics.* Phys. Rev. A **74**(3), 032301 (2006). URL http://dx.doi.org/10.1103/PhysRevA.74.032301. xvii, 45, 63, 83, 84

[91] H. Kang and Y. Zhu. *Observation of large kerr nonlinearity at low light intensities.* Phys. Rev. Lett. **91**(9), 093601 (2003). URL http://dx.doi.org/10.1103/PhysRevLett.91.093601. 46

[92] H. Chang, Y. Du, J. Yao, C. Xie, and H. Wang. *Observation of cross-phase shift in hot atoms with quantum coherence.* EPL (Europhysics Letters) **65**(4), 485 (2004). URL http://stacks.iop.org/0295-5075/65/i=4/a=485. 46

[93] S. Li, X. Yang, X. Cao, C. Zhang, C. Xie, and H. Wang. *Enhanced cross-phase modulation based on a double electromagnetically induced transparency in a four-level tripod atomic system.* Phys. Rev. Lett. **101**(7), 073602 (2008). URL http://dx.doi.org/10.1103/PhysRevLett.101.073602. 46, 52, 56

[94] Y. Han, J. Xiao, Y. Liu, C. Zhang, H. Wang, M. Xiao, and K. Peng. *Interacting dark states with enhanced nonlinearity in an ideal four-level tripod atomic system.* Phys. Rev. A **77**(2), 023824 (2008). URL http://dx.doi.org/10.1103/PhysRevA.77.023824. 46, 56

[95] Z.-B. Wang, K.-P. Marzlin, and B. C. Sanders. *Large cross-phase modulation between slow copropagating weak pulses in ^{87}Rb.* Phys. Rev. Lett. **97**(6), 063901 (2006). URL http://dx.doi.org/10.1103/PhysRevLett.97.063901. 46

[96] K. Nemoto and W. J. Munro. *Nearly deterministic linear optical controlled-not gate.* Phys. Rev. Lett. **93**(25), 250502 (2004). URL http://dx.doi.org/10.1103/PhysRevLett.93.250502. xv, xvi, 47, 48, 49

[97] G. J. Milburn and D. F. Walls. *State reduction in quantum-counting quantum nondemolition measurements.* Phys. Rev. A **30**(1), 56 (1984). URL http://dx.doi.org/10.1103/PhysRevA.30.56. 47

[98] N. Imoto, H. A. Haus, and Y. Yamamoto. *Quantum nondemolition measurement of the photon number via the optical kerr effect.* Phys. Rev. A **32**(4), 2287 (1985). URL http://dx.doi.org/10.1103/PhysRevA.32.2287.

[99] P. Grangier, J. A. Levenson, and J. Poizat. *Quantum non-demolition measurements in optics.* Nature **396**, 537 (1998). URL http://dx.doi.org/10.1038/25059. 47

[100] A. Einstein, B. Podolsky, and N. Rosen. *Can quantum-mechanical description of physical reality be considered complete?* Phys. Rev. **47**(10), 777 (1935). URL http://dx.doi.org/10.1103/PhysRev.47.777. 48

[101] J. D. Franson, B. C. Jacobs, and T. B. Pittman. *Quantum computing using single photons and the zeno effect.* Phys. Rev. A **70**(6), 062302 (2004). URL http://dx.doi.org/10.1103/PhysRevA.70.062302. 49

[102] P. M. Leung and T. C. Ralph. *Optical zeno gate: bounds for fault tolerant operation.* New Journal of Physics **9**, 224 (2007). URL http://dx.doi.org/10.1088/1367-2630/9/7/224. 49, 50

[103] D. Gottesman and I. L. Chuang. *Demonstrating the viability of universal quantum computation using teleportation and single-qubit operations.* Nature **402**, 390 (1999). URL http://dx.doi.org/10.1038/46503. 50

[104] H. J. Kimble. *Strong Interactions of Single Atoms and Photons in Cavity QED.* Physica Scripta Volume T **76**, 127 (1998). URL http://dx.doi.org/10.1238/Physica.Topical.076a00127. 51, 58

[105] D. K. Armani, T. J. Kippenberg, S. M. Spillane, and K. J. Vahala. *Ultra-high-Q toroid microcavity on a chip.* Nature **421**, 925 (2003). URL http://dx.doi.org/10.1038/nature01371. 52, 58, 59

[106] M. L. Gorodetsky, A. A. Savchenkov, and V. S. Ilchenko. *Ultimate Q of optical microsphere resonators.* Optics Letters **21**, 453 (1996). URL http://dx.doi.org/10.1364/OL.21.000453. 52, 58, 59

[107] Y. Park, A. K. Cook, and H. Wang. *Cavity QED with Diamond Nanocrystals and Silica Microspheres.* Nano Letters **6**, 2075 (2006). URL http://dx.doi.org/10.1021/nl061342r. 52, 59

[108] P. E. Barclay, C. Santori, K. Fu, R. G. Beausoleil, and O. Painter. *Coherent interference effects in a nano-assembled diamond NV center cavity-QED system.* Optics Express **17**, 8081 (2009). URL http://dx.doi.org/10.1364/OE.17.008081. 52, 58, 59, 62

[109] S. M. Tan. *A computational toolbox for quantum and atomic optics.* Journal of Optics B: Quantum and Semiclassical Optics **1**, 424 (1999). 52

[110] R. Unanyan, M. Fleischhauer, B. W. Shore, and K. Bergmann. *Robust creation and phase-sensitive probing of superposition states via stimulated Raman adiabatic passage (STIRAP) with degenerate dark states.* Optics Communications **155**, 144 (1998). URL http://dx.doi.org/10.1016/S0030-4018(98)00358-7. 52

[111] S. M. Spillane. *Fiber-coupled ultra-high-Q microresonators for nonlinear and quantum optics.* Ph.D. thesis, California Institute of Technology (2004). 57

[112] T. J. Kippenberg. *Nonlinear optics in ultra-high-Q whispering-gallery optical microcavities.* Ph.D. thesis, California Institute of Technology (2004). 57

[113] A. Mazzei. *Cavity enhanced optical processes in microsphere resonators.* Ph.D. thesis, Humboldt-Universität zu Berlin, Mathematisch-Naturwissenschaftliche Fakultät I (2008). 57, 58

[114] P. E. Barclay, K. Srinivasan, O. Painter, B. Lev, and H. Mabuchi. *Integration of fiber-coupled high-Q SiN_x microdisks with atom chips.* Applied Physics Letters **89**(13), 131108 (2006). URL http://dx.doi.org/10.1063/1.2356892. 58

[115] M. Soltani, S. Yegnanarayanan, and A. Adibi. *Ultra-high Q planar silicon microdisk resonators for chip-scale silicon photonics.* Optics Express **15**, 4694 (2007). URL http://dx.doi.org/10.1364/OE.15.004694. 58

[116] T. J. Kippenberg, S. M. Spillane, and K. J. Vahala. *Demonstration of ultra-high-Q small mode volume toroid microcavities on a chip.* Applied Physics Letters **85**, 6113 (2004). URL http://dx.doi.org/10.1063/1.1833556. 58

[117] P. E. Barclay, K. Fu, C. Santori, and R. G. Beausoleil. *Chip-based microcavities coupled to nitrogen-vacancy centers in single crystal diamond.* Applied Physics Letters **95**(19), 191115 (2009). URL http://dx.doi.org/10.1063/1.3262948. 58

[118] A. Beveratos, R. Brouri, T. Gacoin, J.-P. Poizat, and P. Grangier. *Nonclassical radiation from diamond nanocrystals.* Phys. Rev. A **64**(6), 061802 (2001). URL http://dx.doi.org/10.1103/PhysRevA.64.061802. 58

[119] B. R. Smith, D. W. Inglis, B. Sandnes, J. R. Rabeau, A. V. Zvyagin, D. Gruber, C. J. Noble, R. Vogel, E. Ōsawa, and T. Plakhotnik. *Five-nanometer diamond with luminescent nitrogen-vacancy defect centers.* Small **5**, 1649?1653 (2009). 58

[120] T. van der Sar, E. C. Heeres, G. M. Dmochowski, G. de Lange, L. Robledo, T. H. Oosterkamp, and R. Hanson. *Nanopositioning of a diamond nanocrystal containing a single nitrogen-vacancy defect center.* Applied Physics Letters **94**(17), 173104 (2009). URL http://dx.doi.org/10.1063/1.3120558. 59

[121] M. Larsson, K. N. Dinyari, and H. Wang. *Composite Optical Microcavity of Diamond Nanopillar and Silica Microsphere.* Nano Letters **9**, 1447 (2009). URL http://dx.doi.org/10.1021/nl8032944. 59

[122] S. Schietinger, T. Schröder, and O. Benson. *One-by-One Coupling of Single Defect Centers in Nanodiamonds to High-Q Modes of an Optical Microresonator.* Nano Letters **8**, 3911 (2008). URL http://dx.doi.org/10.1021/nl8023627. 59

[123] S. Schietinger and O. Benson. *Coupling single NV-centres to high-Q whispering gallery modes of a preselected frequency-matched microresonator.* Journal of Physics B Atomic Molecular Physics **42**(11), 114001 (2009). URL http://dx.doi.org/10.1088/0953-4075/42/11/114001. 59

[124] S. Rebić, D. Vitali, C. Ottaviani, P. Tombesi, M. Artoni, F. Cataliotti, and R. Corbalan. *Quantum theory of a polarization phase gate in an atomic tripod configuration.* Optics and Spectroscopy **99**, 264 (2005). URL http://dx.doi.org/10.1134/1.2034613. 62

[125] I. Rotter and A. F. Sadreev. *Zeros in single-channel transmission through double quantum dots.* Phys. Rev. E **71**(4), 046204 (2005). URL http://dx.doi.org/10.1103/PhysRevE.71.046204. 64

[126] M. Sigrist, T. Ihn, K. Ensslin, M. Reinwald, and W. Wegscheider. *Coherent probing of excited quantum dot states in an interferometer.* Phys. Rev. Lett. **98**(3), 036805 (2007). URL http://dx.doi.org/10.1103/PhysRevLett.98.036805. 64

[127] G. Benenti and G. Strini. *Simple representation of quantum process tomography.* Phys. Rev. A **80**(2), 022318 (2009). URL http://dx.doi.org/10.1103/PhysRevA.80.022318. 65

[128] S. Watanabe, R. Matsumoto, and T. Uyematsu. *Tomography increases key rates of quantum-key-distribution protocols.* Phys. Rev. A **78**(4), 042316 (2008). 69

[129] E. Schrödinger. *Die gegenwärtige Situation in der Quantenmechanik.* Naturwissenschaften **23**, 807 (1935). URL http://dx.doi.org/10.1007/BF01491891. 71

[130] H. Jeong, M. S. Kim, and J. Lee. *Quantum-information processing for a coherent superposition state via a mixedentangled coherent channel.* Phys. Rev. A **64**(5), 052308 (2001). URL http://dx.doi.org/10.1103/PhysRevA.64.052308. 71

[131] S. J. van Enk and O. Hirota. *Entangled coherent states: Teleportation and decoherence.* Phys. Rev. A **64**(2), 022313 (2001). URL http://dx.doi.org/10.1103/PhysRevA.64.022313.

[132] T. C. Ralph, A. Gilchrist, G. J. Milburn, W. J. Munro, and S. Glancy. *Quantum computation with optical coherent states.* Phys. Rev. A **68**(4), 042319 (2003). URL http://dx.doi.org/10.1103/PhysRevA.68.042319.

[133] A. Gilchrist, K. Nemoto, W. J. Munro, T. C. Ralph, S. Glancy, S. L. Braunstein, and G. J. Milburn. *Schrödinger cats and their power for quantum information*

processing. Journal of Optics B: Quantum and Semiclassical Optics **6**, 828 (2004). URL http://dx.doi.org/10.1088/1464-4266/6/8/032. 71

[134] B. Yurke and D. Stoler. *Generating quantum mechanical superpositions of macroscopically distinguishable states via amplitude dispersion.* Physical Review Letters **57**, 13 (1986). URL http://dx.doi.org/10.1103/PhysRevLett.57.13. 71

[135] M. Brune, S. Haroche, J. M. Raimond, L. Davidovich, and N. Zagury. *Manipulation of photons in a cavity by dispersive atom-field coupling: Quantum-nondemolition measurements and generation of "Schrödinger cat" states.* Phys. Rev. A. **45**, 5193 (1992). URL http://dx.doi.org/10.1103/PhysRevA.45.5193. 71

[136] D. Vitali, P. Tombesi, and P. Grangier. *Conditional Schrödinger cats generation and detection by quantum non-demolition measurements.* Applied Physics B: Lasers and Optics **64**, 249 (1996). URL http://dx.doi.org/10.1007/s003400050171. 71, 73

[137] A. Kenfack and K. Zyczkowski. *Negativity of the Wigner function as an indicator of non-classicality.* Journal of Optics B: Quantum and Semiclassical Optics **6**, 396 (2004). arXiv:quant-ph/0406015, URL http://dx.doi.org/10.1088/1464-4266/6/10/003. 73

[138] C.-W. Lee and H. Jeong. *Quantification of macroscopic quantum superpositions within phase space.* Phys. Rev. Lett. **106**(22), 220401 (2011). 75

[139] E. Brion, L. H. Pedersen, and K. Mølmer. *Adiabatic elimination in a lambda system.* Journal of Physics A Mathematical General **40**, 1033 (2007). URL http://dx.doi.org/10.1088/1751-8113/40/5/011. 84